



2020

Development of Lipid-based Nano Formulations of Miriplatin Against Lung Cancer

Zizhao Xu

University of the Pacific, z_xu8@u.pacific.edu

Follow this and additional works at: https://scholarlycommons.pacific.edu/uop_etds

 Part of the [Pharmacy and Pharmaceutical Sciences Commons](#)

Recommended Citation

Xu, Zizhao. (2020). *Development of Lipid-based Nano Formulations of Miriplatin Against Lung Cancer*. University of the Pacific, Thesis. https://scholarlycommons.pacific.edu/uop_etds/3699

This Thesis is brought to you for free and open access by the Graduate School at Scholarly Commons. It has been accepted for inclusion in University of the Pacific Theses and Dissertations by an authorized administrator of Scholarly Commons. For more information, please contact mgibney@pacific.edu.

DEVELOPMENT OF LIPID-BASED NANO FORMULATIONS OF MIRIPLATIN
AGAINST LUNG CANCER

By

Zizhao Xu

A Thesis Submitted to the
Graduate School
In Partial Fulfillment of the
Requirements for the Degree of
MASTER OF SCIENCE

Thomas J. Long School of Pharmacy and Health Sciences
Pharmaceutical and Chemical Sciences

University of the Pacific
Stockton, California

2020

DEVELOPMENT OF LIPID-BASED NANO FORMULATIONS OF MIRIPLATIN
AGAINST LUNG CANCER

By

Zizhao Xu

APPROVED BY:

Thesis Advisor: Xin Guo, Ph.D.

Committee Member: Xiaoling Li, Ph.D.

Committee Member: Qinliang Zhao, Ph.D.

Department Chair: William K. Chan, Pharm.D., Ph.D.

ACKNOWLEDGEMENTS

I would like to express my sincere gratitude to many people because it would be impossible for me to present my research here without their help.

I want to thank my advisor Dr. Xin Guo first for his continuous guidance and support in the past two years. His enthusiasm and critical thinking in academia have shaped me into an independent and comprehensive researcher. He enlightened me with such insightful guidance and encouragement that helped me navigate through all the hurdles during my experiment. It has been such an honor and pleasure for me to work with him.

I would also like to thank my thesis committee members Dr. Xiaoling Li and Dr. Qinliang Zhao for their invaluable contribution to my thesis. I want to express my gratitude particularly to Dr. Li for introducing this outstanding PCSP program to me because he did change my scientific road when we first met two years ago. He also gave me brilliant suggestions to my research and academic career. I would like to thank Dr. Zhao for the permission to work in her lab as well as all her suggestions to my project. She is an expert in inorganic chemistry, especially in the field of platinum and I learnt a lot from her. I would also like to thank Dr. William K. Chan, Dr. John C. Livesey and Dr. Jianhua Ren for the resource in their labs that supported my research. I want to thank Dr. Fei Guo for using TEM in his department at UC Davis. My thanks also go to Lynda, Sonya, Kathy and all PCSP faculty and staff for their kindness and generous help during my study life here.

I would like to thank the Guo group members both past and present for providing me this friendly and collaborating research environment. It was such a pleasure for me to work with

them. I would like to especially thank Dr. Yifan Lu and Yingbo Huang, who have given me great training and assistance on my project. I want to thank Zhongyue Yuan for being my partner and all the discussion on with her. I also want to thank Dr. Mallika Vadlamudi, Dr. Shen Zhao, Ruiqi Huang, Xinyu Pei and Yong Zhu for their support and kindness both in my project and in my life. Special thanks to Dr. Chao Feng and Yuntao Zhang for teaching me using their instruments and giving me their great advice. I want to thank my friends Jingda Wang, Hao Wei, Dengpan Liang, Rui Xiong, Michael Ng, Arjun Patel, Yiyuan Wang, Yujie Yang, Jinyu Chen, Fang Liu, Md Tariqul Haque Tuhin, Toufiq Ul Amin, Guanming Jiang, Ryan Murray and Shengxi Li, for all the help and making my life in Pacific memorable. I want to thank Qing Zhang especially, who has given me countless support and love in my daily life.

Finally, I would like to thank my family. Their unconditional love and support strengthen me to walk through this tough but invaluable journey.

DEVELOPMENT OF LIPID-BASED NANO FORMULATIONS OF MIRIPLATIN AGAINST LUNG CANCER

Abstract

By Zizhao Xu

University of the Pacific
2020

Cancer is the second leading cause of death and is responsible for approximately 9.6 million deaths worldwide in 2018. Among all oncological diseases, lung cancer claims the highest mortality (male: 23.5%; female: 22%) and the second most new cases (male: 13%; female: 12%) in the US. Approximately 40% of newly diagnosed lung cancer patients are in the advanced stage IV, for which platinum-based chemotherapy is the first-line treatment, either by itself or in combination with surgery or radiotherapy.

Cisplatin, the first-generation platinum-based anticancer chemotherapeutic agent, has the highest potency against lung cancer but carries many severe adverse effects. Cisplatin also induces drug resistance during long-term chemotherapy. Many more platinum complexes have been investigated as better alternatives, which led to the approval of carboplatin and oxaliplatin by Food and Drug Administration (FDA). In addition, miriplatin suspended in iodolipids (lipiodolization) was approved in Japan for the treatment of hepatocellular carcinoma (HCC) in 2009. Miriplatin has the same non-leaving group as oxaliplatin but different leaving groups of two myristate chains, which make it highly lipophilic.

Several characteristics of solid tumors in lung cancer constitute a physiochemical barrier to the homogenous distribution and deep penetration of chemotherapy agents. Nanocarriers

provide a promising platform to overcome the physiochemical barrier and to reduce the systemic toxicity of anticancer chemotherapy. In this study, miriplatin is formulated with various lipid-based nanocarriers including micelles and solid lipid nanoparticles (SLNs) thanks to its highly lipophilic structure. The goal of this thesis is to develop and evaluate miriplatin-loaded nano formulations against lung cancer.

Miriplatin-loaded formulations were prepared by different methods, including thin film hydration and several scale-up methods including chloroform dripping, chloroform injection, chloroform evaporation, co-solvent evaporation, chloroform slow evaporation and co-solvent slow evaporation. Between the two types of nano formulations under this study, micelles were much smaller (~10 nm in diameter) and more homogeneous (PDI < 0.3), while SLNs were bigger (~ 100 nm in diameter) and more heterogeneous (PDI ~0.8). A quantification method of miriplatin was established using inductively coupled plasma-optical emission spectrometry (ICP-OES). The quantification of platinum recovery from different miriplatin-loaded nano formulations was facilitated by digestion with 70% nitric acid and heating. The co-solvent slow evaporation method to prepare miriplatin-loaded nano formulations improved the platinum recovery prominently from 10% to 70%. Thus, co-solvent slow evaporation has been established as a pharmaceutically viable scale-up method to prepare nano formulations of miriplatin.

Miriplatin-loaded nano formulations of different compositions were negatively stained with uranyl acetate and then imaged by transmission electron microscopy (TEM), which showed the formulations' size and morphology that were consistent with the size and PDI data from dynamic light scattering studies by the Malvern Zetasizer. In the TEM studies, micelles showed a morphology of spherical dots at around 10 nm in diameter while SLNs showed both spherical and rod structures with a size distribution from 50 to 150 nm.

A three-dimensional multicellular spheroid (3D MCS) model of A549-iRFP cells was used for *in vitro* evaluation of the nano formulations' activity against lung cancer. A549-iRFP cells were engineered from the common lung cancer cell line A549 to stably express the near-infrared fluorescent protein (iRFP). The viability of A549-iRFP 3D MCS after exposure to cisplatin or nano formulations was similar to A549 3D MCS. The anticancer activity of miriplatin-loaded nano formulations against 3D MCS was positively associated with the platinum recovery as quantified by ICP-OES. The miriplatin-loaded nano formulations that had been prepared by the co-solvent slow evaporation method showed substantial anticancer activities against A549 3D MCS and A549-iRFP 3D MCS, which were comparable to cisplatin.

Taken together, miriplatin-loaded nano formulations were successfully prepared by co-solvent slow evaporation. The formulations were developed to carry favorable physiochemical properties to enhance the activities of platinum drugs against lung cancer.

TABLE OF CONTENTS

List of Tables	12
List of Figures	13
List of Abbreviations	16
Chapter 1: Introduction	19
1.1 Statement of the Problem.....	19
1.1.1 Lung Cancer.....	19
1.1.2 Treatment Options And Chemotherapy	20
1.1.3 Platinum-Based Anticancer Drugs.....	22
1.1.4 Barriers of Drug Delivery into Solid Tumor.....	26
1.2 Strategies for Effective Drug Delivery to Solid Tumors	28
1.2.1 Passive Targeting	29
1.2.2 Active Targeting	31
1.2.3 Lipid-Based Nanocarriers	31
1.3 Miriplatin-Loaded Nano Formulations and their Proposed Mechanism of Action	34
1.4 Hypothesis and Specific Aims	36
Chapter 2: Preparation of Miriplatin-Loaded Nano Formulations	37
2.1 Introduction.....	37
2.1.1 Strategies to Prepare Nano Formulations	37
2.1.2 Components of Miriplatin-Loaded Formulations	39

2.2 Materials and Methods.....	41
2.2.1 Materials	41
2.2.2 Preparation Methods for Miriplatin-Loaded Formulations.....	42
2.2.3 Physicochemical Characterizations of Miriplatin-Loaded Nano Formulations	46
2.3 Results and Discussion	47
2.3.1 Size Distribution of Miriplatin-Loaded Formulations Based on Intensity, Volume and Number Weighing from the Malvern Zetasizer Software	47
2.3.2 Effect of the Payload Drug Miriplatin to the Nano Formulations	51
2.3.3 Effect of Lipid Components.....	52
2.3.4 Comparison of Different Methods to Prepare Nano Formulations.....	54
2.3.5 Size and Polydispersity Index (PDI) of Miriplatin-Loaded Formulations Prepared by Co-Solvent Slow Evaporation	58
2.4 Summary	60
Chapter 3: Physicochemical Characterization of Miriplatin-Loaded Nano Formulations	61
3.1 Introduction.....	61
3.1.1 Solubility of Miriplatin	61
3.1.2 Quantification of Miriplatin.....	61
3.1.3 Transmission Electron Microscopy (TEM)	63
3.2 Materials and Methods.....	64
3.2.1 Materials	64
3.2.2 Quantification of Miriplatin by HPLC.....	64
3.2.3 Mass Spectrometer.....	64
3.2.4 Quantification of Miriplatin by ICP-OES.....	65

	10
3.2.5 Quantification of Recovery of Platinum in Miriplatin-Loaded Nano Formulations by ICP-OES	65
3.2.6 Characterization of Miriplatin-Loaded Nano Formulations by TEM.....	66
3.3 Results and Discussion	66
3.3.1 Quantification of Miriplatin By HPLC	66
3.3.2 Mass Spectrometry of Miriplatin	69
3.3.3 Quantification of Miriplatin by ICP-OES.....	71
3.3.4 Recovery in the Quantification of Platinum from Miriplatin-Loaded Nano Formulations by ICP-OES	72
3.3.5 Morphology of Miriplatin-Loaded Nano Formulations.....	76
3.4 Summary	83
 Chapter 4: Evaluation of Anticancer Activity of Miriplatin-Loaded Nano Formulations	
Against 3D MCS.....	85
4.1 Introduction.....	85
4.2 Materials and Methods.....	88
4.2.1 Cell Culture Maintenance	88
4.2.2 Fluorometric Characterization of A549-iRFP Monolayer Cells.....	89
4.2.3 3D MCS Formation.....	89
4.2.4 Cell Viability Assays for Miriplatin-Loaded Nano Formulations on 3D MCS	90
4.3 Results and Discussion	91
4.3.1 Correlation of Fluorescent Signal in A549-iRFP Monolayer Cells with Cell Seeding Density and Cell Viability.....	91
4.3.2 Formation of 3D MCS	92

	11
4.3.3 Comparison between Sensitivity of A549 and that of A549-iRFP 3D MCS to Anticancer Drugs and Nano Formulations	93
4.3.4 Comparison of Anticancer Activity of Miriplatin-Loaded Nano Formulations Prepared by Different Methods	95
4.3.5 Anticancer Activity of Selected Miriplatin-Loaded Nano Formulations	98
4.4 Summary	101
Chapter 5: Summary and Future Work	103
REFERENCES	107

LIST OF TABLES

Table

2.1. Composition of Select Miriplatin-Loaded Lipid Nano Formulations.....	46
2.2. Composition, Size and PDI of SLNs with or without Miriplatin	52
2.3. Size and PDI of Miriplatin-Loaded Formulations with Different Lipid Compositions	53
2.4. Size and PDI of Miriplatin-Loaded SLNs Prepared by Different Preparation Procedures	55
2.5. Solubility of Miriplatin/Solid Lipids (TM/TP) in Co-Solvents	57
2.6. Composition, Size and PDI of Selected SLN Formulations Prepared by Co- Solvent Slow Evaporation Method.....	58
2.7. Composition, Size and PDI of Selected Micelle Formulations Prepared by Co-Solvent Slow Evaporation Method.....	58
3.1. Composition and Platinum Recovery of Miriplatin-Loaded SLNs Prepared by Different Preparation Procedures	74
3.2. Composition and Platinum Recovery of Selected SLN Formulations Prepared by Co-Solvent Slow Evaporation Method	76
3.3. Composition and Platinum Recovery of Selected Micelle Formulations Prepared by Co-Solvent Slow Evaporation Method	76
3.4. Comparison of Different Preparation Methods.....	84

LIST OF FIGURES

Figure

1.1. Lung cancer classification.....	20
1.2. Cisplatin structure and its mechanism of action	23
1.3. General structure of anticancer platinum agents.....	24
1.4. The family tree of platinum anticancer agents.....	25
1.5. Physiological Characteristics of Tumor Tissue and Vasculatures	27
1.6. Examples of lipid-based nanoparticles: micelles, liposomes and solid lipid nanoparticles (SLNs)	32
1.7. Proposed mechanism of action of miriplatin-loaded nano formulations-- passive targeting of miriplatin-loaded nano formulation to lung solid tumor.....	35
1.8. Proposed mechanism of action of miriplatin-loaded nano formulations-- cellular uptake of miriplatin-loaded nano formulation in lung solid tumor cells.....	35
2.1. Schematic representation of formation of lipid-based nanoparticles by solvent injection method.....	39
2.2. Schematic structures of miriplatin-loaded micelles (left) and miriplatin-loaded SLNs (right).	41
2.3. Schematic illustration of the chloroform dripping method.....	43
2.4. Schematic of co-solvent slow evaporation method.	45
2.5. An example of intensity-based size distribution of miriplatin-loaded SLN from Malvern Zetasizer software.	48
2.6. An example of volume-based size distribution of miriplatin-loaded SLN from Malvern Zetasizer software.	48
2.7. An example of number-based size distribution of miriplatin-loaded SLN from Malvern Zetasizer software.	49
2.8. An example of intensity-based size distribution of miriplatin-loaded micelle from Malvern Zetasizer software.	50

	14
2.9. An example of volume-based size distribution of miriplatin-loaded micelle from Malvern Zetasizer software.	50
2.10. An example of number-based size distribution of miriplatin-loaded micelle from Malvern Zetasizer software.	51
2.11. Solvent miscibility table	57
3.1. Diagram of a typical ICP-OES instrument with radial configuration of the detection system	62
3.2. Chromatograms of free miriplatin by HPLC.	67
3.3. Calibration curve of miriplatin UV absorbance at wavelengths 210 and 220 nm in HPLC.....	68
3.4. The change of AUC in calibration curve of miriplatin over time.	69
3.5. ESI-MS mass spectrum of miriplatin.....	70
3.6. Calibration curves of platinum standard solutions at wavelength 214.4 and 265.9 nm by ICP-OES.....	71
3.7. Calibration curves of different forms of platinum (platinum standard solution, cisplatin, miriplatin) at wavelength 214.4 nm by ICP-OES.....	72
3.8. TEM images of miriplatin-loaded micelles	77
3.9. TEM images of miriplatin/paclitaxel-loaded micelles.....	78
3.10. TEM images of miriplatin-loaded SLNs consisting of TP	79
3.11. TEM images of miriplatin-loaded SLNs consisting of TM.....	80
3.12. TEM images of miriplatin/paclitaxel loaded SLNs of TP	81
3.13. TEM images of miriplatin-loaded SLNs (TP) containing cholesterol.....	82
4.1. Schematic diagrams of the traditional two-dimensional monolayer cell culture (A) and three-dimensional cell culture systems (B, C)	87
4.2. Schematic diagrams of 3D MCS produced by seeding cells into 96-well microplate plates with noncell adherent surfaces	88
4.3. Correlation of iRFP fluorescent signal in A549-iRFP monolayer cells with cell seeding density (lower left) and with cell viability (lower right)	92

4.4. Morphology of A549-iRFP 3D MCS (3000 cells/well) after 5, 7, 9, 11, 13, 15 days of culturing (scale bar=500 μm).....	93
4.5. Cell viability of A549 (blue) and A549-iRFP (red) 3D MCS after 3-day exposure to cisplatin plus 4-day cisplatin-free growth.....	94
4.6. Cell viability of A549 (blue) and A549-iRFP (red) 3D MCS after 3-day exposure to miriplatin-loaded formulations plus 4-day drug-free growth	95
4.7. Cell viability of A549-iRFP 3D MCS after 3-day exposure to miriplatin-loaded nano formulation prepared by different methods at 400 μM input platinum concentration and 4-day platinum-free growth	97
4.8. Growth inhibition of A549-iRFP 3D MCS after 3-day exposure to miriplatin-loaded nano formulation prepared by different methods at 400 μM input platinum concentration and 4-day platinum-free growth	98
4.9. Cell viability of A549-iRFP 3D MCS after 3-day exposure to miriplatin-loaded nano formulations prepared by the co-solvent slow evaporation method and 4-day drug-free growth.....	100
4.10. The dynamic change of iRFP fluorescent signal of A549-iRFP 3D MCS after 3-day exposure to miriplatin-loaded nano formulations prepared by co-solvent slow evaporation and 4-day drug-free growth.....	101

LIST OF ABBREVIATIONS

AR	aspect ratio
AUC	area under curve
CBDCA	1,1-cyclobutanedicarboxylate
Chol	cholesterol
CMC	critical micelle concentration
CTR1	copper transporter proteins
DACH	1R,2R-diaminocyclohexane
DLS	dynamic light scattering
EGFR	epidermal growth factor receptor
EPR	enhanced permeation and retention effect
ESI-MS	electrospray ionization mass spectrometry
FDA	Food and Drug Administration
HCC	hepatocellular carcinoma
HEPES	4-(2-hydroxyethyl)-1-piperazineethanesulfonic acid
HPLC	high performance liquid chromatography
ICP-MS	inductively coupled plasma mass spectrometry

ICP-OES	inductively coupled plasma-optical emission spectrometry
IC50	fifty percent inhibitory concentration
IPA	isopropanol
IV	intravenous
iRFP	near-infrared fluorescent protein
LOD	limit of detection
Miri	miriplatin
MS	mass spectrometry
NSCLC	non-small cell lung cancer
PDI	polydispersity index
PDX	patient-derived xenograft
PEG	polyethylene glycol
PE-PEG ₂₀₀₀	1,2-distearoyl-sn-glycero-3-phosphoethanolamine-N- [methoxy (polyethylene glycol)-2000] (ammonium salt)
PS	performance status
PTX	paclitaxel
QC	quality control
RES	reticuloendothelial system

RGD	arginylglycylaspartic acid
SCLC	small cell lung cancer
SLN	solid lipid nanoparticle
TEM	transmission electron microscopy
TM	trimyristin
TME	tumor microenvironment
TP	tripalmitin
2D	two-dimensional
3D MCS	three-dimensional multicellular spheroid

CHAPTER 1: INTRODUCTION

1.1 Statement of the Problem

1.1.1 Lung Cancer

Cancer is a group of diseases which are characterized by the uncontrolled growth and spread of abnormal cells [1]. Based on the latest updated data, cancer is the second leading cause of death and is responsible for approximately 9.6 million deaths in 2018 [2]. More than 1.8 million new cancer cases are expected to be diagnosed and about 606,520 Americans are expected to die from cancer in 2020 [1]. Among all oncological diseases, lung cancer claims the highest mortality (male: 23.5%; female: 22%) and the second most new cases (male: 13%; female: 12%) in the US [3]. Smoking tobacco is the leading cause of lung cancer but non-smokers can also be diagnosed with lung cancer if they are exposed to other risk factors such as radon, secondhand smoke, air pollution, asbestos and certain chemicals [4]. Personal and family history of lung cancer is also a risk factor even for nonsmokers and light smokers.

Based on histological features, lung cancer can be classified into two types: non-small cell lung cancer (NSCLC) and small cell lung cancer (SCLC). NSCLC is the most prevalent type (85% of total cases) and has three main subtypes, namely adenocarcinoma, squamous cell carcinoma and large-cell carcinoma (Figure 1.1) [5]. Adenocarcinoma represents about 60-70% of NSCLC and tends to develop into solid tumors in peripheral bronchioles, which are usually located more along the outer edges of the lungs. Squamous cell carcinoma comprises about 30% of NSCLC and tends to arise in main bronchi and then advance to the carina [6]. Large-cell carcinoma is more proximal in location and locally tends to develop tumors that lack the common glandular or squamous morphology. SCLC is derived from the lung hormonal cells and

accounts for the remaining 15% of lung cancer. It tends to develop into central mediastinal tumors and disseminate aggressively into submucosal lymphatic vessels and nodes [5, 7].

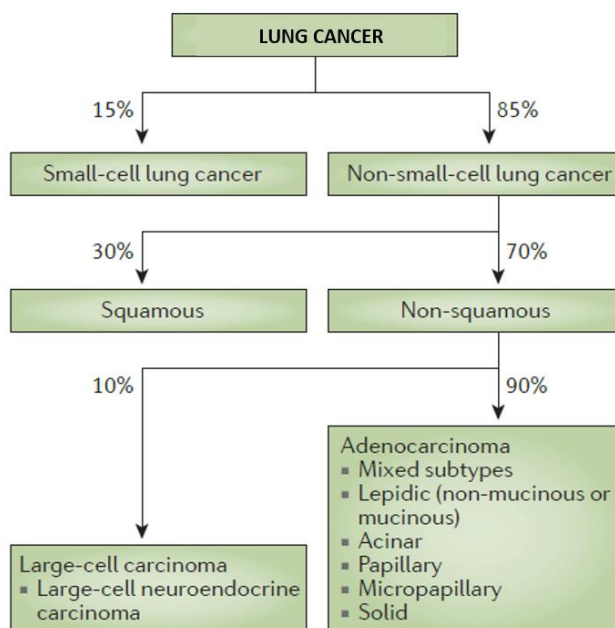


Figure 1.1. Lung cancer classification. Adapted from [8].

1.1.2 Treatment Options and Chemotherapy

The treatment of lung cancer includes surgery, radiotherapy, chemotherapy, targeted therapy and immunotherapy. The diagnosis of the histological subtypes and the stages of progression are important for designing the treatment. Patients in stage I, II, and IIIA are typically suggested to have surgery to remove the tumor if the tumor is resectable and if the patients can tolerate the surgery [9, 10]. Some patients may benefit from adjuvant therapy, which includes radiation, chemotherapy, and targeted therapy, before or after the resection surgery. If the tumor is too large, doctor may recommend using adjuvant therapy to shrink the tumor size before surgery. Patients also receive chemotherapy after surgery to kill the remaining

cancer cells and to reduce the risk of cancer relapse [11, 12]. Radiotherapy can help control or eliminate tumors at specific sites using high-energy beams to damage DNA of cancer cells. Radiotherapy also serves as part of palliative care to patients who do not respond to surgery or chemotherapy [13]. Immunotherapy is a breakthrough treatment in oncology that uses people's own defense system to fight off cancer [14]. Generally, it can prevent cancer cells from spreading to other regions of the body and can increase the effectiveness of the immune system by targeting cancer cells to stop/slow their growth [15]. Immunotherapy treatments are typically reserved for patients who have both local, advanced lung cancers and cancer cells have spread to remote parts of the body. Targeted drug treatments focus on abnormalities that are specific to the cancer cells and aim to block these abnormalities, such as epidermal growth factor receptor (EGFR) mutations.

However, approximately 40% of newly diagnosed lung cancer patients are in stage IV and the goal for treating these patients is to improve their survival time and to reduce disease-related adverse events [10]. Cytotoxic combination chemotherapy is the first-line therapy for both advanced-stage NSCLC and advanced-stage SCLC [16, 17]. A platinum-based anticancer drug (cisplatin or carboplatin) plus paclitaxel, gemcitabine, docetaxel, vinorelbine, irinotecan, or pemetrexed are usually given in a series of treatments over a period of weeks or months, with breaks in between so that patients can recover [12, 18]. The specific combination depends on different cancer types, performance status (PS), toxic effects and should be decided on an individual basis [10]. Patients with performance status of 0, 1 or 2 are usually suggested to take a platinum-based regimen, but patients with a PS of 3 do not benefit from cytotoxic chemotherapy because of the high risk of adverse effects [10]. Therefore, a platinum-based

combination chemotherapy plays a major role in lung cancer treatment, either by itself or in combination with surgery or radiotherapy.

1.1.3 Platinum-Based Anticancer Drugs

The discovery of cisplatin and subsequent expansion of the platinum-based drug family has revolutionized the treatment of lung cancer and other certain cancers. Platinum-based chemotherapy drugs account for approximately 50% of clinically used anticancer therapeutic agents [19]. Cisplatin was initially discovered as an antibacterial agent over 50 years ago and later found to have potent anticancer effects over a wide range of cancers [20]. Cisplatin was named by Dr. Rosenberg and approved by the US Food and Drug Administration (FDA) for cancer treatment in 1978.

Cisplatin is administered to patients by intravenous infusion in saline solution either individually or in combination with another therapeutic agent. The general mechanism of cisplatin involves four steps (Figure 1.2): (1) cellular uptake, (2) aquation/activation, (3) DNA binding, and (4) apoptosis [21, 22]. When administered in bloodstream, cisplatin is relatively stable and remains its initial chemical state due to the high concentration of chloride ion (~100 mM) [23]. It enters cells via passive diffusion or active transport by membrane transporters, such as copper transporter proteins CTR1 [24]. Once inside cells, cisplatin undergoes aquation/activation process, where the chlorine ligands of cisplatin are easily displaced by water molecules due to the lower intracellular chloride concentration (~4-12 mM) [21, 25]. The positively charged Pt-water complex ion is attracted to the negatively charged DNA, where it binds to the nitrogen in the N7 position on purine bases (guanine and adenine) to form the cross-link adduct [26, 27]. The cells will then undergo apoptosis unless they promptly repair the

damage. The cross-linking process is crucial to the cytotoxicity of cisplatin [28]. It is reported that the number of the formation of Pt-DNA adduct can directly determine the cytotoxic effect [19].

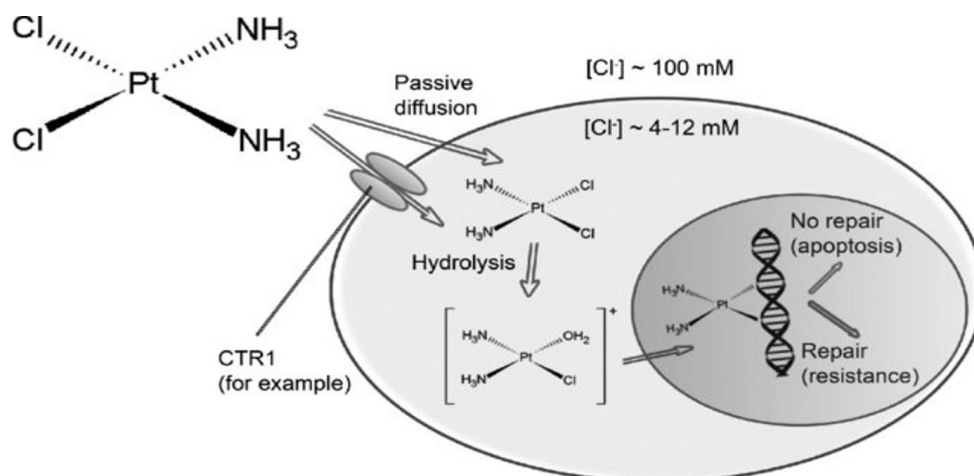


Figure 1.2. Cisplatin structure and its mechanism of action. Adapted from [19].

However, systemic administration of cisplatin also produces many severe adverse effects, ranging from hearing loss to hemolysis [19]. Neurotoxicity is the major dose-limiting side effect, which is a composite result of the transport of cisplatin into renal epithelial cells, injury to DNA, activation of a multiple cell death and survival pathways and initiation of a robust inflammatory response [29, 30]. Other common adverse effects including neurotoxicity and ototoxicity are caused by the limited selectivity of cisplatin between normal cells and cancer cells. Another major challenge of cisplatin is the rapid development of resistance. When stressed with cisplatin, cancer cells can reduce the expression of the transporter that uptake cisplatin (CTR1) and increase the production of glutathione to enhance DNA repair [31-33], both contributing to drug resistance.

To overcome the toxicity and the resistance of cisplatin, many more platinum complexes have been investigated for their antitumor properties. The design of new platinum-based anticancer agents involves strategic modification of several structural features (Figure 1.3) [34]. The non-leaving group ligands L of a platinum complex are typically nitrogen donors and form thermodynamically stable bond with the platinum. Such non-leaving ligands usually maintain unchanged during the drug activation and directly affect the nature of the final platinum-DNA adduct [35, 36]. The leaving group ligands X, commonly halides and carboxylates, are labile and can be replaced through ligand substitution. Modification of ligand X can change the aquation/activation kinetics, toxicity profile and solubility [35, 36]. The axial ligands R are only present in higher-valent platinum complexes, such as platinum (III) and platinum (IV). These ligands will ultimately dissociate after biological reduction but can be used for tumor-targeting or for attachment to nanoparticles [34]. Any modification of these three types of ligands will also change the platinum molecule's lipophilicity and solubility, which are important physicochemical parameters for drug design and drug delivery.

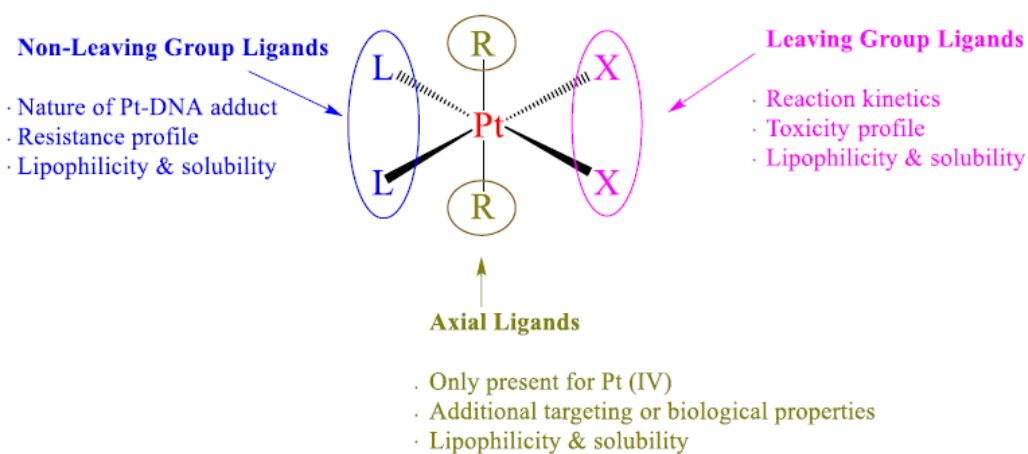


Figure 1.3. General structure of anticancer platinum agents. Adapted from [34].

Although over a thousand platinum complexes have been synthesized and tested for anticancer activity, only two platinum drugs are approved for clinical use worldwide and four additional compounds approved for regional use in Asia [21, 37].

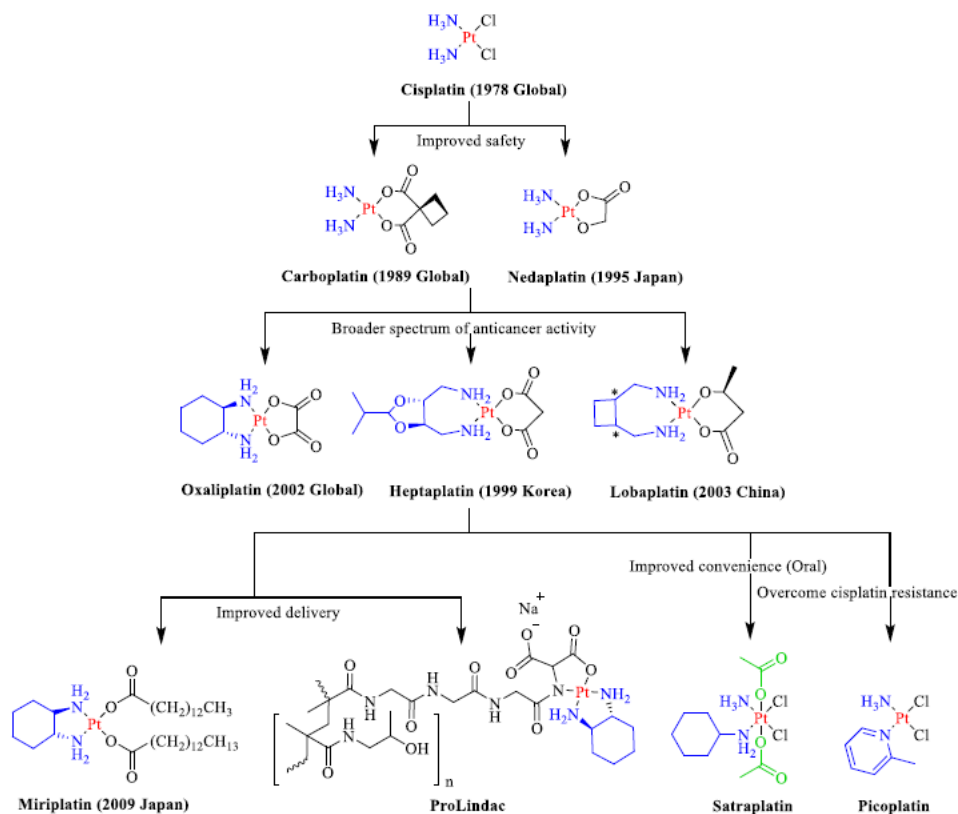


Figure 1.4. The family tree of platinum anticancer agents. Copyright from [22].

Carboplatin was approved by FDA in 1989 as a second-generation Platinum-based drug [37, 38]. It contains the same non-leaving group as cisplatin but a different leaving group, chelating 1,1-cyclobutanedicarboxylate (CBDCA), which leads to a lower toxicity profile. Although carboplatin can be administered at a higher dosage than cisplatin, it exhibits cross-resistance with cisplatin because they share the same non-leaving group [39, 40]. Oxaliplatin

gained FDA approval for treatment of colon cancer in 2002 as a third generation of platinum-based anticancer drug [37, 38]. Oxaliplatin has another chelating ligand (oxalate) as the leaving group and a different non-leaving group, 1R,2R-diaminocyclohexane (DACH), which exhibits a different spectrum of anticancer activity [41]. Because of the different non-leaving group, oxaliplatin usually showed no cross-resistance with cisplatin. Further, oxaliplatin needs to be activated by replacing the oxalate ligand with chloride ion [42]. It has been reported that oxaliplatin is more dependent on organic cation transporters (overexpressed in colon cancer) than copper transporters for uptake by cancer cells [24, 43]. Oxaliplatin is the first clinically approved platinum drug that can overcome cisplatin resistance. In addition, nedaplatin, heptaplatin and lobaplatin have been approved in Japan, South Korea and China, respectively, as alternatives of cisplatin [37, 38].

Miriplatin was approved in Japan for lipiodolization in the treatment of hepatocellular carcinoma (HCC) in 2009. It has the same non-leaving group as oxaliplatin and two myristate chains as leaving groups, which makes miriplatin a highly lipophilic complex. In clinic, it is administered into the hepatic artery using an oily lymphographic agent, Lipiodol Ultra-Fluide® as a carrier to release the active platinum compounds into the aqueous phase gradually, which is similar to the transformation of oxaliplatin. Miriplatin can be considered as a fourth generation of platinum drug to improve delivery and reduce toxicity, especially in liver [44].

1.1.4 Barriers of Drug Delivery into Solid Tumor

The limitations of anticancer chemotherapy have been primarily ascribed to drug toxicity and drug resistance at the cellular level. However, substantial evidence suggests that tumor microenvironment (TME) also mediates resistance of solid tumors against chemotherapy [45].

As in many solid tumors, the TME of NSCLC exhibits many distinctive physiological characteristics (Figure 1.5) which are different from normal tissue, including vascular structure, interstitial pressure, and multiple gradients of cell proliferation, nutrients, oxygen and therapeutic agents [46, 47]. In normal tissues, drug molecules with low molecular weight can enter the vascular network and readily perfuse the tissues due to the concentration gradient[48]. By contrast, the distribution of many anticancer drugs is heterogeneous in solid tumors. The insufficient penetration prevents a high proportion of the tumor cells from exposure to potentially lethal concentration of the anticancer drug, especially deep in the core of the solid tumors.

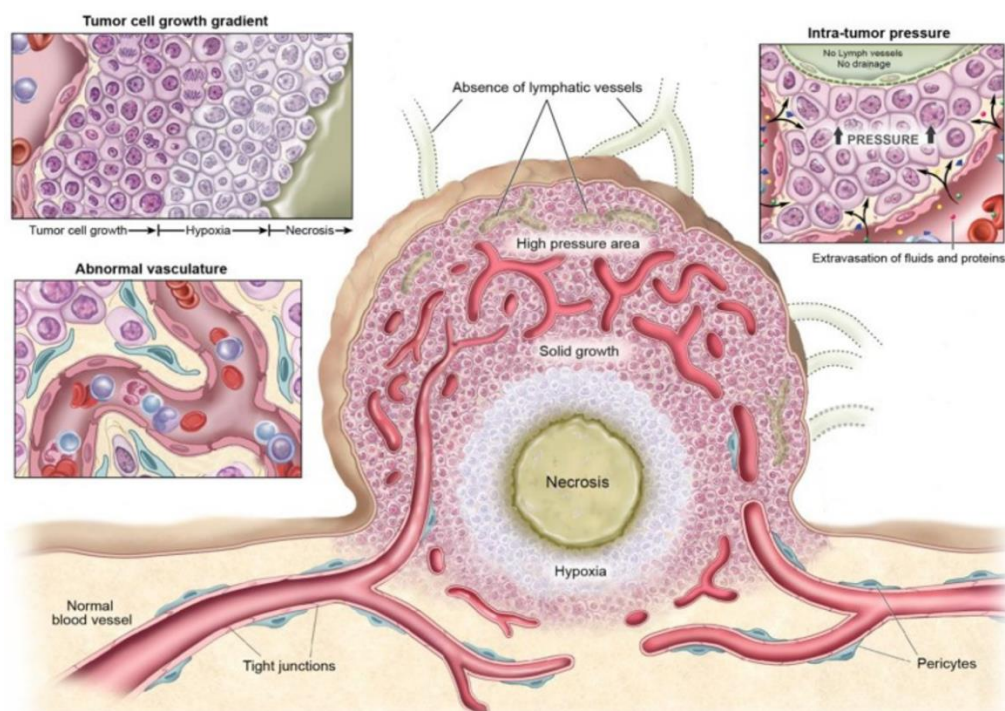


Figure 1.5. Physiological Characteristics of Tumor Tissue and Vasculatures. Adapted from [48].

Solid tumors can be seen as heterogeneous organ-like structural complex consisting of cancer cells and stromal cells [45]. Compared with normal tissues, the tumor stroma contains an altered extracellular matrix and an increased number of fibroblasts that synthesize growth factors, chemokines, and adhesion molecules [45, 49]. The tumor stroma, which varies greatly among tumors, can influence malignant transformation, cancer invasion and metastasis, and the sensitivity to drug treatment [50-52]. In addition, a tumor's response to chemotherapy is also influenced by its abnormal vasculature and blood flow. Unlike normal tissue, tumor microvasculature shows disorganization and lack of the conventional hierarchy of blood vessels, which interferes with the homogeneous distribution of anticancer drugs within tumor [53, 54]. For an example, the leaky blood vessels in solid tumor allow macromolecules to reach tumor cells but also cause high interstitial pressures, which inhibits the drug accumulation [55]. Furthermore, the lack of functional intratumoral lymphatic vessels inhibits the clearance of extracellular fluid, further contributing to interstitial hypertension within tumors [56]. These structural abnormalities of tumor blood vessels are the main reason of the heterogeneity of blood supply and cell proliferation within the tumor microenvironment.

In summary, several characteristics of solid tumors in lung cancer constitute a physiochemical barrier to the homogenous distribution and deep penetration of chemotherapy agents.

1.2 Strategies for Effective Drug Delivery to Solid Tumors

Nanotechnology provides a promising platform to overcome the aforementioned physiochemical barrier against intratumoral drug distribution and to reduce the systemic toxicity of anticancer chemotherapy. Generally, nanocarriers are colloidal drug carrier systems with size

usually less than 500 nm in diameter. They are used for encapsulation and delivery of hydrophilic and/or hydrophobic drug molecule(s) to improve their bioavailability and therapeutic efficacy. Compared with chemotherapeutic agents with low molecular weight, nano drug delivery systems can help to improve solubility, stability, pharmacokinetic profile, drug release, and drug targeting [57].

1.2.1 Passive Targeting

Passive targeting, also known as physical targeting, can enhance the accumulation of therapeutic agent at the target site by catering the physicochemical properties of the drug delivery system to the distinctive characteristics of the pathologic tissue [47]. The enhanced permeation and retention (EPR) effect, which was proposed as an innovative strategy to deliver macromolecular drugs in 1986, is one mechanism of passive targeting [58]. The enhanced permeation of nanocarriers or macromolecules at the tumor site is caused by tumor vascular leakage while the enhanced retention is due to the impaired lymphatic drainage within neoplastic tissues [59]. Compared to tightly aligned normal vasculature with 10 nm or smaller fenestrae, the blood vessels inside solid tumors contain large fenestrae ranging from 100 to 700 nm in diameter, which enables selective extravasation of nanocarriers into the tumor interstitium [57]. The leaky tumor vasculature also allows excessive fluid extravasation, which generates high interstitial pressure and non-functional lymphatic drainage, which in turn enhances the retention of nanocarriers inside solid tumors [48, 60]. Hence, the increased vascular permeability and poor lymphatic drainage results in the selective accumulation and retention of nanocarriers in tumor tissues.

The cut-off size for the extravasation varies, but 200 nm in diameter or below is generally accepted for the solid tumor vasculature [61]. In order to achieve a sufficient accumulation of nanocarriers at tumor site, polyethylene glycol (PEG) is usually used to modify the surface of nanocarriers to extend their time of circulation in blood. The hydrophilic PEG polymer can hinder the adsorption of serum proteins (opsonization) and thus hinder their recognition and clearance by the reticuloendothelial system (RES) [62]. Therefore, when administered intravenously, PEG-coated nano delivery systems tend to circulate for longer time if they are not small enough (40 kDa) to be excreted by renal filtration or large enough to be recognized by the RES [48, 63].

Although the EPR effect is thought to significantly benefit nanocarriers, including Doxil®, Caelyx® and Abraxane® [48], which are now in clinical use, there are several challenges in this mechanism of passive targeting for anticancer drug delivery. Compared to normal organs, the EPR effect may provide only modest tumor specificity of 20–30% increase in drug delivery [48, 64]. In addition, the benefit of the EPR effect varies by tumor types and depends on the following factors: (1) the degree of angiogenesis and lymphangiogenesis; (2) the degree of perivascular tumor growth and the density of the stromal response; and (3) intratumor pressure [48]. Together with the physicochemical characteristics of nanocarriers, all these factors will affect the drug delivery efficiency. Some researchers also proposed three methods that might improve the EPR effect: (1) modulating tumor blood flow; (2) modulating the tumor vasculature and stroma; and (3) killing cancer cells to reduce the barrier function of solid tumors [48, 65].

1.2.2 Active Targeting

Active targeting is strategies of grafting or tagging nanocarriers with targeting ligands, which can specifically bind to over-expressed receptors on the surface of tumor cells. Compared to passive targeting, active targeting can help deliver more drug molecules into targeted cells by receptor-mediated endocytosis instead of interstitial accumulation [64]. The strong and highly selective interaction between the ligand and receptor can decrease non-specific binding and toxicity in normal tissues. It has been reported that the involvement of receptor-mediated endocytosis can also suppress multidrug resistance because it circumvents drug efflux by P-glycoprotein [66]. The first proof of concept for the strategy of active targeting was published in 1980 in a report on liposomes grafted with antibodies [67]. A numbers of receptors have been found to be overexpressed in cancer cells, followed by investigations on their binding ligands for active targeting, including proteins, peptides, polysaccharides, aptamers and small molecules [64, 68-70]. For example, it has been found that RGD peptide binds to $\alpha V\beta 3$ integrin, which are highly presented on both the glioma cells and vasculature of TME [71].

1.2.3 Lipid-Based Nanocarriers

Nano drug carriers can be classified into organic and inorganic nanoparticles. Compared with inorganic nanoparticles, such as mesoporous silica nanoparticles and gold nanoparticles, organic nanoparticles are more commonly used due to their better biocompatibility. Phospholipids are the major component of the cell membrane, so they commonly serve as biocompatible and biodegradable key components organic nanoparticles for drug delivery. Approximately 40% of lipophilic drug candidates fail due to poor water solubility or formulation stability issues. Lipid-based nanoparticles can help formulate those molecules and help deliver

and release them at the target site of action to lower both acute and chronic toxicity [72, 73].

Based on the lipid composition and the nano-sized structure, lipid-based nanoparticles mainly include micelles, liposomes, solid lipid nanoparticles (SLNs) (Figure 1.6).

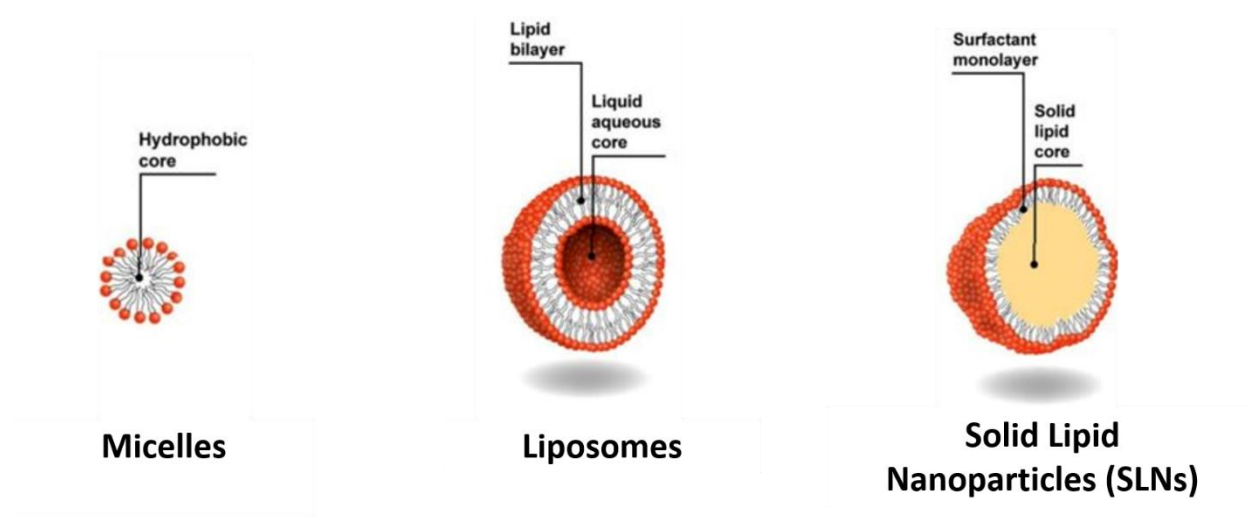


Figure 1.6. Examples of lipid-based nanoparticles: micelles, liposomes and solid lipid nanoparticles (SLNs). Adapted from [74].

Additionally, the physiochemical properties of lipid-based nanocarriers can be catered to the unique characteristics of solid tumors in order to increase the efficiency of drug targeting and delivery [73]. Based on the cut-off size for renal excretion and tumor permeation as mentioned before, a size range between 10 to 100 nm would be optimal for drug targeting and delivery. Neutral or negatively charged surface of nanocarriers is preferred to prolong circulation time and reduce renal clearance [75]. It is well known that a spherical shape promotes cellular interaction and cellular uptake [76]. However, it has also been reported that rod-shaped structures might be internalized more efficiently than spherical structures [77, 78]. Furthermore, nanocarriers are commonly modified with the hydrophilic polymer PEG to reduce opsonization and thus to prolong circulation [79].

1.2.3.1 Micelles. Micelles are spherical colloids consisting of a core of nonpolar groups of its surfactant monomers and a surface of polar groups of the same surfactant monomers. Depending on the structure of the monomers, the size of the micelle varies from 10 nm to 100-200 nm [80]. For an example, micelles made of lipid-PEG conjugates usually have a size of no more than 20 nm in diameter [81, 82]. The extremely small size of micelles might be beneficial to the tumor penetration and accumulation. Compared to other nanoparticles, micelles usually form at higher concentration of the monomers, which is known as critical micelle concentration (CMC). The usually high CMC value of micelles might lead to their insufficient stability *in vivo*.

1.2.3.2 Liposomes. Liposomes are the most commonly used nanocarriers and represent the majority of FDA-approved nanomedicines for cancer therapy. Liposomes are mainly composed of phospholipids and has the structure of a shell of lipid bilayer enclosing an aqueous interior, which allows the loading of both lipophilic and hydrophilic drug molecules [83, 84]. Hydrophilic molecules can be encapsulated in the aqueous core while lipophilic molecules can be incorporated into the lipid bilayer. Compared to micelles, liposomes have a larger size ranging from 50 to 500 nm. The size and surface charge of a liposome preparation depend on both the lipid composition and the preparation method. Liposomes can be modified by PEG polymer and targeting ligands on the surface in order to prolong circulation time and to increase tumor accumulation. The *in vivo* stability and the drug loading for hydrophilic drugs of liposomes are still challenging. It was reported that the encapsulation of hydrophobic drugs inside the aqueous core destabilized the lipid bilayer structure resulting in drug leakage and colloidal instability [85]. In order to overcome the instability caused by opsonization, tremendous researches focused on modifying liposomes with hydrophilic molecules such as PEG

or monosialoganglioside to generate “stealth liposomes” that can evade the recognition and clearance by RES [86, 87].

1.2.3.3 Solid lipid nanoparticles (SLNs). SLNs are nanocarriers containing a hydrophobic core of solidified lipid molecules. SLNs carry a size ranging from 50 to 1000 nm in diameter [74, 88]. SLNs have the flexibility of size and surface modification. The major components of SLNs are solid lipids such as triglycerides, free fatty acids, fatty acid alcohols, waxes and steroids, which are all used for dispersion and entrapment of hydrophobic drugs. The solidification/crystallization of the lipids sometimes results in particles with non-spherical shape [74]. The solid lipid molecules are solid at room and body temperatures, which means that SLNs have much better stability than micelles and liposomes. Besides the excellent physical stability, SLNs also have the advantages of sustained drug release, high drug loading capacity and biodegradability [89].

1.3 Miriplatin-Loaded Nano Formulations and their Proposed Mechanism of Action

Due to the highly lipophilic structure and compatibility with phospholipid and solid lipid molecules, miriplatin can be formulated into various lipid-based nanocarriers. The appropriate physiochemical properties will allow nanocarriers to passively target to lung solid tumors. After they reach cancer cells, miriplatin will enter cancer cells either by endocytosis together with nanocarriers or by diffusion by itself. The myristate chains of miriplatin will be replaced by chloride ions to transform miriplatin into smaller, active platinum-containing compounds, followed by further activation by water molecules and crosslinking with DNA to kill cancer cells.

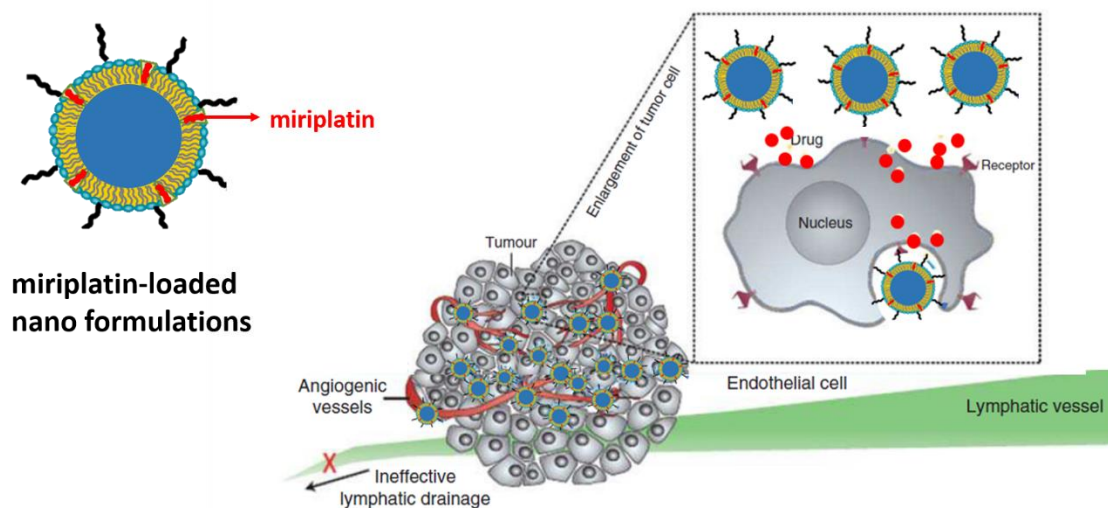


Figure 1.7. Proposed mechanism of action of miriplatin-loaded nano formulations--passive targeting of miriplatin-loaded nano formulation to lung solid tumor.

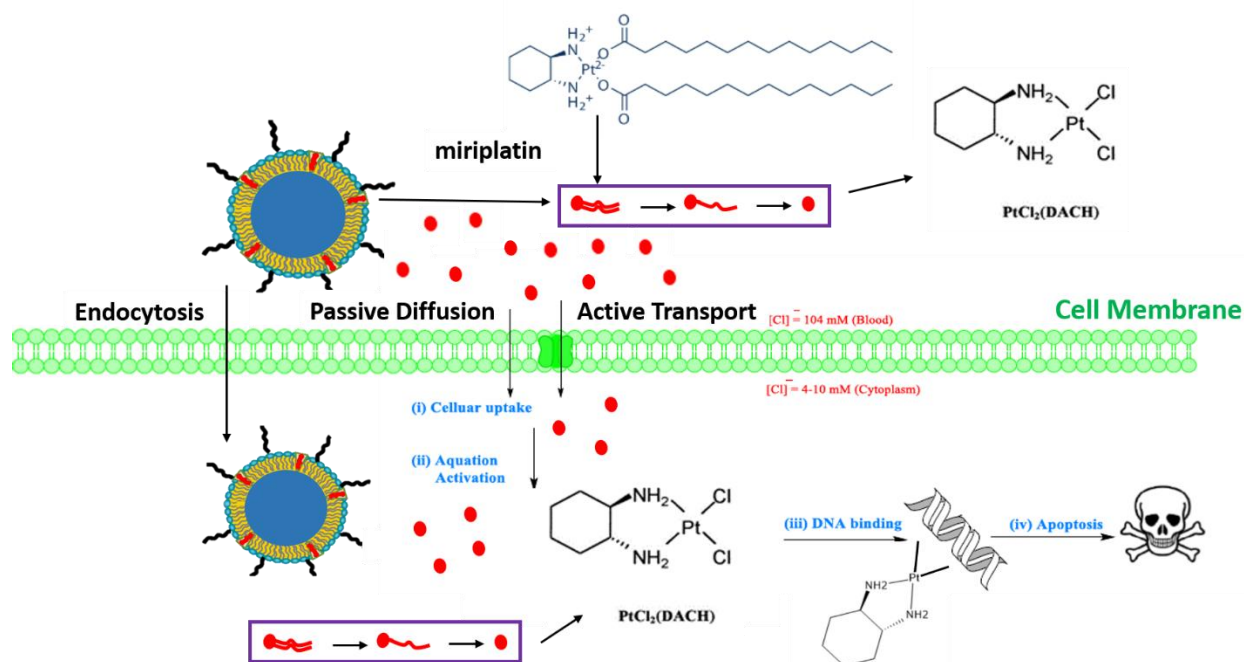


Figure 1.8. Proposed mechanism of action of miriplatin-loaded nano formulations--cellular uptake of miriplatin-loaded nano formulation in lung solid tumor cells.

1.4 Hypothesis and Specific Aims

Based on the foregoing, we hypothesize that lipid-based nano formulations of miriplatin would carry appropriate physiochemical properties to improve the anticancer activity of platinum drugs against lung cancer. To test the hypothesis, the research of this thesis is focused on the following specific aims:

1. To develop a methodology to construct miriplatin-loaded nano formulations;
2. To characterize the physiochemical properties and the morphology of miriplatin-loaded nano formulations;
3. To evaluate the anticancer activity of miriplatin-loaded formulations against three-dimensional multicellular spheroids (3D MCS).

CHAPTER 2: PREPARATION OF MIRIPLATIN-LOADED NANO FORMULATIONS

2.1 Introduction

2.1.1 Strategies to Prepare Nano Formulations

It is widely known that lipid-based nanoparticles are mainly composed of natural or synthetic lipids. Due to the lipid molecules' amphiphilic property, they tend to form aggregation like nanoparticles or microparticles when they are exposed to aqueous phase in order to minimize the exposure of their hydrophobic moieties to water molecules [90].

Numerous techniques have been developed to prepare lipid-based nano formulations, such as thin film hydration method, ethanol injection method, solvent evaporation method, microfluidic technique, and high pressure/hot homogenization technique. The main challenges are to control the energy input during the preparation of nanoparticles and to apply appropriate lipid-to-drug and organic phase-to-aqueous phase ratios [91, 92].

In research labs, some preparation methods such as thin film hydration are easily executed but can only prepare nano formulations in small scale. Generally, lipids and hydrophobic drugs are dissolved into a volatile organic solvent or mixture of organic solvents [93]. After evaporating the organic solvent(s) under reduced pressure to form a thin film, aqueous buffer is added at temperature above the lipid transition temperature followed by free-thawing and membrane extrusion. It is difficult for human eyes to assess the quality of the thin film, such as homogeneity and thickness, so the batch-to-batch reproducibility can be a huge challenge.

In industry, solvent injection is the most commonly used way to prepare nano formulations. Generally, lipids dissolved in organic solvent(s) (eg. ethanol) is injected into aqueous phase slowly at a temperature above the transition temperature of the lipids. The size of the lipid-based formulations prepared by this technique can be controlled by adjusting the speed of injection, which determines the ratio of organic phase/aqueous phase during the mixing. The outcome of solvent injection can also be explained by two crucial speeds [94] – the speed at which the lipids and hydrophobic cargo drug molecules precipitate from the organic phase and the speed at which they form particle in aqueous phase. Application of appropriate injection speed to control these two speeds can facilitate the preparation of nanoparticles with optimal size and can reduce material loss during the preparation. The solvent evaporation method can be seen as a modified solvent injection method, in which the water-immiscible organic solvent is emulsified in aqueous phase by injection, but by stirring at high speed [93]. The two crucial speeds of lipid/cargo precipitation and formation of particles are controlled by the evaporation of organic solvent. The residual organic solvent need to be removed completely, otherwise it will damage biomolecules and tissues once the formulations are administrated to patients [93].

Other commonly used methods such as microfluidic technique and spray-drying method share similar mechanism to the two methods mentioned previously but need more specialized instruments [92, 93, 95].

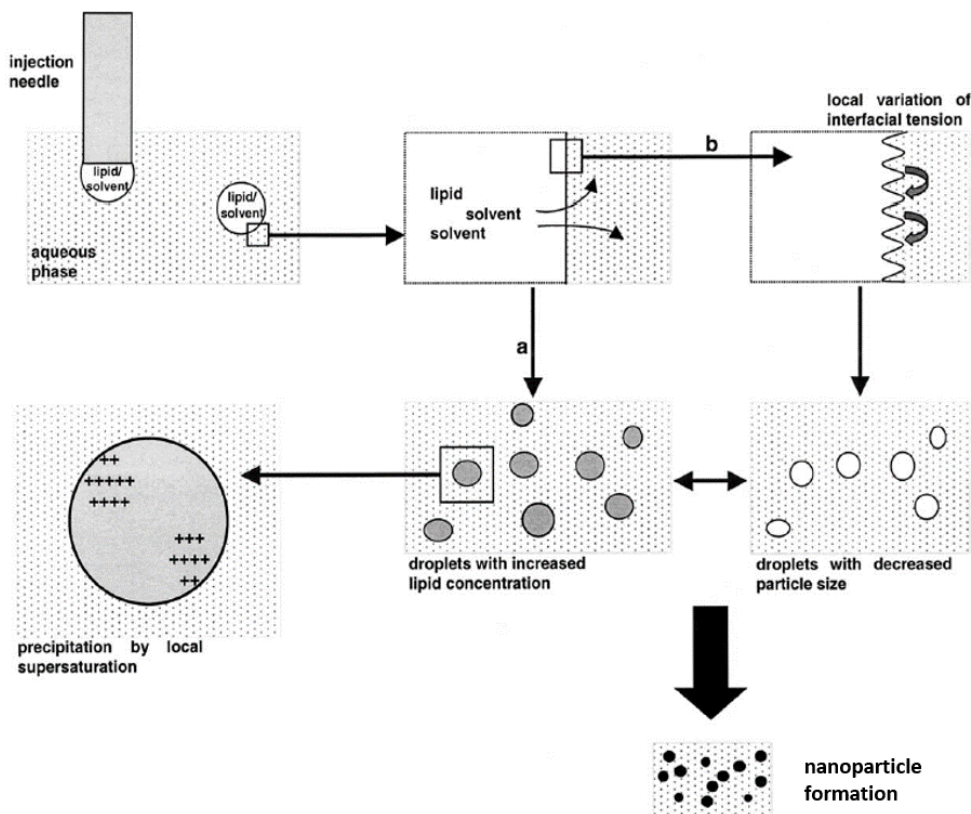


Figure 2.1. Schematic representation of formation of lipid-based nanoparticles by solvent injection method [94].

2.1.2 Components of Miriplatin-Loaded Formulations

Miriplatin is a highly lipophilic platinum anticancer drug containing myristates (C-14 fatty acid) as leaving groups and diaminocyclohexane (DACH) as a carrier ligand [96]. The two C-14 chains greatly influence the solubility of miriplatin and make it similar to the structure of lipids, especially phospholipids. In this way, miriplatin can not only be considered as an anticancer drug but also a lipidic component inside our formulations.

It is well acknowledged that combination therapy (IV infusion with two anticancer drugs together or sequentially) can achieve significantly better anticancer efficacy and lower toxicity in clinic cancer treatment [97]. In this study, paclitaxel (PTX) will be used as a secondary

anticancer drug inside the lipid nano formulations because the chemotherapy regimens with platinum-based drugs (cisplatin or carboplatin) and paclitaxel are first-line treatments for non-small cell lung cancer. Paclitaxel, another hydrophobic drug molecule, can be easily formulated into the lipophilic core of lipid-based nano formulations such as micelles and solid lipid nanoparticles [82, 98, 99].

Trimyristin (TM) and tripalmitin (TP) are triglycerides synthesized by formal acylation of the three hydroxy groups of glycerol by myristic (tetradecanoic) acid and palmitic (hexadecanoic) acid, respectively. Both TM and TP have already been widely utilized as major components of solid lipid nanoparticles [99, 100]. Paclitaxel-loaded SLN of tripalmitin have also been successfully prepared and studied by some researchers [99]. TM and TP have similar length of carbon chains to miriplatin so we expect that they both would be easily compatible with miriplatin to form lipid nanoparticles.

18:0 PE-PEG₂₀₀₀ is a commonly used pegylated lipid in nano formulations to prolong circulation time, increase stability and reduce opsonization. In addition, because it is an amphiphilic polymeric molecule, it can form spherical colloidal nanoparticles such as micelles by self-assembly [82, 98].

In this study, various miriplatin-loaded formulations such as micelles and SLNs have been prepared and characterized by size and polydispersity index (PDI). Miriplatin-loaded micelles were prepared with 18:0 PE-PEG₂₀₀₀ only, while miriplatin-loaded SLNs were prepared with triglycerides (TM or TP) and 18:0 PE-PEG₂₀₀₀. Miriplatin or miriplatin/paclitaxel are used as anticancer payload drug(s) of the nano formulations. In addition, several scale-up preparation methods (including solvent injection and solvent evaporation) for miriplatin-loaded nano

formulations were investigated. Due to the poor solubility of miriplatin in most organic solvents, chloroform was chosen as the major component of the organic phase to dissolve miriplatin. The preparation methods will be discussed one by one in this chapter and summarized in a table at the end of Chapter 3.

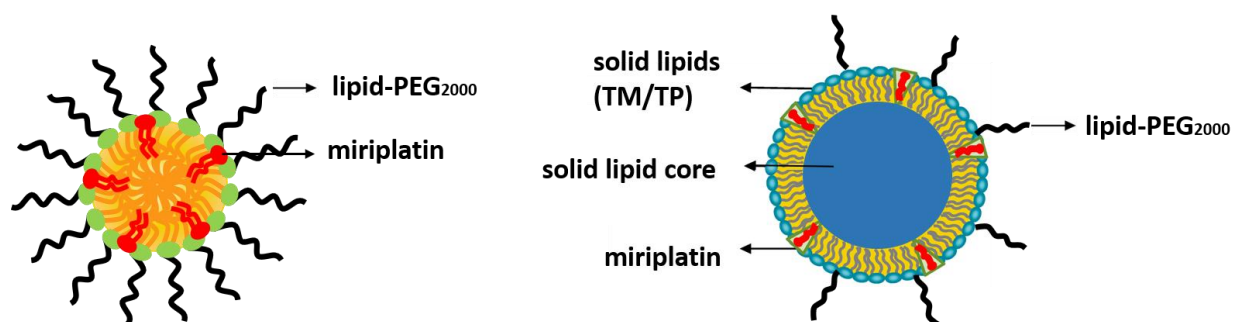


Figure 2.2. Schematic structures of miriplatin-loaded micelles (left) and miriplatin-loaded SLNs (right).

2.2 Materials and Methods

2.2.1 Materials

1,2-distearoyl-sn-glycero-3-phosphoethanolamine-N-[methoxy(polyethylene glycol)-2000] ammonium salt (18:0 PEG2000 PE) was purchased from Avanti Polar Lipids, Inc. (Alabaster, AL, USA). Miriplatin was purchased from MedChemExpress LLC (NJ, USA). Cholesterol, Glycerol trimyristate, Glycerol tripalmitate were purchased from Sigma-Aldrich. 2-[4-(2-hydroxyethyl) piperazin-1-yl]-ethanesulfonic acid (HEPES) was purchased from Fisher Scientific. All other organic solvent and chemicals were purchased from Sigma Aldrich, Fisher Scientific or VWR.

2.2.2 Preparation Methods for Miriplatin-Loaded Formulations

2.2.2.1 Preparation of miriplatin-loaded formulations by film hydration. A solution of 4 μmol various lipids and additional 0.8 μmol miriplatin in chloroform was mixed in glass tube. The residual organic solvent was removed by rota-vaporation and further drying under high vacuum overnight. The lipid film was then hydrated with HEPES buffer (5 mM, pH 7.4) containing 150 mM NaCl. The tube was filled with argon, sealed with parafilm and then put into a 75 °C water bath for at least 30 min. Mild sonication and vortexing were applied to facilitate hydration to obtain a micelle or SLN formulation of miriplatin.

2.2.2.2 Preparation of miriplatin-loaded formulations by chloroform dripping. A solution of various lipids and miriplatin in chloroform was prepared in a larger scale (at least 5 times: 20 μmol total lipids and 4 μmol miriplatin) in glass tube. The hydration buffer, HEPES buffer (5 mM, pH 7.4) containing 150 mM NaCl, was preheated and equilibrated in a 75 °C water bath on a stirring hot plate (Fisher Scientific). The chloroform solution was pre-warmed and added dropwise into the above-mentioned aqueous phase of HEPES buffer. The two phases were kept stirring at 75 °C for 30 min until all chloroform was evaporated. Further mild sonication and vortexing were applied to facilitate hydration and homogeneity to obtain a micellar or SLN formulation of miriplatin.

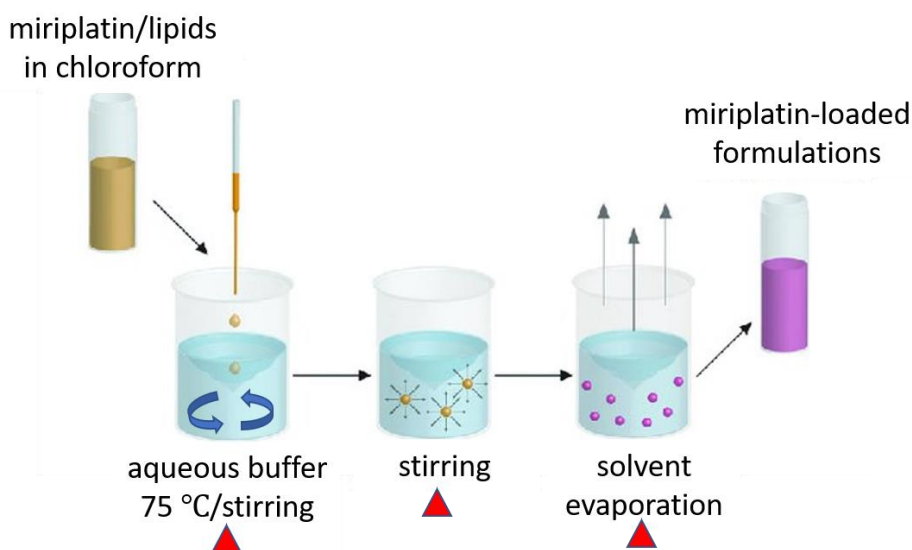


Figure 2.3. Schematic illustration of the chloroform dripping method.

2.2.2.3 Preparation of miriplatin-loaded formulations by chloroform injection. A

solution of various lipids and miriplatin in chloroform was prepared in a larger scale as described above. The hydration buffer, HEPES buffer (5 mM, pH 7.4) containing 150 mM NaCl, was preheated and equilibrated in a 75 °C water bath on a stirring hot plate. The chloroform solution of miriplatin and lipids was pre-warmed and injected into aqueous phase slowly. The mixture was kept stirring at 75 °C for 30 min until all chloroform was evaporated. The resultant aqueous colloidal solution was sonicated and vortexed mildly to enhance hydration and sample homogeneity to obtain a micellar or SLN formulation of miriplatin.

2.2.2.4 Preparation of miriplatin-loaded formulations by chloroform evaporation. A

solution of various lipids and miriplatin in chloroform was prepared in a larger scale as described above. The aqueous phase, HEPES buffer (5 mM, pH 7.4) containing 150 mM NaCl, was put into a water bath on a stirring hot plate at room temperature. The chloroform solution as the organic phase (2 to 3 mL) was added into the aqueous phase under constant mixing by a stirring

bar. The temperature of the mixture was increased from room temperature to 75 °C and then kept at 75 °C for 30 min until all chloroform was evaporated. Further mild sonication and vortexing were applied to facilitate hydration and the dispersion to yield the miriplatin-loaded micellar or SLN formulation.

2.2.2.5 Preparation of miriplatin-loaded formulations by co-solvent evaporation. A solution of various lipids and miriplatin was dissolved in a co-solvent (chloroform/iso-propanol mixed in different ratio) in a larger scale as described above. The hydration buffer, (5 mM HEPES, 150 mM NaCl, pH 7.4) was put into a flask in water bath on a stirring hot plate at room temperature. The co-solvent solution of lipids and miriplatin (2 to 3 mL in total) was added into the hydration buffer under constant mixing. The temperature was then increased from room temperature to 85 °C. The mixture was kept stirring at 85 °C for an additional 30 min until all organic solvents were evaporated. Further mild sonication and vortexing were applied to the resultant aqueous suspension to facilitate hydration and dispersion in order to obtain a miriplatin-loaded micellar or SLN formulation.

2.2.2.6 Preparation of miriplatin-loaded formulations by slow chloroform evaporation. A solution of various lipids and miriplatin in chloroform was prepared in a larger scale as described above. The hydration buffer (5 mM HEPES buffer, 150 mM NaCl, pH 7.4) was put into a flask in water bath on a stirring hot plate at room temperature. The chloroform solution (2 to 3 mL) was added into the hydration phase and mixed well by constant stirring. The temperature of the mixture was then slowly increased from room temperature to 75 °C (approximately ten centigrade every 30 min from room temperature until 60 °C, and then five centigrade every 30 min until 75 °C). The mixture was stirred at 75 °C for another 30 min until

all chloroform was evaporated. Further mild sonication and vortexing were applied to facilitate hydration and dispersion to obtain a miriplatin-loaded micellar or SLN formulation.

2.2.2.7 Preparation of miriplatin-loaded formulations by co-solvent slow

evaporation. A solution of various lipids and miriplatin in co-solvent (chloroform/iso-propanol mixed in different ratios) was prepared as described above. The hydration buffer (5 mM HEPES, 150 mM NaCl, pH 7.4) was put into a flask in water bath on a stirring hot plate at room temperature. The co-solvent solution (2 to 3 mL in total) was added into the hydration buffer and mixed well by constant stirring. The temperature was slowly increased from room temperature to 85 °C (approximately ten centigrade every 30 min from room temperature until 60 °C, and then five centigrade every 30 min until 85 °C). The mixture was stirred at 85 °C for another 30 min until all organic solvents were evaporated. Further mild sonication and vortexing were applied to facilitate hydration and dispersion to obtain a miriplatin-loaded micellar or SLN formulation.

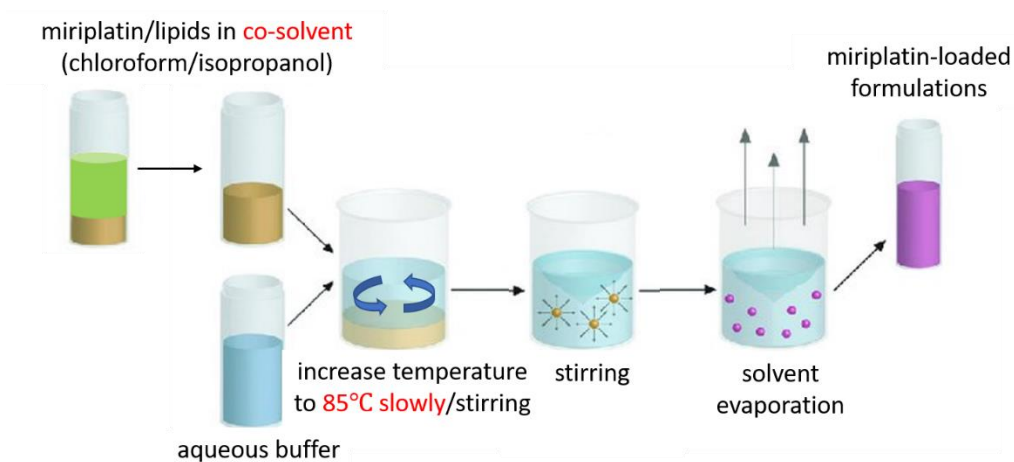


Figure 2.4. Schematic of co-solvent slow evaporation method.

2.2.2.8 Preparation of selected miriplatin-loaded lipid nano formulations by co-solvent slow evaporation. Selected miriplatin-loaded formulations, whose compositions are shown in Table 2.1., were prepared by co-solvent slow evaporation method as described in 2.2.2.7.

Table 2.1
Composition of Selected Miriplatin-Loaded Lipid Nano Formulations

Nanocarriers	Lipid composition	Drug input (%)
micelles	100% PE-PEG ₂₀₀₀	20% miriplatin
	100% PE-PEG ₂₀₀₀	20% miriplatin+10% PTX
SLNs	90% TM/10% PE-PEG ₂₀₀₀	20% miriplatin
	90% TP/10% PE-PEG ₂₀₀₀	20% miriplatin
	90% TM/10% PE-PEG ₂₀₀₀	20% miriplatin+10% PTX
	90% TP/10% PE-PEG ₂₀₀₀	20% miriplatin+10% PTX
	80% TM/10% Chol/10% PE-PEG ₂₀₀₀	20% miriplatin
	80% TP/10% Chol/10% PE-PEG ₂₀₀₀	20% miriplatin

(TM: trimyristin, TP: tripalmitin, PE-PEG₂₀₀₀: 1,2-distearoyl-sn-glycero-3-phosphoethanolamine-N-[methoxy (polyethylene glycol)-2000] (ammonium salt), Chol: cholesterol, PTX: paclitaxel)

2.2.3 Physicochemical Characterizations of Miriplatin-Loaded Nano Formulations

The sizes and Polydispersity Index (PDI) of the miriplatin-loaded formulations were measured by dynamic light scattering using Zetasizer ZS 90 (Malvern Instruments Ltd., Malvern, UK). An aliquot (3 μ L) of miriplatin-loaded formulations diluted with deionized water (150 μ L) was transferred into a low volume cuvette (ZEN0118, Malvern Instruments) and the

hydrodynamic diameter was measured in triplicates. The size distribution based on intensity, volume and number was analyzed by Zetasizer software.

2.3 Results and Discussion

Miriplatin-loaded formulations consisting of miriplatin, solid lipids (trimyristin or tripalmitin) and 18:0 PE-PEG₂₀₀₀ were successfully prepared by different procedures and characterized by dynamic light scattering to measure their size and PDI. Miriplatin was compatible with solids lipids and pegylated lipid to form lipid-based formulations due to their similar structures.

2.3.1 Size Distribution of Miriplatin-Loaded Formulations Based on Intensity, Volume and Number Weighing from the Malvern Zetasizer Software

Dynamic Light Scattering (DLS) is a well-established technique to measure the size of nanoparticles [101]. DLS monitors the change of intensity of scattered light from nanoparticles in suspension as they move in and out of the orifice of the detector due to Brownian motion. The recorded data are then converted into size and a size distribution using the Stokes-Einstein relationship. The weighing of the size distribution can be presented based on the intensity of the light scattered by the nanoparticles, the volume of the nanoparticles, and the number of the nanoparticles. In this study, the size and the size-distribution are reported based on the number of the nanoparticles, although intensity-based distribution is also commonly used for nanoparticles. Intensity-based distributions weigh more on species that have the largest scattering intensity while number-based distributions stress more on species with the highest number of particles, which tend to be smaller particles. For this reason, investigations of small

nanoparticles (usually around or smaller than 100 nm in diameter) more commonly use number-based distribution to present the DLS data rather than intensity-based distribution [82, 98].

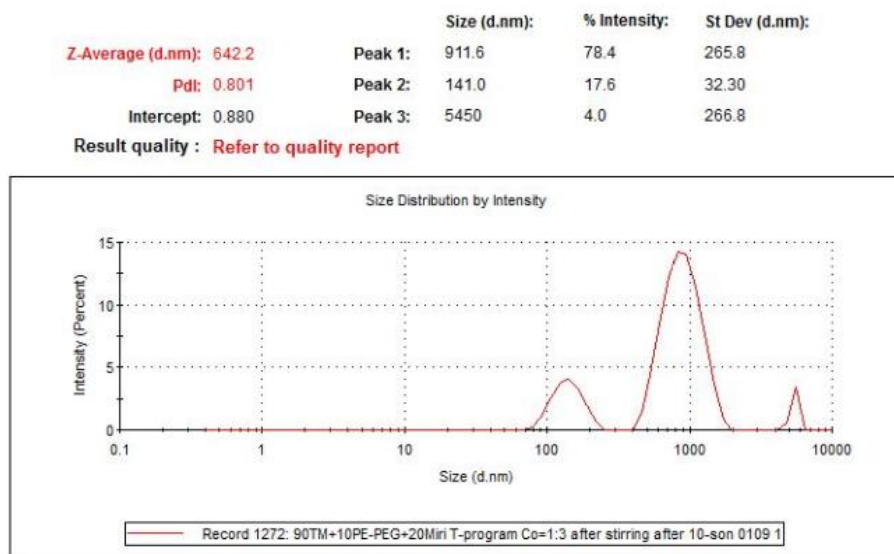


Figure 2.5. An example of intensity-based size distribution of miriplatin-loaded SLN from Malvern Zetasizer software.

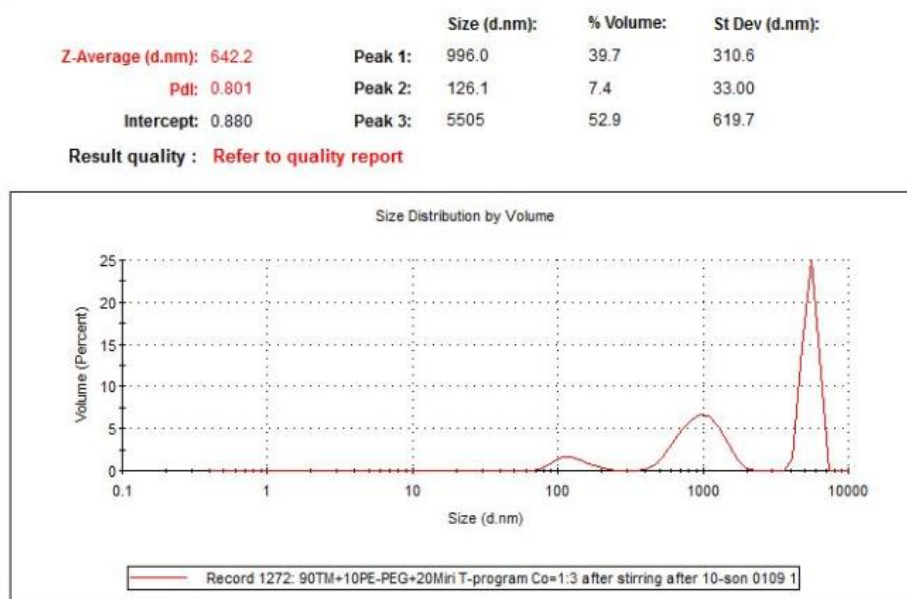


Figure 2.6. An example of volume-based size distribution of miriplatin-loaded SLN from Malvern Zetasizer software.

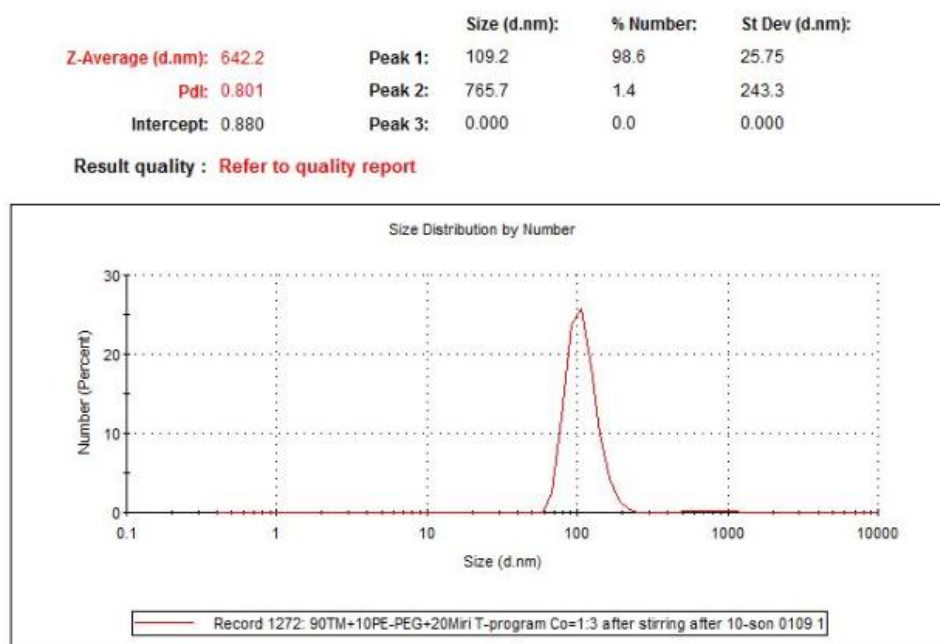


Figure 2.7. An example of number-based size distribution of miriplatin-loaded SLN from Malvern Zetasizer software.

As shown in Fig 2.5-2.7, nano formulations with multiple peaks in size distribution and a large PDI (e.g., miriplatin-loaded SLNs), was poorly represented by the intensity-based calculation of size distribution. However, the number-based size distribution could represent the size of the majority of the nanoparticles, which also could be reflected by TEM images in Chapter 3. By contrast, as shown in Picture 2.8-2.10, miriplatin-loaded micelles of good homogeneity had similar size results whether the data is presented based on intensity or size. Hence, all the sizes of miriplatin-loaded nano formulations in this study are represented in number-based distribution.

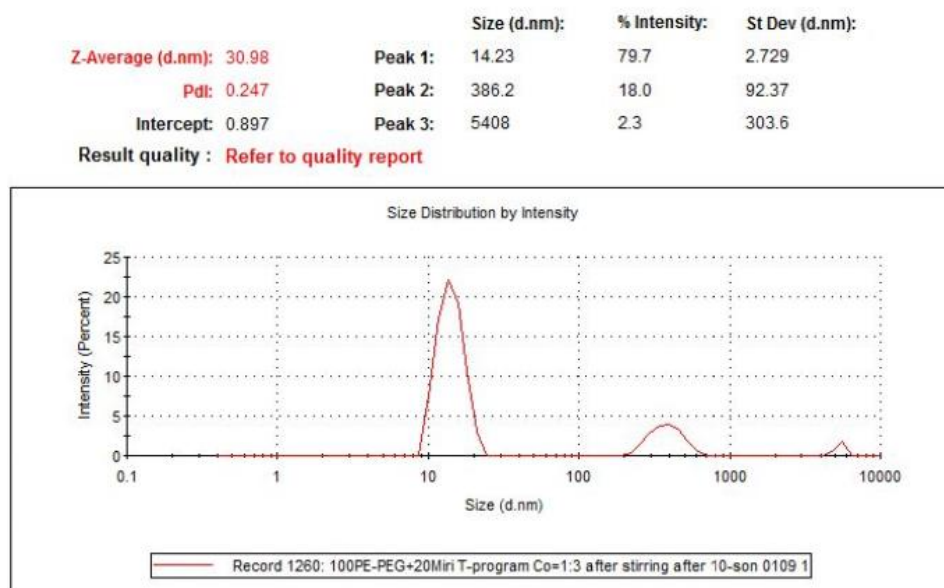


Figure 2.8. An example of intensity-based size distribution of miriplatin-loaded micelle from Malvern Zetasizer software.

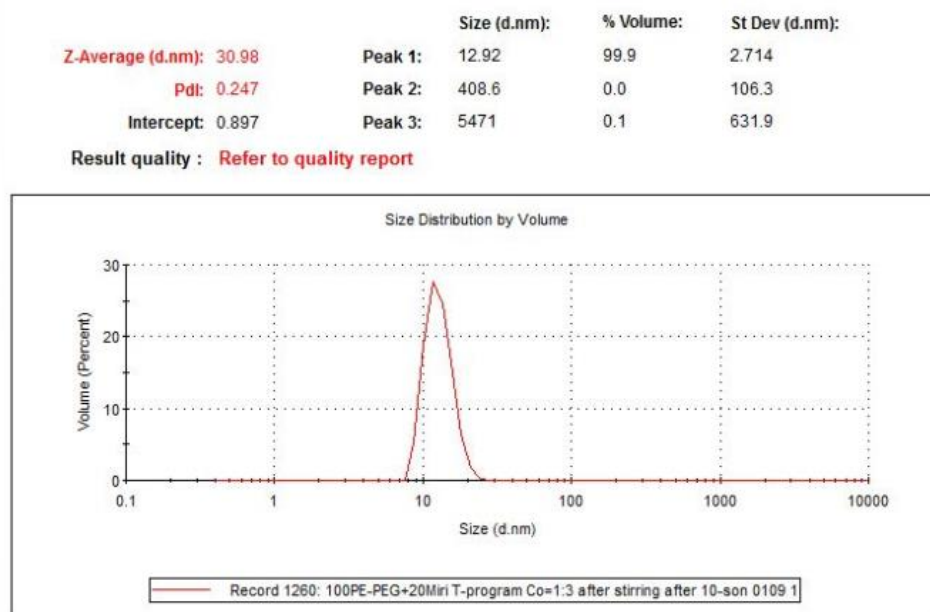


Figure 2.9. An example of volume-based size distribution of miriplatin-loaded micelle from Malvern Zetasizer software.

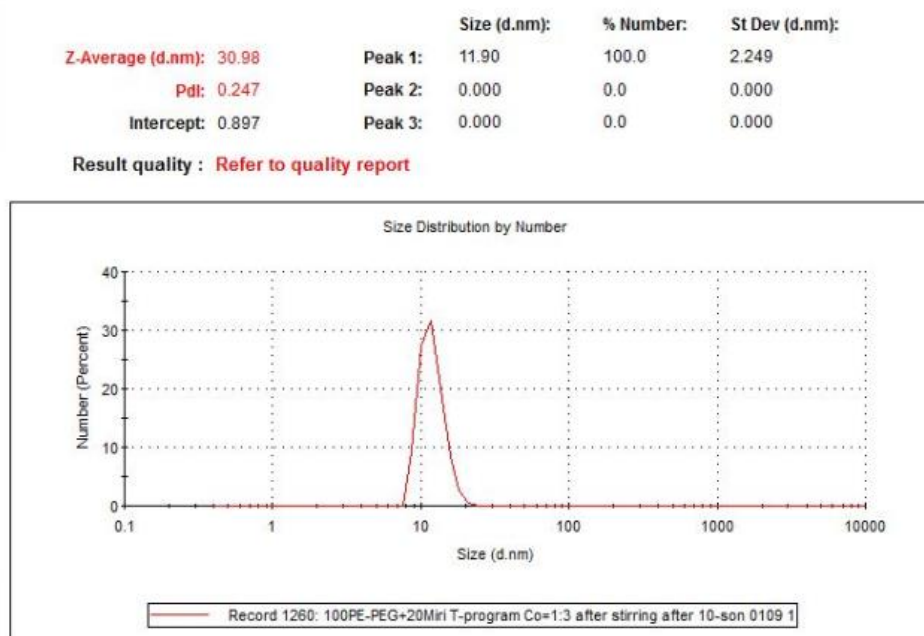


Figure 2.10. An example of number-based size distribution of miriplatin-loaded micelle from Malvern Zetasizer software.

2.3.2 Effect of the Payload Drug Miriplatin to the Nano Formulations

SLNs with or without the payload miriplatin were prepared by chloroform dripping and their sizes and PDI values are listed in Table 2.2. As shown in Table 2.2, the size and PDI of the SLN formulations with miriplatin were smaller than those without miriplatin. The PDI values of SLN formulations with or without miriplatin were all below 0.3, which indicates good homogeneity.

Because of its unique chemical structure with two C14 hydrocarbon chains, miriplatin can be considered as both the anticancer payload drug and a lipid component inside the formulations. Therefore, appropriate amount of miriplatin would be well compacted with other lipids (TM, TP and PE-PEG₂₀₀₀) to form denser colloids of smaller size and PDI.

Table 2.2
Composition, Size and PDI of SLNs with or without Miriplatin

SLNs Compositions	Drug input (%)	Size (number, nm)	PDI
95% TM/5% PE-PEG ₂₀₀₀	/	148.1	0.303
95% TP/5% PE-PEG ₂₀₀₀	/	148.5	0.202
95% TM/5% PE-PEG ₂₀₀₀	20% miriplatin	121.2	0.254
95% TP/5% PE-PEG ₂₀₀₀	20% miriplatin	107.4	0.186

(TM: trimyristin, TP: tripalmitin, PE-PEG₂₀₀₀: 1,2-distearoyl-sn-glycero-3-phosphoethanolamine-N- [methoxy (polyethylene glycol)-2000] (ammonium salt))

2.3.3 Effect of Lipid Components

The effect of lipid components (TM, TP and pegylated lipid) on the size and PDI of their miriplatin nano formulations is evaluated using selected lipid compositions. The SLN and micelle formulations of different compositions were prepared by chloroform dripping and their size and PDI measured by dynamic light scattering (Table 2.3 and Table 2.4). The sizes of the SLN formulations ranged from 30 nm to 120 nm and most of their PDI were around or below 0.3. For the same ratio of triglyceride lipid/PE-PEG₂₀₀₀, most sizes of SLNs consisting of the triglyceride lipid TP were slightly smaller than the SLNs consisting of the other triglyceride lipid TM. Additionally, in SLNs of the same triglyceride lipid (TM or TP) the higher the mole percentage of PE-PEG₂₀₀₀ the lower the size would be. Micelles, which could also be considered as 100% PE-PEG₂₀₀₀ + 0% solid lipids, can be fit into this trend as well, so the size of miriplatin-loaded formulations could change from 10 nm to 120 nm as the percentage of PE-PEG₂₀₀₀ changes from 100% to 5%.

Table 2.3
Size and PDI of Miriplatin-Loaded Formulations (SLNs and Micelles) with Different Lipid Compositions

SLNs Compositions	Drug input (%)	Size (number, nm)	PDI
95% TM/5% PE-PEG ₂₀₀₀	20% miriplatin	126.6	0.237
95% TP/5% PE-PEG ₂₀₀₀	20% miriplatin	104.1	0.382
90% TM/10% PE-PEG ₂₀₀₀	20% miriplatin	81.81	0.255
90% TP/10% PE-PEG ₂₀₀₀	20% miriplatin	47.72	0.460
85% TM/15% PE-PEG ₂₀₀₀	20% miriplatin	63.05	0.491
85% TP/15% PE-PEG ₂₀₀₀	20% miriplatin	105.6	0.490
80% TM/20% PE-PEG ₂₀₀₀	20% miriplatin	38.36	0.263
80% TP/20% PE-PEG ₂₀₀₀	20% miriplatin	23.59	0.587
100% PE-PEG ₂₀₀₀	20% miriplatin	12.52	0.391

(TM: trimyristin, TP: tripalmitin, PE-PEG₂₀₀₀: 1,2-distearoyl-sn-glycero-3-phosphoethanolamine-N- [methoxy (polyethylene glycol)-2000] (ammonium salt))

It is well acknowledged that the size of nano drug delivery systems has a significant impact on their tissue distribution and stability in blood circulation [102]. It is reported that nanocarriers with a size lower than 150 nm in diameter can escape from the fenestrated capillaries of solid tumors to penetrate into the tumor interstitium (aka enhanced permeation and retention effect, EPR effect) and 200 nm is the cut off size to cause such EPR effect for passive targeting[65, 103]. Moreover, the openings of blood vessels in normal tissues are less than 10 nm so nano drug delivery systems larger than 10 nm would get across the openings of the tumor blood vessels easily but not those of normal blood vessels to cause adverse effect [91]. The sizes of FDA approved nano formulations, such as Doxil® (pegylated liposomal doxorubicin) and Abraxane® (albumin-bound paclitaxel), are all in the range of 50-150 nm [91, 104, 105]. Therefore, our miriplatin-loaded formulations ranging 30-120 nm in diameter may serve as valid

nanocarriers of anticancer drugs. The SLNs (90% TM/TP + 10% PE- PEG₂₀₀₀ + 20% Miripatin) with a diameter around 50-80 nm and micelles (100% PE-PEG₂₀₀₀ + 20% Miripatin) with a diameter around 10 nm are chosen for further studies.

2.3.4 Comparison of Different Methods to Prepare Nano Formulations

Miriplatin-loaded SLNs consisting of the same lipid composition (90% TM/TP + 10% PE- PEG₂₀₀₀ + 20% miripatin) were successfully prepared by different procedures and characterized. Their composition, size and PDI were compared in Table 2.5.

2.3.4.1 Thin film hydration method vs. scale-up preparation methods. Compared to other SLNs prepared by scale-up methods, SLNs prepared by thin film hydration method had similar sizes but much better PDI values indicating better homogeneity of nano formulation, which was caused by the good quality of the thin film and the well-established methodology by previous lab mates. However, one critical step of thin film hydration, which is organic solvents evaporation by rota-vaporator needed to be practiced several times in order to form a uniform thin film and the resultant SLNs may still have batch-to-batch variance. The scale of thin film hydration could be no more than several hundred microliters while other preparation methods could achieve at least one-milliliter scale. Therefore, thin film hydration method would be suitable for small scale experiments to try different compositions for the sake of saving cost, while scale-up methods would be more practical for further industrial production.

Table 2.4
*Size and PDI of Miriplatin-Loaded SLNs (90% TM/TP + 10% PE-PEG₂₀₀₀ + 20% Miriplatin)
 Prepared by Different Preparation Procedures*

SLN compositions + drug input (%)	Preparation methods	Size (number, nm)	PDI
90% TM /10% PEG +20% Miri	Thin film hydration	86.68	0.261
90% TP/10% PEG +20% Miri	Thin film hydration	91.45	0.241
90% TM /10% PEG +20% Miri	Chloroform dripping	59.83	0.252
90% TP/10% PEG +20% Miri	Chloroform dripping	49.92	0.397
90% TM /10% PEG +20% Miri	Chloroform injection	100.1	0.363
90% TP/10% PEG +20% Miri	Chloroform injection	98.10	0.613
90% TM /10% PEG +20% Miri	Chloroform evaporation	82.62	0.634
90% TP/10% PEG +20% Miri	Chloroform evaporation	277.0	0.623
90% TM /10% PEG +20% Miri	Co-solvent evaporation	466.7	0.552
90% TP/10% PEG +20% Miri	Co-solvent evaporation	381.7	0.385
90% TM /10% PEG +20% Miri	Chloroform slow evaporation	70.15	1.000
90% TP/10% PEG +20% Miri	Chloroform slow evaporation	85.74	0.582
90% TM /10% PEG +20% Miri	Co-solvent slow evaporation	95.92	0.800
90% TP/10% PEG +20% Miri	Co-solvent slow evaporation	132.5	0.394

(TM: trimyristin, TP: tripalmitin, Miri: miriplatin, PEG: 1,2-distearoyl-sn-glycero-3-phosphoethanolamine-N-[methoxy(polyethylene glycol)-2000] (ammonium salt))

2.3.4.2 Solvent evaporation methods. Compared to chloroform dripping method, solvent evaporation methods yielded slightly larger formulations around 100 nm. This might be caused by higher encapsulation efficiency of miriplatin inside formulations (90% TP/10% PEG +20% miriplatin), which will be discussed in detail in the next chapter.

The sizes of SLN formulations prepared by the co-solvent evaporation method were much larger than SLNs prepared by other solvent evaporation methods. Because chloroform is immiscible with water and miriplatin is insoluble in water, the transition of miriplatin between the organic phase and the aqueous phase may be too low for efficient drug loading. Therefore, a co-solvent, was added to improve the miscibility of the organic phase and the aqueous phase. As shown in Table 2.6, although a number of solvents are miscible with both chloroform and water, isopropanol (IPA) was attempted as the co-solvent because it had better solubility of miriplatin than other co-solvents. The size of SLNs could be controlled by changing the percentage of IPA and the speed of the solvent evaporation. From the observed precipitation during or after the preparation procedures, slow evaporation did help lipids and miriplatin precipitate out of organic solvents gradually and slowly and them formed nanoparticles in aqueous phase, which also could be reflected by the drug recovery of nano formulations in Chapter 3. The boiling point of IPA is 83 °C so the final temperature of preparation was kept at 85 °C to drive its evaporation to completion. The long duration and high temperature of the preparation procedure may cause the degradation of miriplatin in aqueous buffer, which could be addressed in future studies by evaporating the organic solvents under reduced pressure.

The PDI values of SLNs prepared by co-solvent evaporation were much higher than 0.3, which might be caused by lower solubility of miriplatin in water and precipitation from the system. For future studies, the SLNs can be filtered to remove large particles and thus to further improve their homogeneity.

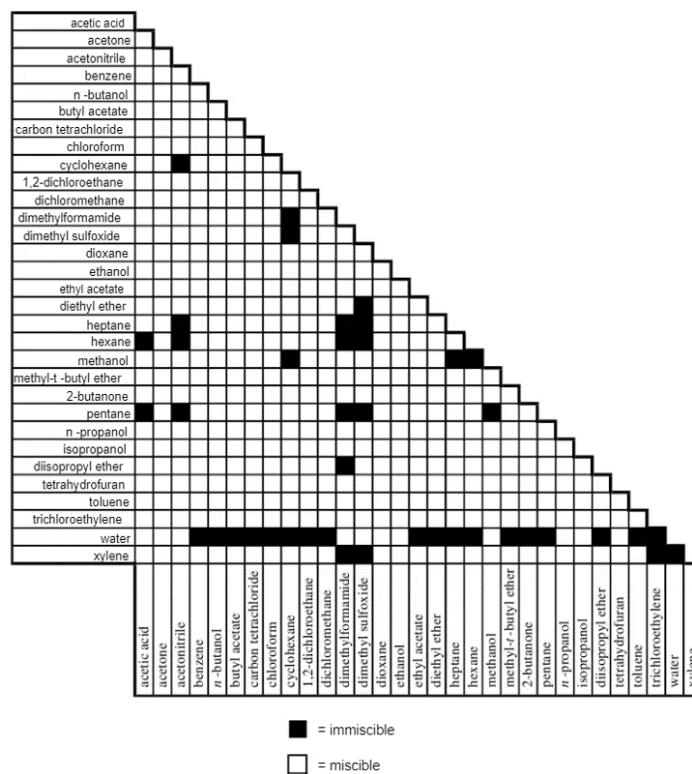


Figure 2.11. Solvent miscibility table [106].

Table 2.5
Solubility of Miriplatin/Solid Lipids (TM/TP) in Co-Solvents

Chloroform percentage (%)	Secondary organic solvent			
	percentage (%)	Ethanol	Acetone	Isopropanol
100	0	√	√	√
75	25	√	√	√
50	50	√	×	√
25	75	×	×	√
0	100	×	×	×

2.3.5 Size and Polydispersity Index (PDI) of Miriplatin-Loaded Formulations Prepared by Co-Solvent Slow Evaporation

Miriplatin-loaded SLNs and Micelles of selected compositions were successfully prepared by co-solvent slow evaporation. Such formulations' composition, size and PDI are shown in Table 2.7 and Table 2.8.

Table 2.6
Composition, Size and PDI of Selected SLN Formulations Prepared by Co-Solvent Slow Evaporation Method

SLNs Compositions	Drug input (%)	Size (number, nm)	PDI
90% TM/10% PE-PEG	20% miriplatin	109.2	0.801
90% TP/10% PE-PEG	20% miriplatin	143.6	0.948
90% TM/10% PE-PEG	20% miriplatin + 10% PTX	138.1	0.872
90% TP/10% PE-PEG	20% miriplatin + 10% PTX	82.08	1.000
80% TM/10% Chol/10% PE-PEG	20% miriplatin	142.1	0.667
80% TP/10% Chol /10% PE-PEG	20% miriplatin	83.32	0.911

(TM: trimyristin, TP: tripalmitin, PE-PEG₂₀₀₀: 1,2-distearoyl-sn-glycero-3-phosphoethanolamine-N- [methoxy (polyethylene glycol)-2000] (ammonium salt), Chol: cholesterol, PTX: paclitaxel)

Table 2.7
Composition, Size and PDI of Selected Micelle Formulations Prepared by Co-Solvent Slow Evaporation Method

Micelles Compositions	Drug input (%)	Size (number, nm)	PDI
100% PE-PEG ₂₀₀₀	20% miriplatin	11.90	0.247
100% PE-PEG ₂₀₀₀	20% miriplatin + 10% PTX	11.71	0.254

(TM: trimyristin, TP: tripalmitin, PE-PEG₂₀₀₀: 1,2-distearoyl-sn-glycero-3-phosphoethanolamine-N- [methoxy (polyethylene glycol)-2000] (ammonium salt), PTX: paclitaxel)

2.3.5.1 Comparison of different nanocarriers. In Table 2.7, there was not too much difference in size and PDI between miriplatin-loaded SLNs of different compositions. The sizes were all in the range of 80-150 nm and the PDI were all around 0.8, indicating poor homogeneity. The slight difference in size might be caused by the poor controlling of the temperature increasement. As discussed earlier, the speed of solvent evaporation would influence the speed of lipid/miriplatin precipitation and nanoparticle formation. The manual increase of temperature might not be controlled as precisely as instrument, so this problem could be solved by computer programming to achieve precise thermal control.

Compared to SLNs, the variance in the size and PDI of miriplatin-loaded micelles were negligible. The micelles had much smaller size around 10 nm and PDI lower than 0.3, suggesting that the micelle delivery system with PE-PEG₂₀₀₀ as the major lipid component was compatible with miriplatin. The C18 long chains of PE-PEG₂₀₀₀ further suggest that triglycerides with longer chains such as tristearin might also be a compatible lipid component of the SLN formulations of miriplatin. The small size of the micelles might enhance their penetration into solid tumors but might also generate stability and pharmacokinetics problems *in vivo*.

Miriplatin-loaded liposome formulations consisting of phospholipid, cholesterol and pegylated lipid were prepared, too. However, such formulations showed inferior physicochemical and biological properties in our preliminary studies and hence were not subjected to further studies.

2.3.5.2 Effect of cholesterol. It was reported that cholesterol can affect the fluidity of bilayer structure and occupy the cavities between fatty acid chains to inhibit the movement of hydrocarbon chains [107]. Therefore, cholesterol is widely used as a stabilizer in lipid-based

formulations [108]. However, in our studies, adding cholesterol did not improve or worsen the homogeneity or stability of miriplatin-loaded SLNs (Table 2.7). This is probably because the core of the SLNs under our study is already filled with hydrocarbon chains of either the lipids or miriplatin so that cholesterol might not be able to permeate and stabilize the SLNs as usual. However, cholesteryl palmitate and cholesteryl myristate may be alternatives of cholesterol to further stabilize miriplatin formulations.

2.4 Summary

Miriplatin-loaded formulations were successfully prepared by different preparation methods, including thin film hydration method and several scale-up methods (chloroform dripping, chloroform injection, chloroform evaporation, co-solvent evaporation, chloroform slow evaporation and co-solvent slow evaporation). In the future, this method could be further optimized to reduce batch-to-batch variance and to improve homogeneity. Different compositions of the nano formulations have been investigated. Higher percentage of the pegylated lipid PE-PEG₂₀₀₀ in the composition can result in a smaller size. Among the two types of nano formulations under this study, micelles were much smaller (~ 10 nm in diameter) and more homogeneous (PDI < 0.3), while SLNs were bigger (~ 100 nm in diameter) and had a more heterogeneous size distribution that would need improvement (PDI ~0.8).

CHAPTER 3: PHYSICO-CHEMICAL CHARACTERIZATION OF MIRIPLATIN-LOADED NANO FORMULATIONS

3.1 Introduction

3.1.1 Solubility of Miriplatin

Miriplatin was approved in Japan for the treatment of hepatocellular carcinoma (HCC) in 2009. It can be easily suspended in ethyl esters of iodized fatty acids obtained from poppy seed oil and keeps its dispersed state for a long duration [44]. In clinic, it is administered into the hepatic artery as a suspension in an oily lymphographic agent (Lipiodol Ultra-Fluide®) to gradually release the active platinum compounds [44, 96]. The miriplatin/Lipiodol suspension is exclusively used for HCC in Japan and is the only formulation of miriplatin in clinical use. The narrow application and the limited pharmaceutical development are mainly due to its extremely low solubility in water (<0.00260 mg/mL) [109]. Among organic solvents commonly used in research labs (such as methanol, ethanol, acetonitrile and acetone), miriplatin can be only well dissolved in chloroform above 1 mg/mL.

3.1.2 Quantification of Miriplatin

Inductively coupled plasma mass spectrometry (ICP-MS) uses inductively coupled plasma to atomize the sample and produce excited atoms and ions, which are then detected by their emitted electromagnetic radiation at wavelengths characteristic of a particular element. The plasma is applied by a high temperature source of ionized source gas (often argon). In this way, ICP-MS can specifically trace an element of interest regardless of its form, which makes it a highly attractive method to detect trace level of elements in biological fluids [110]. Heavy

metals, such as platinum, gold and palladium can all be quantified by ICP-MS, even those in water-insoluble molecules. The last decade sees a slow shift towards ICP-MS from other older techniques of detection such as atomic emission and atomic absorption [110]. ICP-MS offers plenty of attractive features including high sensitivity, wide elemental coverage, multi-element capability, and simple sample preparation [110].

Additionally, inductively coupled plasma optical emission spectrometry (ICP-OES), is an alternative analytical technique used for the detection of chemical elements. Compared to ICP-MS, ICP-OES enjoys simpler method development and lower cost but has higher limit of detection. Both ICP-MS and ICP-OES have been widely applied in the analysis of metal elements in pharmaceutical formulations [111, 112].

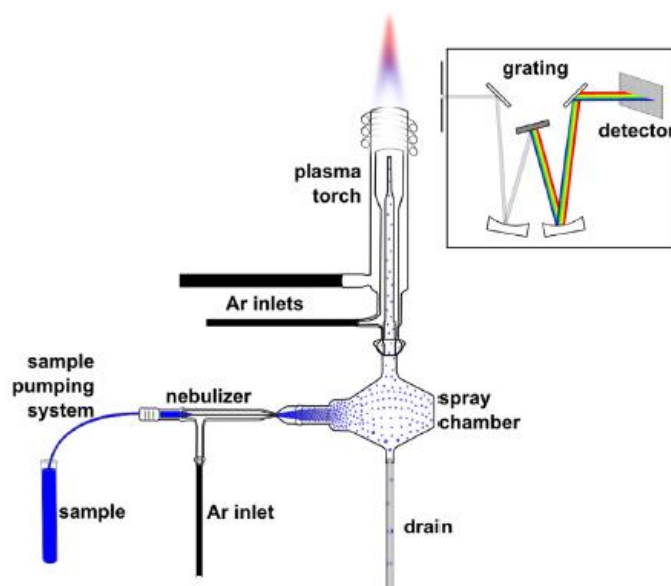


Figure 3.1. Diagram of a typical ICP-OES instrument with radial configuration of the detection system [113].

In this study, a method to quantify miriplatin was established by ICP-OES. In order to quantify the platinum drugs inside miriplatin-loaded nano formulations at high recovery, which is the percentage of the detected platinum by the total input platinum, several agents (nitric acid, sulfuric acid and aqua regia) were used to digest nano formulations before injection into ICP-OES. Moreover, Xia's group have published a quantification method for miriplatin and miriplatin-loaded liposomes by high performance liquid chromatography (HPLC) [109]. Thus, another HPLC method of quantifying miriplatin in the nano formulations under this study was attempted.

3.1.3 Transmission Electron Microscopy (TEM)

In nanotechnology, TEM serves as an essential tool for characterizing the morphology and particle size of nano drug carriers [114]. The principle of transmission electron microscopy (TEM) is to image a sample by detecting electrons after they transmit through the sample [115]. An ultrathin section of the specimen was formed on a grid followed by applying an accelerated beam of electrons and generating an image with the transmitted electrons. Metals would scatter electrons to appear darker against the background. By contrast, non-metals that cannot scatter electrons need additional staining techniques to visualize [115]. Positive staining is used to visualize samples' inner components (such as organelles inside cells) while negative staining can help to visualize the structure and size [116].

In this study, the miriplatin-loaded nano formulations were negatively stained with uranyl acetate, then observed and imaged under TEM. The morphology of nanocarriers with different compositions was compared and the sizes were compared with size data generated from dynamic light scattering.

3.2 Materials and Methods

3.2.1 Materials

Miriplatin was purchased from MedChemExpress LLC (NJ, USA). Two-hundred mesh continuous carbon-coated copper grids were obtained from TED PELLA (Redding, CA). All other organic solvent and chemicals were purchased from Sigma Aldrich, Fisher Scientific or VWR.

3.2.2 Quantification of Miriplatin by HPLC

Quantification of miriplatin was performed with high performance liquid chromatography (HPLC) equipped with Waters 2695 separations module coupled to 2996 photodiode array detector. The stationary phase (Agilent ZORBAX SB-C8, 3.5 μm ; 4.6 \times 150 mm) was kept at 30 $^{\circ}\text{C}$, and the mobile phase (methanol: water: acetonitrile = 92:7.5:0.5, v/v) was run at the flow rate of 1 mL/min. Effluent was monitored at wavelength 210 and 220 nm. In order to enhance the dissolution of miriplatin in methanol, gentle heating and sonication were applied to achieve a maximum concentration of 500 $\mu\text{g}/\text{mL}$. The calibration curve of miriplatin was established using standard solutions of miriplatin (10, 20, 50, 100, 200, 250, 500 $\mu\text{g}/\text{ml}$) that were diluted from a stock solution at 500 $\mu\text{g}/\text{ml}$. An aliquot (10 μL) of each standard solution was injected into HPLC 0, 4, 8, 12, 24 hours after preparation.

3.2.3 Mass Spectrometer

MS spectra were recorded using a Varian 320 ESI-MS spectrometer at the Chemistry Department. The mass spectrometer was used for quality control (QC) samples containing miriplatin and operated in positive ion mode. The drying gas temperature was 160 $^{\circ}\text{C}$ and the capillary voltage was 5000 V. Miriplatin was dissolved in methanol (5-50 $\mu\text{g}/\text{mL}$) before

injection into the MS spectrometer. Analysis of the QC samples was performed 3 times after the blank runs.

3.2.4 Quantification of Miriplatin by ICP-OES

Quantification of miriplatin by inductively coupled plasma-optical emission spectrometry (ICP-OES) was performed at the Chemistry Department. The serial platinum standard solutions for the calibration curve (5, 10, 50, 100, 1000, 10 000 ng/mL) were prepared by dilution from a 1 g/mL platinum standard solution (Inorganic Ventures, VA, USA) and were measured on a Thermal Fisher iCAP 6000 series instrument at wavelengths 214.4 and 265.9 nm . The calibration curves of cisplatin and miriplatin were established with the same serial platinum standard solutions in 5% nitric acid. Each sample was measured in triplicates.

3.2.5 Quantification of Recovery of Platinum in Miriplatin-Loaded Nano Formulations by ICP-OES

In order to determine the recovery of platinum quantification for miriplatin-loaded nano formulations, different agents were used to digest nano formulations, including nitric acid, sulfuric acid and aqua regia. Heating with nitric acid for 90 min was chosen as the general digestion method to release platinum from the nano formulations into aqueous phase for quantification. Specifically, an aliquot (50 μ L) of formulations was taken and diluted into 3.45 mL 70% concentrated nitric acid followed by heating at 90 $^{\circ}$ C for at least 90 min. After cooling down, an aliquot (500 μ L) of the digestion solution was diluted into 6.5 mL deionized water to achieve the lower concentration of nitric acid (5%) that is suitable for the injection into ICP-OES. Each sample was measured in triplicates. The concentration of platinum in the miriplatin-loaded nano formulations was estimated by the calibration curve of platinum standard solutions

as mentioned in 3.2.4. The recovery of platinum from miriplatin-loaded nano formulations is calculated by the following formula:

Recovery (%)

$$= \frac{\textit{Platinum amount detected from ICP}}{\textit{Platinum amount in the added miriplatin during drug loading}} \times 100\%$$

3.2.6 Characterization of Miriplatin-Loaded Nano Formulations by TEM

The morphology of miriplatin-loaded nano formulations was studied on a JEOL-JEM 1230 Electron Microscope (JEOL, Japan). Two-hundred mesh carbon-coated copper TEM grids were exposed to glow discharge to increase hydrophilicity before usage. An aliquot (5 μ L) of nano formulation was deposited on a grid and air-dried for at least 60 seconds. Excess liquid on the grid was blotted with filter paper to generate a thin film, which was then quickly stained with 2% uranyl acetate and blotted with filter paper for cycles. The grid was then transferred into the transmission electron microscope for imaging with the help of Dr. Fei Guo from Electron Imaging Facility, Department of Molecular and Cellular Biology at UC Davis. The digital images of the nano formulations from TEM were recorded and analyzed with EMMENU4 (TIETZ imaging software).

3.3 Results and Discussion

3.3.1 Quantification of Miriplatin by HPLC

3.3.1.1 Calibration curve of miriplatin by HPLC. The elution peaks of miriplatin was monitored by ultraviolet spectrophotometer at wavelengths 210, 220, 254 and 280 nm, and the maximum wavelength of miriplatin was found at 210 nm. Figure 3.2 displayed the chromatogram of free miriplatin at a series of concentrations in methanol (10, 20, 50, 100, 200,

250, 500 $\mu\text{g/ml}$). Due to the limited solubility in methanol, miriplatin standards gave both increasing retention time (from 7.5 min to 8.5 min) and broader elution peaks as the concentration increases. Addition of acetonitrile to decrease the mobile phase polarity sharpened the elution peaks. However, because miriplatin has an even lower solubility in acetonitrile than methanol, acetonitrile could not be added at a higher percentage to improve the shape of the elution peaks.

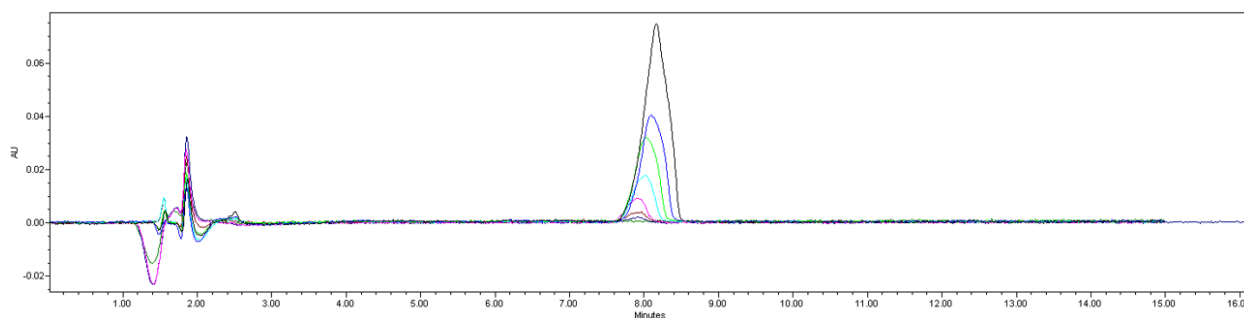


Figure 3.2. Chromatograms of free miriplatin (10, 20, 50, 100, 200, 250, 500 $\mu\text{g/ml}$) by HPLC.

The calibration curves of miriplatin at wavelength 210 nm and 220 nm (Figure 3.3) both showed an R square value above 0.999 in linear regression, indicating that the concentration of miriplatin had a linearly relationship with the area under the peak in HPLC chromatogram over the concentration range from 10 to 500 $\mu\text{g/mL}$.

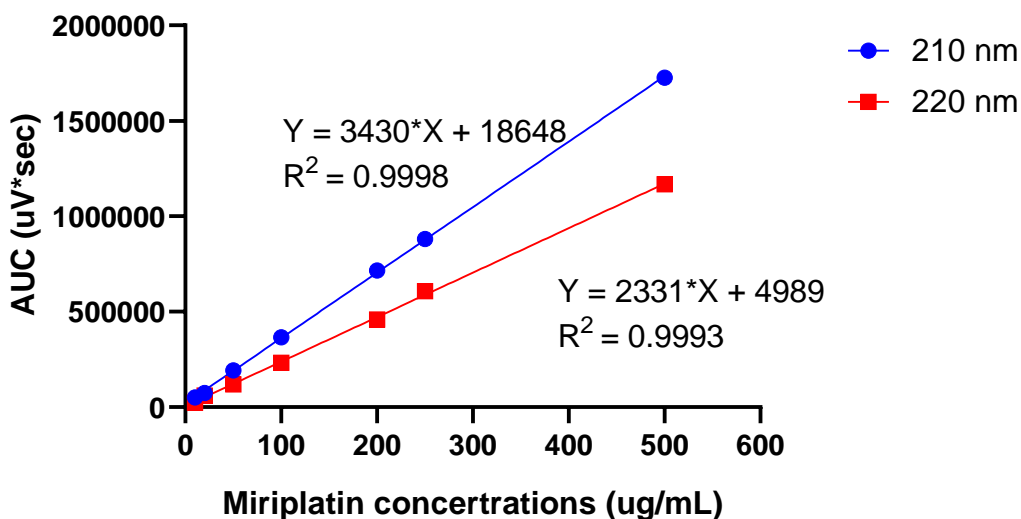


Figure 3.3. Calibration curve of miriplatin UV absorbance at wavelengths 210 and 220 nm in HPLC.

3.3.1.2 Calibration curve of miriplatin by HPLC (AUC decreased along with time).

As shown in Figure 3.4, AUC (area under curve) from HPLC chromatogram decreased by percentage as time went by, from the 0 h to 24 hours after the first injection. This might be caused by miriplatin's extremely low solubility in water (<0.00260 mg/mL) [109] and relatively low solubility in methanol. Although about 0.5 mg/mL miriplatin could be dissolved in methanol after mild sonication and heating, miriplatin might precipitate back out of the solution after some time of storage at room temperature.

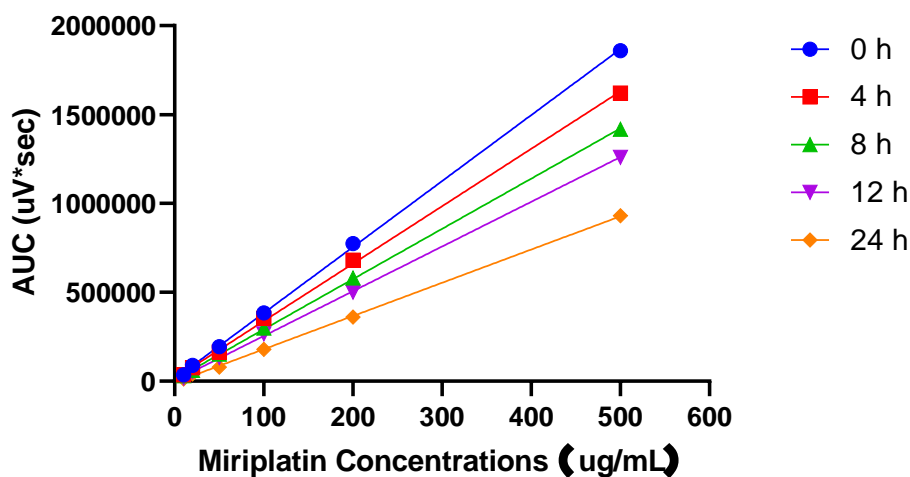


Figure 3.4. The change of AUC in calibration curve of miriplatin over time.

It is well documented that platinum-based drugs are not stable in aqueous media because the leaving groups of the platinum complex will be replaced by hydroxy groups [19, 42]. The miriplatin molecules may not be stable in methanol as well in that the two myristate leaving groups of miriplatin could be replaced gradually by molecules in the mobile phase such as water and methanol. In our studies, the gradually decreasing AUC of the miriplatin standards indicate that miriplatin may not be precisely quantified by HPLC due to its low solubility and stability in water and methanol, even though the calibration curves from HPLC were in good linearity after the preparation of the platinum standards. Therefore, the quantification method by HPLC was not applied further to quantify miriplatin in its nano formulations.

3.3.2 Mass Spectrometry of Miriplatin

ESI-MS: chemical formula: $C_{34}H_{68}N_2O_4Pt$, m/z value of the most abundant isotope peak of $[M^+ + H]^+$: calculated 764.490518, found 764.8. Chemical Formula: $C_{20}H_{41}N_2O_2Pt$, $[M^+]^+$:

calculated 536.281588, found 536.1; $[M''+H_2O]^+$: calculated 554.292153, found 554.1;

$[M''+CH_3OH]^+$: calculated 568.307803, found 568.3.

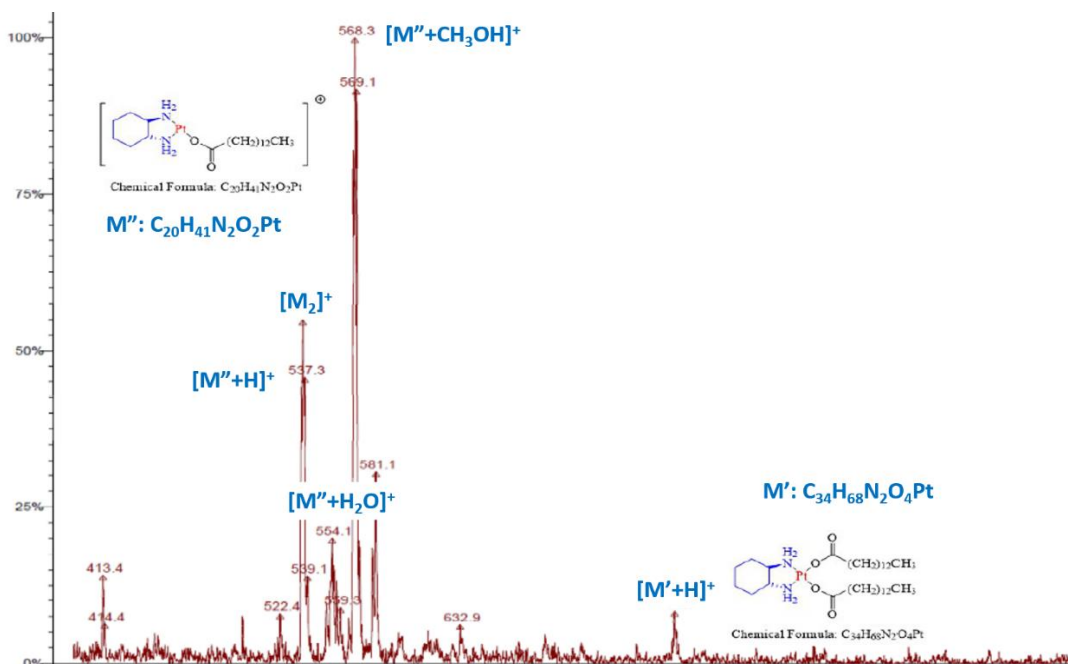


Figure 3.5. ESI-MS mass spectrum of miriplatin.

From the ESI-MS mass spectrum in Figure 3.5, we found that the strongest peak corresponds to miriplatin molecules that have lost one myristate chain. But this could be explained by the prior findings that miriplatin was not stable in methanol and existed as a molecule losing one chain. Miriplatin was not easily ionized so the temperature and voltage setting of its ESI-MS needed to be increased, which would enhance its degradation. However, this phenomenon indirectly supports our hypothetical mechanism of the anticancer activities of miriplatin-loaded nano formulations, in which miriplatin would degrade into myristate chains and other platinum-containing fragments, which would then be released from the nano formulation to kill the surrounding cancer cells.

3.3.3 Quantification of Miriplatin by ICP-OES

3.3.3.1 Calibration curve of platinum standard solutions by ICP-OES. As shown in Figure 3.6, the calibration curves of platinum standard solutions measured at wavelengths 214.4 and 265.9 nm were established by ICP-OES. Both of them had high R square (0.9999) indicating that the concentration of platinum had a linear relationship with ICP-OES signals over the concentration range from 10 ng/mL to 100 μ g/mL. We found the ICP-OES signals at 10 ng/mL or lower platinum concentrations no longer fit to the calibration curves very well, indicating that the limit of detection (LOD) of the instrument was around 10 ng/mL platinum. This LOD of ICP-OES is critical for the quantification of platinum-based drugs, especially in animal studies, whose samples will contain highly diluted platinum in blood. Due to the LOD and high volume for ICP-OES measurements (around 6 mL for each sample), further biological studies of platinum nano formulations *in vitro* and *in vivo* need to be designed carefully to ensure enough volume and concentration for each sample.

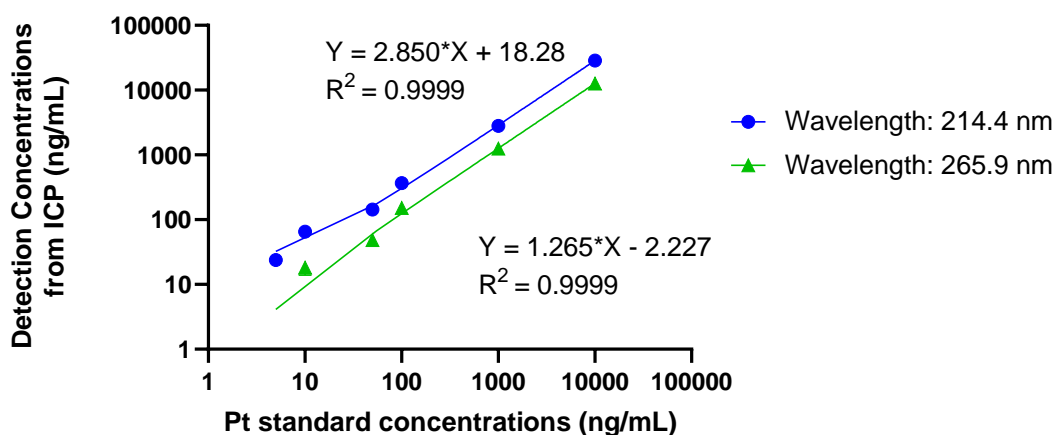


Figure 3.6. Calibration curves of platinum standard solutions at wavelength 214.4 and 265.9 nm by ICP-OES.

3.3.3.2 Calibration curves of different forms of platinum. It is well known that ICP only trace the element no matter what form it is. As shown in Figure 3.7, different forms of platinum including platinum standard solution, cisplatin and miriplatin at the same platinum concentrations showed great consistency with each other. Thus, the measurement would reflect the concentration of miriplatin (or other platinum-based drugs such as cisplatin and oxaliplatin) and its degradation products. The limit of detection of the three forms of platinum was all around 10 ng/mL, which was consistent with the result mentioned in 3.3.3.1.

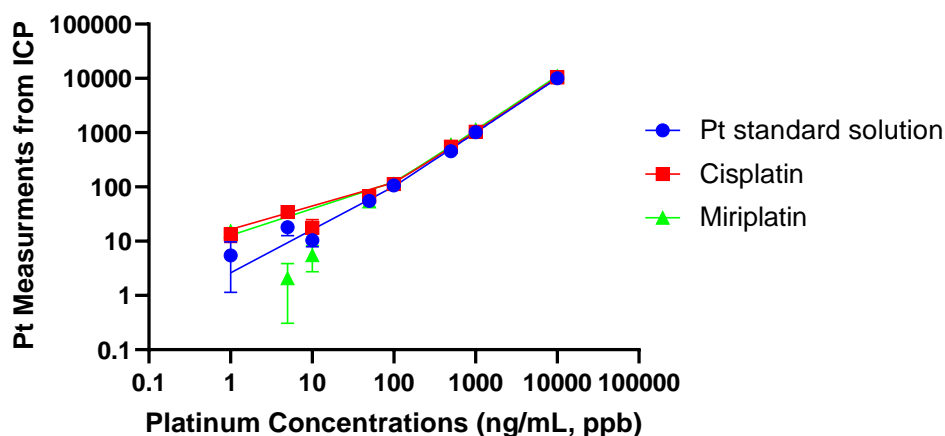


Figure 3.7. Calibration curves of different forms of platinum (platinum standard solution, cisplatin, miriplatin) at wavelength 214.4 nm by ICP-OES.

3.3.4 Recovery in the Quantification of Platinum from Miriplatin-Loaded Nano Formulations by ICP-OES

Different digestion methods (nitric acid, sulfuric acid and aqua regia) have been tried to optimize the recovery in quantifying the platinum from miriplatin-loaded nano formulations by ICP-OES in preliminary studies. Although some manuals suggested using aqua regia for the digestion of formulations consisting of platinum [117, 118], this digestion method was

abandoned in later study because it was far more dangerous than the others and needed high diluted of the digested sample before its injection into the ICP-OES instrument. Nitric acid and sulfuric acid showed similar recoveries of platinum from nano formulations. Based on our preliminary data and on the usage experiences of Dr. Zhao's lab, heating in 70 % nitric acid at 90 °C for 90 min was chosen to digest nano formulations in further experiments.

3.3.4.1 Comparison of platinum recovery from different miriplatin-loaded nano formulations. The composition and platinum recovery of miriplatin-loaded SLNs prepared by different procedures were shown in Table 3.1. All nano formulations were digested by 70% nitric acid at 90 °C for 90 min.

The two initial scale-up methods to prepare miriplatin-loaded nano formulations, namely chloroform dripping method and chloroform injection method gave the lowest platinum recoveries, which was probably due to the loss of miriplatin during the dripping/injection procedure. When chloroform solution touched the hot aqueous phase (75 °C), chloroform would evaporate very quickly to precipitate out lots of lipids and the payload miriplatin due to their low solubility in water. This quick precipitation would then prevent miriplatin from assembling with the lipids to yield a high loading or high recovery of platinum.

The solvent evaporation method with or without co-solvent and the slow evaporation method improved the platinum recovery significantly (from 10% to 20-30%). It is probably because the slow evaporation gave the two phases (organic phase and aqueous phase) more time to mix well and gave the lipids and miriplatin more time to form nanoparticles together in aqueous phase slowly. Adding co-solvent and slow evaporation were two positive contributors to platinum recovery but they did not show prominent improvement individually. Co-solvent

could help lipids transfer from organic phase to aqueous phase gradually and smoothly because of the better miscibility while slow evaporation could let two phases have more time to mix and transfer. Furthermore, the platinum recovery improved drastically from 20% to 80% when both slow evaporation and co-solvent were applied. Such a high platinum recovery of the improved formulations warrants their further characterizations.

Table 3.1
Composition and Platinum Recovery of Miriplatin-Loaded SLNs (90% TM or TP/10% PE-PEG₂₀₀₀ +20% Miriplatin) Prepared by Different Preparation Procedures

SLN Compositions + drug input (%)	Preparation methods	Platinum recovery (%)
90% TM/10% PEG + 20% Miri	Chloroform dripping	9.02
90% TP/10% PEG + 20% Miri	Chloroform dripping	9.57
90% TM/10% PEG + 20% Miri	Chloroform injection	3.60
90% TP/10% PEG + 20% Miri	Chloroform injection	12.10
90% TM/10% PEG + 20% Miri	Chloroform evaporation	22.40
90% TP/10% PEG + 20% Miri	Chloroform evaporation	24.90
90% TM/10% PEG + 20% Miri	Co-solvent evaporation	20.00
90% TP/10% PEG + 20% Miri	Co-solvent evaporation	31.50
90% TM/10% PEG + 20% Miri	Chloroform slow evaporation	21.20
90% TP/10% PEG + 20% Miri	Chloroform slow evaporation	29.60
90% TM/10% PEG + 20% Miri	Co-solvent slow evaporation	87.80
90% TP/10% PEG + 20% Miri	Co-solvent slow evaporation	80.10

(TM: trimyristin, TP: tripalmitin, Miri: miriplatin, PEG: 1,2-distearoyl-sn-glycero-3-phosphoethanolamine-N-[methoxy(polyethylene glycol)-2000] (ammonium salt))

Nonetheless, the platinum recovery quantified by ICP-OES cannot be simply taken as the encapsulation efficiency of the nano formulations because the ICP traces the platinum element regardless of its form. Due to its extremely low water solubility, we can reasonably assume that free, intact miriplatin does not substantially partition into the bulk aqueous phase. However, miriplatin may degrade (losing myristate chains) to convert its platinum into water-soluble form(s) after long exposure to water. In this way, other forms of platinum (miriplatin degradation products) could still be detected by ICP so that the actual encapsulation efficiency may be lower than the platinum recovery. Therefore, the separation and quantification of different forms of platinum are needed to more precisely assess the encapsulation efficiency. Possible techniques in this regard include chloroform extraction and ^{195}Pt -NMR [119, 120]. Moreover, storage procedures such as lyophilization and spray-drying are also needed to be considered in order to reduce the time that miriplatin exposed to aqueous solution.

3.3.4.2 Platinum recovery of miriplatin-loaded nano formulations prepared by co-solvent slow evaporation. The composition and platinum recovery of miriplatin-loaded SLNs and micelles that were prepared by the co-solvent slow evaporation method are shown in Table 3.2 and Table 3.3. All nano formulations were digested by 70% nitric acid at 90 °C for 90 min. The platinum recovery of all such nano formulations were 70 % or higher. There was no significant difference in platinum among different compositions. Adding cholesterol or another anticancer drug Paclitaxel did not influence the platinum drug recovery, either. The reproducibility could be improved by controlling the temperature increase more consistently for each batch.

Table 3.2
Composition and Platinum Recovery of Selected SLN Formulations Prepared by Co-Solvent Slow Evaporation Method

SLNs Compositions	Drug input (%)	Platinum recovery (%)
90% TM/10% PE-PEG ₂₀₀₀	20% miriplatin	76.20
90% TP/10% PE-PEG ₂₀₀₀	20% miriplatin	86.30
90% TM/10% PE-PEG ₂₀₀₀	20% miriplatin + 10% PTX	83.20
90% TP/10% PE-PEG ₂₀₀₀	20% miriplatin + 10% PTX	74.40
80% TM/10% Chol/10% PE-PEG ₂₀₀₀	20% miriplatin	69.50
80% TP/10% Chol 10%/PE-PEG ₂₀₀₀	20% miriplatin	81.40

(TM: trimyristin, TP: tripalmitin, Miri: miriplatin, PEG: 1,2-distearoyl-sn-glycero-3-phosphoethanolamine-N-[methoxy(polyethylene glycol)-2000] (ammonium salt), Chol: cholesterol, PTX: paclitaxel)

Table 3.3
Composition and Platinum Drug Recovery of Selected Micelle Formulations Prepared by Co-Solvent Slow Evaporation Method

Micelles Compositions	Drug input (%)	Platinum recovery (%)
100% PE-PEG ₂₀₀₀	20% miriplatin	80.80
100% PE-PEG ₂₀₀₀	20% miriplatin + 10% PTX	77.70

(TM: trimyristin, TP: tripalmitin, Miri: miriplatin, PEG: 1,2-distearoyl-sn-glycero-3-phosphoethanolamine-N-[methoxy(polyethylene glycol)-2000] (ammonium salt), Chol: cholesterol, PTX: paclitaxel)

3.3.5 Morphology of Miriplatin-Loaded Nano Formulations

Miriplatin-loaded nano formulations prepared by co-solvent evaporation method were then subjected to morphological studies by TEM imaging.

3.3.5.1 Morphology of miriplatin-loaded micelles. As shown in Figures 3.8 and 3.9, micelles loaded with miriplatin only or with miriplatin and paclitaxel showed as little white dots under TEM. Both of them had size around 10 nm, which was consistent with the size data measured by dynamic light scattering. There was no obvious morphological difference between the two compositions of micelles. The shape of micelles could not be observed clearly under TEM due to the extremely small particle size. Some papers have reported that micelles consisting of phospholipids or phospholipids-PEG conjugate had similar spherical structures [121, 122].

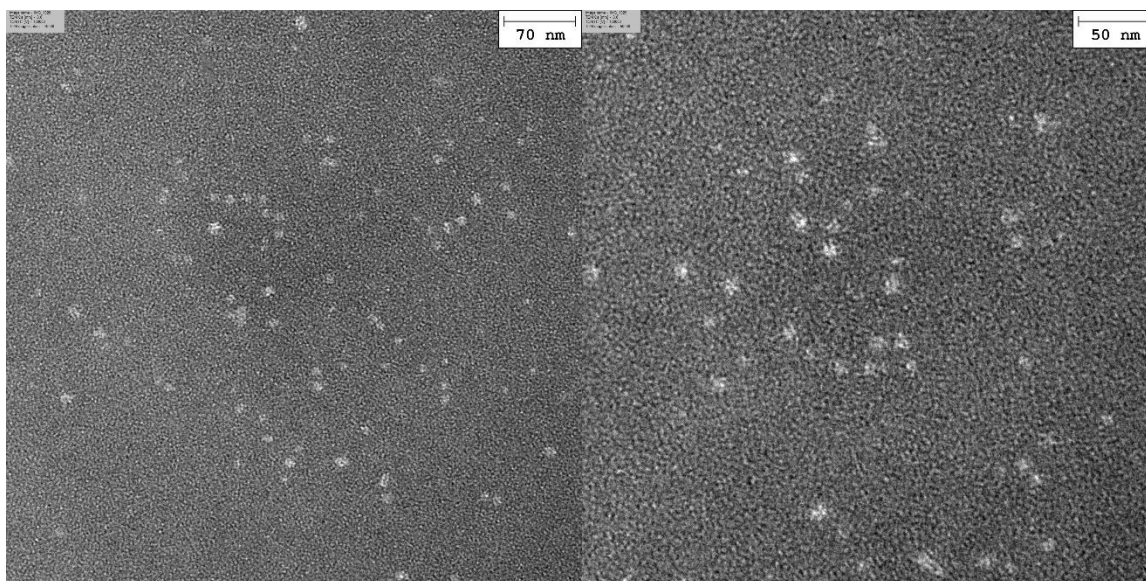


Figure 3.8. TEM images of miriplatin-loaded micelles (100% PE-PEG₂₀₀₀ + 20% miriplatin).

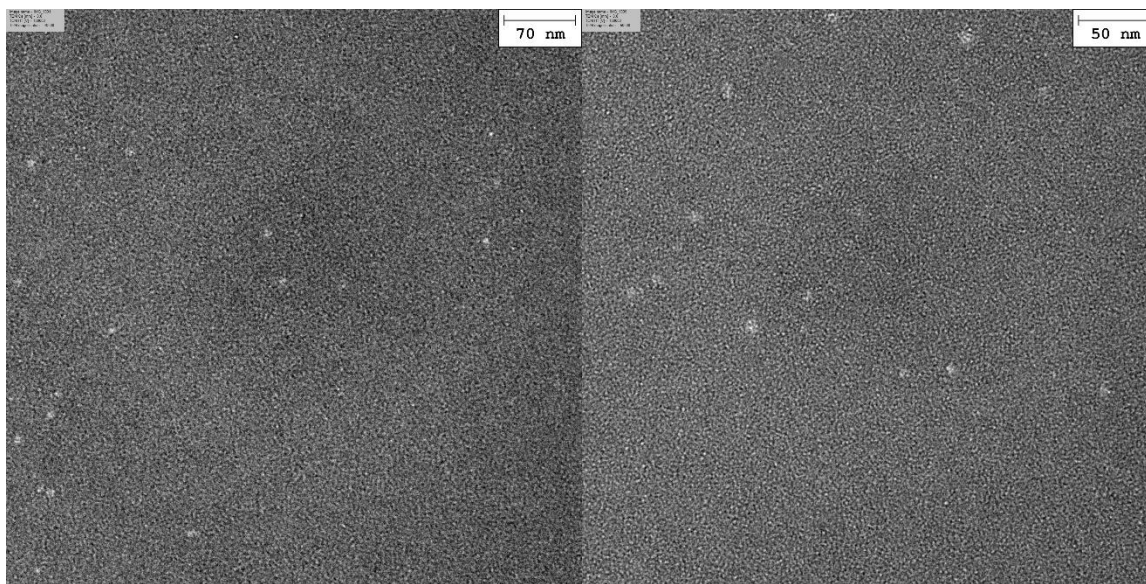


Figure 3.9. TEM images of miriplatin/paclitaxel-loaded micelles (100% PE-PEG₂₀₀₀ + 20% miriplatin + 10% paclitaxel).

3.3.5.2 Morphology of miriplatin-loaded SLNs.

3.3.5.2.1 *TM versus TP.* The TEM images of SLNs consisting of TM or TP and loaded with miriplatin are shown in Figure 3.10 and Figure 3.11. SLN with TP showed the morphology of round-shape spheroids, while SLN with TM showed a mixture of spherical and rod structures. It was reported that the shape (aspect ratio, AR) of lipid molecule impacted the shape of their nanoparticles [77, 123]. When the size of the lipid head group is similar to the lipid tail (with an AR of ~ 1), the lipid molecules tend to form spheres while rods are formed when the lipid tail is bigger than the lipid head group (with an AR > 2) [123]. However, our SLNs which consisted of TM (containing two C-14 chains) formed rod-shaped nanoparticles while SLNs which consisted of TP (containing two C-16 chains) formed spherical nanoparticles. TP might better bridge between the lipid tail of PE-PEG conjugate (containing two C-18 chains) and that of miriplatin (containing C-14 chains) to mix all the three components to form the sphere. As to SLNs with

TM, most of the component molecules had C-14 chains (TM and miriplatin) so they would tend to phase separate to form rods. The shape of nanocarriers have a huge effect on their behavior *in vivo* behavior, such as cellular uptake [76, 77, 123, 124]. Some researchers reported that sphere-shaped nanoparticles are more efficiently internalized by cells compared to rod-shaped ones, but some recent studies showed contradictory results[76, 77, 123, 125]. Other than shape, factors such as size, surface chemistry and material composition also influence the permeation into cell membranes[77, 78]. Hence, both spherical shape and rod-shape warrant further *in vitro* and *in vivo* studies.

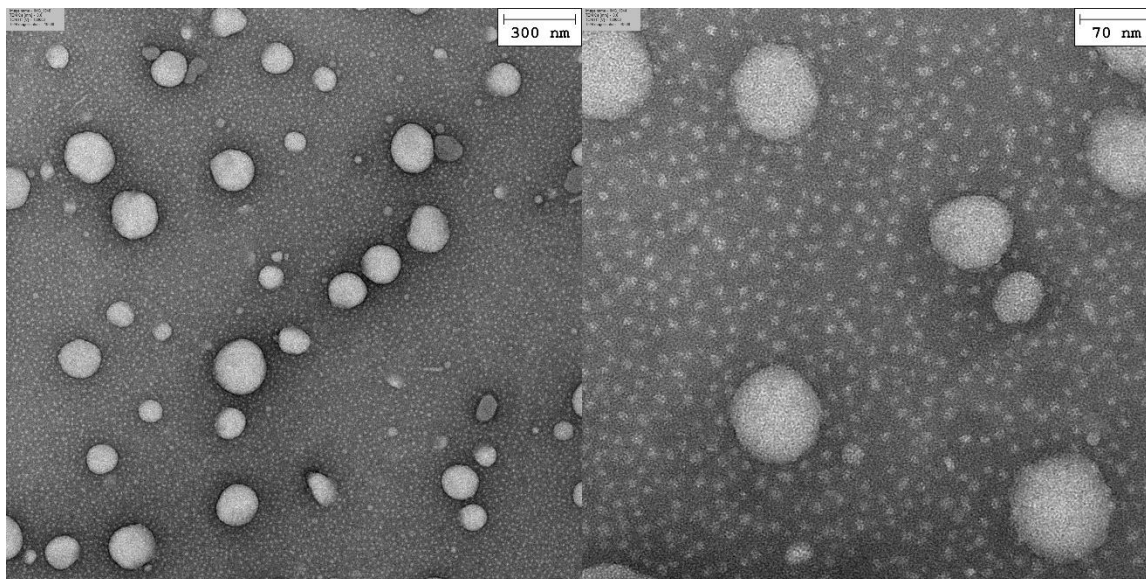


Figure 3.10. TEM images of miriplatin-loaded SLNs consisting of TP (90% TP/10% PE-PEG₂₀₀₀ + 20% miriplatin).

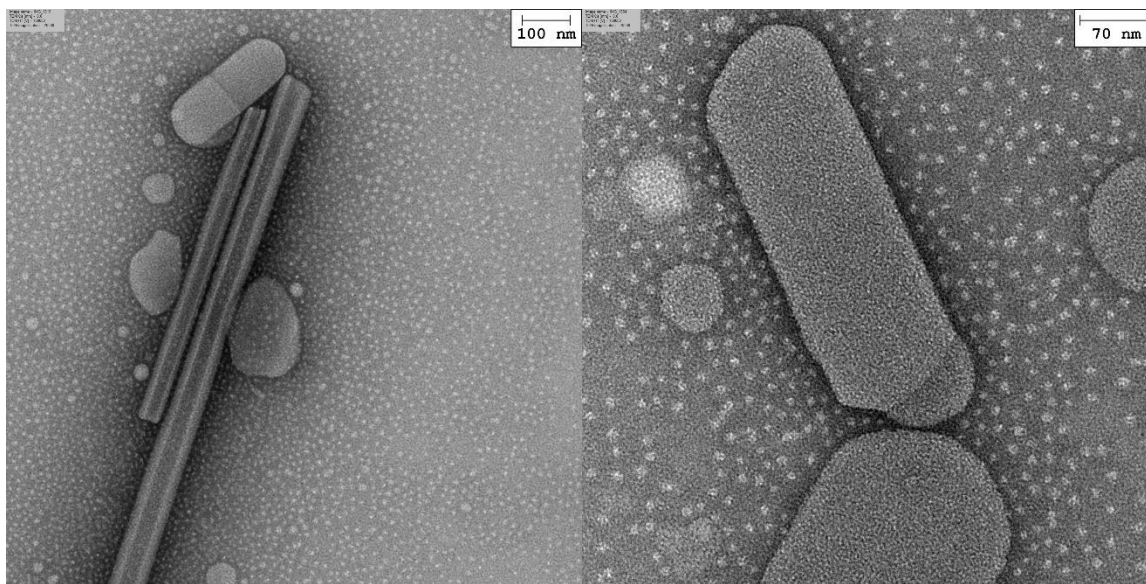


Figure 3.11. TEM images of miriplatin-loaded SLNs consisting of TM (90% TM/10% PE-PEG₂₀₀₀ + 20% miriplatin).

Both TM-containing and TP-containing SLNs averaged around 100 nm in diameter, which was consistent with the sizing data from Zetasizer. These TEM images also support that the number-based size distribution analyzed from Malvern Zetasizer software could represent the size of the majority of nanoparticles. They had size distribution from 50 to 150 nm, which was consistent with the high PDI values in their dynamic light scattering studies, both indicating the substantial heterogeneity of the formulations. Some smaller particles (observed as 20-30 nm) might be formed by the instability and degradation from bigger particles. The ones having size around 10 nm could be explained by the self-assembly of only PE-PEG₂₀₀₀ and the formation of micelles (similar to Figure 3.8 and Figure 3.9).

3.3.5.2.2 Effect of loading multiple drugs. The TEM images of miriplatin/paclitaxel loaded SLNs (TP) are shown in Figure 3.12. Such SLNs loaded with both miriplatin and paclitaxel showed similar morphology to the SLNs (TP) loaded only with miriplatin, both having

spherical shape and size around 100 nm. There was no significant difference in the physiochemical properties (including sizes, platinum drug recovery and morphology) between the SLNs loaded with a single drug and a combination of two drugs. The black dots observed in the left figure might be platinum-related compounds (miriplatin or its degradation products), which could scatter electrons to display as darker particles of heavy metal against the background. Some studies on cisplatin-loaded liposomes and platinum-based nanoparticles have showed similar results [126, 127]. However, the black dots could not be found in most other TEM images, so there is another possible explanation that the dark dots were caused by excessive staining agent (uranyl acetate). Compared to liposome formulations, the SLN formulations consisting of solid lipids and PE-PEG₂₀₀₀ conjugate had much more lipophilic structure so they were difficult to be penetrated by the staining agent. Therefore, miriplatin and its degradation products may not be easily observed under TEM.

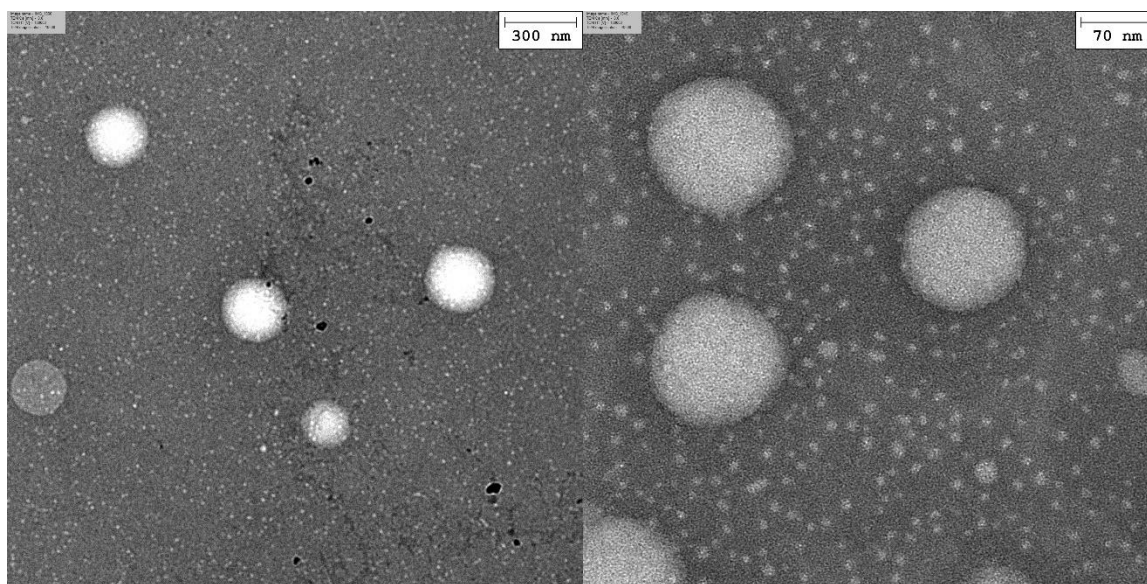


Figure 3.12. TEM images of miriplatin/paclitaxel loaded SLNs of TP (90% TP/10% PE-PEG₂₀₀₀ + 20% miriplatin + 10% paclitaxel).

3.3.5.2.3 Effect of cholesterol. The TEM images of miriplatin-loaded SLNs (TP) containing cholesterol are shown in Figure 3.13. Compared to SLNs (TP) without cholesterol, they showed milky and brighter spheres. The TEM images also showed wider size distribution and a combination of various structures including spheroids, rods and irregular shape, indicating higher heterogeneity of the formulation. Hence, cholesterol did not improve the stability or homogeneity of the SLNs as we expected from their function as a common bilayer stabilizer [107]. However, different percentages of cholesterol and other stabilizers such as cholesteryl palmitate as mentioned in Chapter 2 may be included in the SLNs in future studies.

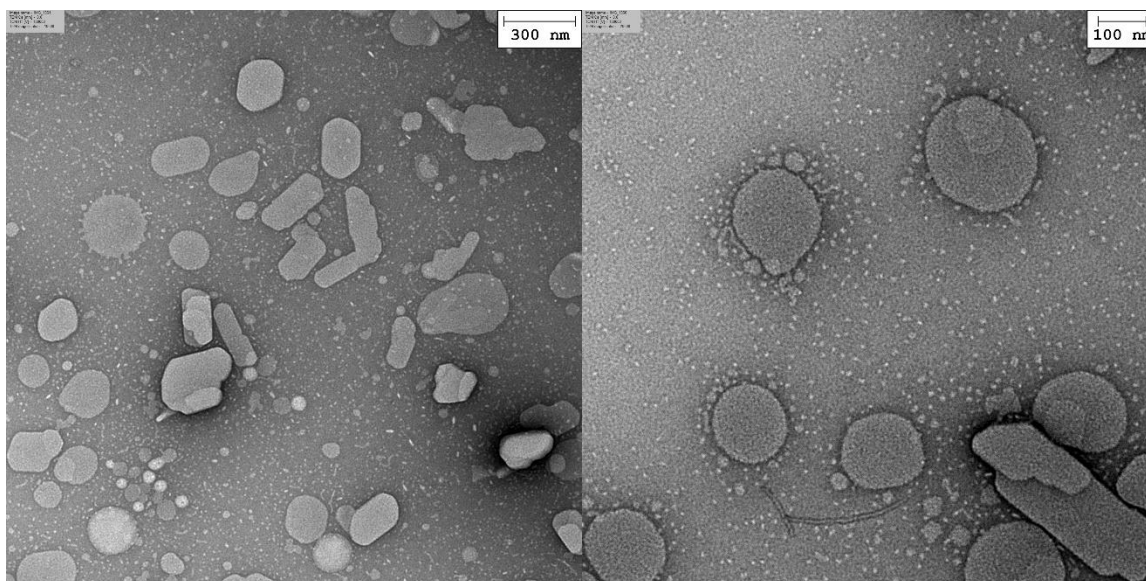


Figure 3.13. TEM images of miriplatin-loaded SLNs (TP) containing cholesterol (80% TP/10% cholesterol/10% PE-PEG₂₀₀₀ + 20% miriplatin).

3.4 Summary

HPLC and ICP-OES techniques were attempted to quantify miriplatin. Miriplatin was characterized by ESI-MS, which confirmed its chemical structure. A quantification method for miriplatin was established using ICP-OES, which showed good consistency in different platinum-containing samples including platinum standard solutions, cisplatin and miriplatin. Recovery in the quantification of different miriplatin-loaded nano formulations was promoted by digestion with 70% nitric acid and heating. The co-solvent slow evaporation method to prepare platinum nano formulations improved the platinum recovery prominently from 10% to 70%. The advantages and disadvantages of different methods to prepare platinum nano formulations are summarized in Table 3.4. Other techniques are still needed to quantify the encapsulation efficiency of miriplatin-loaded formulations in the future.

Miriplatin-loaded nano formulations with different compositions were negatively stained with uranyl acetate and then imaged by TEM, which showed the size and morphology of the miriplatin-loaded nano formulations that were consistent with size and PDI data from dynamic light scattering studies by the Malvern Zetasizer. In the TEM studies, micelles showed a morphology of spherical dots at around 10 nm in diameter while SLNs showed both spherical and rod structures with a size distribution from 50 to 150 nm.

Table 3.4
Comparison of Different Preparation Methods

Preparation methods	Pros	Cons
Thin-film hydration	Easy to prepare	Poor reproducibility Hard to scale-up
Chloroform dripping/injection	Simple Better homogeneity	Low drug recovery
Chloroform evaporation	Simple	Poor homogeneity
Co-solvent evaporation	Slightly higher drug recovery	Larger size Poor homogeneity
Slow evaporation	Slightly higher drug recovery	Poor homogeneity Control T manually
Co-solvent slow evaporation	Significantly higher drug recovery	Poor homogeneity Control T manually

CHAPTER 4: EVALUATION OF ANTICANCER ACTIVITY OF MIRIPLATIN-LOADED NANO FORMULATIONS AGAINST 3D MCS

4.1 Introduction

The application of nanotechnology to clinically established medicine has prompted the design and development of various drug-loaded nanocarriers to treat cancer [128]. However, only a few nano formulations have been successfully translated into medicine in clinic [129]. Although huge resources have been invested in cancer research and nanotechnology, the approval rate of neither anticancer drugs nor nanomedicines is above 5% [129, 130]. One main reason for such low rate of success is the gap between pre-clinical cell culture and animal models of cancer and real life cancer diseases [129, 130]. The current main strategies of screening anticancer drugs are to use two-dimensional (2D) cell models and animal models. However, in the last decade, it has been recognized that models of 2D monolayer cells cannot precisely select clinically successful anticancer drugs [131].

Although 2D cell culture models carry many advantages including simplicity, low-cost, reproducibility and high-throughout, it cannot mimic many unique features of solid tumors. Firstly, 2D cell cultures lack many of the cell-cell and cell-matrix interactions seen in the tumor microenvironment. Secondly, traditional 2D cell culture models lack many of the solid tumors' physiological barriers against anticancer agents, which is the main reason that drug molecules cannot easily penetrate into solid tumors [132]. Thirdly, 2D cell cultures also lack the heterogeneity in oxygen, metabolites and pH, which are usually present in solid tumors. Therefore, 2D cell culture models often incorrectly predict the efficacy and toxicity of an

anticancer drug candidate, which would finally cause the failure in its clinical validation and approval [133, 134].

Three dimensional multicellular spheroids (3D MCS) were first established by Sutherland et al in the 1970s [135]. 3D MCS contain many features of solid tumors that are missing in 2D cell culture model [136]. As shown in Picture 4.1, the 2D cell cultures result in monolayer cells expanding on a flat surface while 3D cell cultures cause cells to form three-dimensional spheroids using an ECM material [133]. 3D MCS can retain the characteristics of solid tumors in patients very well and can create substantial barriers for drugs to penetrate [129]. Spheroids with a diameter larger than 400–500 μm usually formed a hollowed-heart structure consisting of an exterior layer of reproducing cells (proliferating zone), a middle layer of quiescent zone and an internal necrotic core [129, 133, 137]. The various stages of cells within the spheroid structure are established due to the gradients of oxygen and nutrients levels [138, 139]. A schematic diagram of the structure of 3D MCS with different zones and inside gradients is shown in Picture 4.1. In addition, 3D MCS can be cultured *in vitro* for weeks for long term research and can be developed into co-culture models with other cells to better mimic the cell-cell interaction [129]. Thus, a 3D MCS model carrying these characteristics can serve as a better *in vitro* model than 2D cell culture models to mimic the solid tumor microenvironment and to better predict the clinical efficacy of anticancer drug candidates.

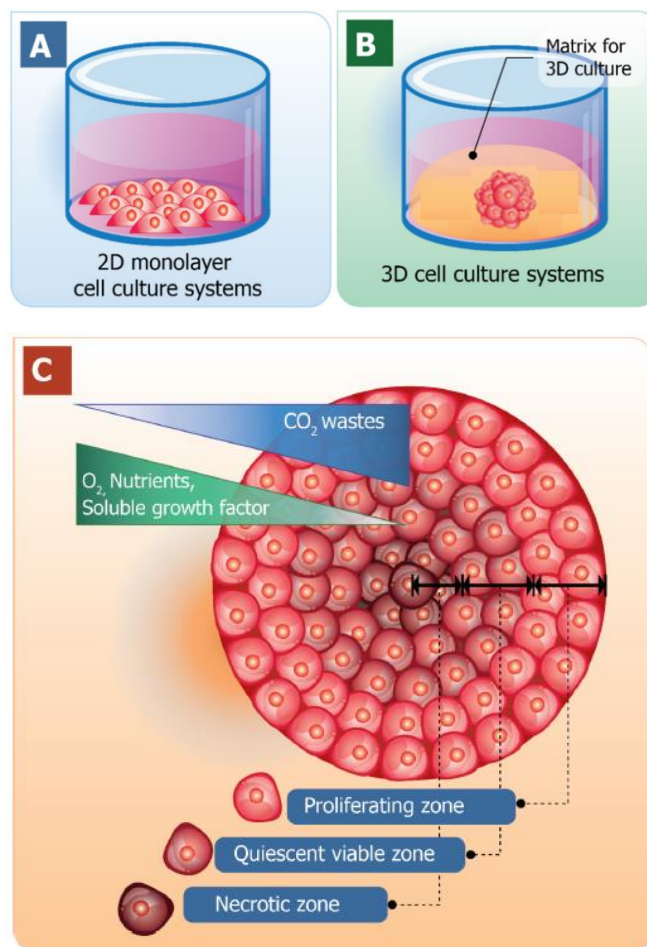


Figure 4.1. Schematic diagrams of the traditional two-dimensional monolayer cell culture (A) and three-dimensional cell culture systems (B, C). Adapted from [133].

3D MCS models have been widely used in preclinical studies on drug-loaded nano delivery systems. Torchilin's Group detected increased BCL-2 expression in an ovarian 3D MCS model and used it to study the accumulation and toxicity of doxorubicin-loaded PEG-PE micelles and solid lipid nanoparticles (co-loaded with doxorubicin and alpha-tocopherol succinate) to overcome drug resistance [140, 141]. 3D MCS were also used to investigate the EPR effect [65], which serves as the main mechanism of tumor targeting by nanocarrier-based drug delivery systems. The penetration and retention of nanocarriers were evaluated in 3D MCS that could reflect the vascular structure in solid tumors. For example, N. Ho *et al* developed

MCS that contain both cancer cells and vasculature endothelial cells to evaluate the penetration of Fe_3O_4 nanoparticles and found that such nanoparticles selectively targeted the MCS containing the endothelial cells and inhibited their growth more effectively than free drugs [142]. Further, 3D MCS can be inoculated into animals to establish patient-derived xenograft (PDX) models *in vivo* [143].

In this chapter, lung adenocarcinoma A549 and A549-iRFP cells were constructed into 3D MCS (Figure 4.2) and used to evaluate the anticancer activity of miriplatin-loaded nano formulations.

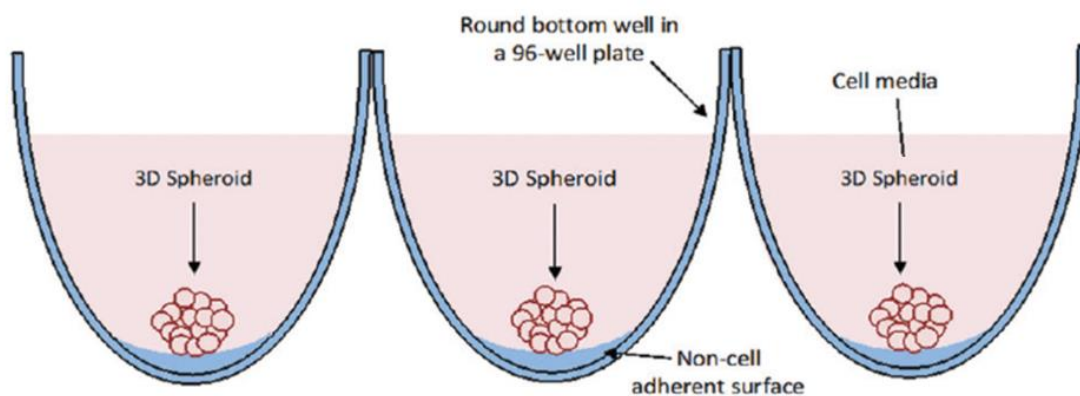


Figure 4.2. Schematic diagrams of 3D MCS produced by seeding cells into 96-well microplate plates with noncell adherent surfaces. Adapted from [144].

4.2 Materials and Methods

4.2.1 Cell Culture Maintenance

Human lung adenocarcinoma A549 cell line was purchased from ATCC (Manassas, VA), Human lung adenocarcinoma A549-iRFP cell line ($\lambda_{\text{ex}} = 690 \text{ nm}$, $\lambda_{\text{em}} = 713 \text{ nm}$) was purchased

from Imanis Life Sciences (Rochester, MN). Cell culture reagents, if not specified, were purchased from Corning Life Science. All cells were maintained at 37°C and 5% CO₂. A549 cells were grown in Roswell Park Memorial Institute Medium (RPMI) cell culture media with supplemented 10% Fetal bovine serum (Gemini Bio-Products, CA) and 1% penicillin-streptomycin. A549-iRFP cells were grown in Dulbecco's Modification of Eagle's Medium (DMEM) cell culture media supplemented with 10% Fetal bovine serum (Gemini Bio-Products, CA), 1% penicillin-streptomycin and 1 µg/ml puromycin (Alfa Aesar, US).

4.2.2 Fluorometric Characterization of A549-iRFP Monolayer Cells

A549-iRFP cells were seeded onto Falcon™ 96-Well Black/Clear flat-bottom microplates (Corning Life Science, US) at 0, 100, 200, 500, 800, 1000, 2000, 5000, 8000 and 10000 cells/well. The fluorescent signal ($\lambda_{\text{ex}}=685$ nm, $\lambda_{\text{em}}=700$ nm) was monitored by Odyssey® Infrared Imaging 205 System (LI-COR® Biosciences, Lincoln, NE, USA) at the 700 nm channel. The cell viability was measured by UV absorbance at 490 nm on a Synergy HTX microplate reader (BioTek, US) using the CellTiter 96® AQueous One Solution Cell Proliferation Assay (Promega Corporation, WI, US).

4.2.3 3D MCS Formation

A549 and A549-iRFP cells were seeded onto 96-well ultra-low attachment spheroid microplates (Corning Life Science, US) at 3000 cells/well in 100 µL/well of the aforementioned growth medium that was supplemented with 0.3% collagen (Gibco, US). The microplates were centrifuged at 7 °C, 300 g for 7 minutes on an Eppendorf Centrifuge 5810R to facilitate the aggregation. The cells were cultured for 48 hours and then supplemented with another 100 µL/well growth medium without collagen. Every two days thereafter, the medium was changed

by replacing 100 μL of growth medium in each well with 100 μL fresh growth medium without collagen to maintain a 200 μL total media volume. The morphology of 3D MCS were monitored by a Keyence (US) BZ-X700 fluorescence microscope.

4.2.4 Cell Viability Assays for Miriplatin-Loaded Nano Formulations on 3D MCS

A549 and A5499-iRFP cells (3000 cells/well) within 15 passages were seeded into 96-well ultra-low attachment spheroid microplates (Corning Life Science, US) to form 3D MCS using the method described above. After 6-8 days when 3D MCS grew to $\sim 500 \mu\text{m}$ in diameter, they were treated with free chemotherapeutic agents (cisplatin, miriplatin, paclitaxel) and miriplatin-loaded nano formulations at the same platinum/paclitaxel input concentrations in complete medium. Cisplatin was dissolved into complete medium directly while miriplatin and paclitaxel were dissolved into complete medium containing 1% DMSO.

After incubation for 3 days at 37 $^{\circ}\text{C}$, 5% CO_2 , the growth medium in each well was removed completely and replaced by 200 μL fresh growth medium. After incubation for 2 more days, 100 μL of the growth medium in each well was replaced with 100 μL fresh growth medium to maintain a 200 μL total media volume. After incubation for another 2 days (3-day exposure plus 4-day growth = 7 days in total), 3D MCS of each treatment group were transferred to an opaque-walled 96-well plate with 100 μL medium in each well. An equal volume (100 μL) of CellTiter-Glo 3D Cell Viability Assay (Promega Corporation, WI, USA) was added to each well. The plate was shaken for 5 minutes and incubated for an additional 25 minutes at room temperature to stabilize the luminescent signal. The luminescence was then recorded by a Synergy HTX microplate reader (BioTek, US). The 3D MCS that were treated only with the

growth media were assayed following the same procedure and taken as 100% viability (0% inhibition) reference. Samples were evaluated in quadruplicates.

The fluorescent signal ($\lambda_{\text{ex}} = 685 \text{ nm}$, $\lambda_{\text{em}} = 700 \text{ nm}$) of A549-iRFP 3D MCS was monitored daily during the 7-day treatment by Odyssey® Infrared Imaging 205 System (LI-COR® Biosciences, Lincoln, NE, USA) at the 700 nm channel. The fluorescent signal of the 3D MCS that were treated only with the growth media were taken as the reference for 100% viability (0% inhibition). Samples were evaluated in quadruplicates.

The cell growth inhibition by miriplatin-loaded nano formulations are calculated by the formula below:

$$\text{Cell Growth Inhibition (\%)} = 100\% - \text{Cell Viability (\%)}$$

4.3 Results and Discussion

4.3.1 Correlation of Fluorescent Signal in A549-iRFP Monolayer Cells with Cell Seeding Density and Cell Viability

A strong linear relationship was found between iRFP fluorescent signal of A549-iRFP monolayer cells and cell seeding density. A linear relationship was also found between such fluorescent signal and the cell viability. As shown in Figure 4.3, the fluorescent signal increased with the increase of cell seeding density ($R^2=0.9902$) and with the cell viability ($R^2 = 0.9313$) as long as the seeding density was in the range of 1000 to 10000 cells/well. The fluorescent signal of A549-iRFP cells at seeding density below 1000 cells/well was too low to be quantified precisely. With this relationship, the trend of the cell growth can be monitored by the iRFP fluorescent signal of A549-iRFP cells. Although this correlation cannot be used to quantify the

cell viability as precisely as the 3D cell viability assay, it allows dynamic assessment of the MCS viability over the course of long treatments (7 days). The dynamic monitoring of the iRFP fluorescence can not only assess the rate of cancer cell killing by anticancer agents/drug-loaded delivery systems, but also assess whether the cancer cells in MCS will relapse after long term exposure. For future studies, the correlation between the fluorescent signal of iRFP and seeding density/viability should also be validated in 3D MCS.

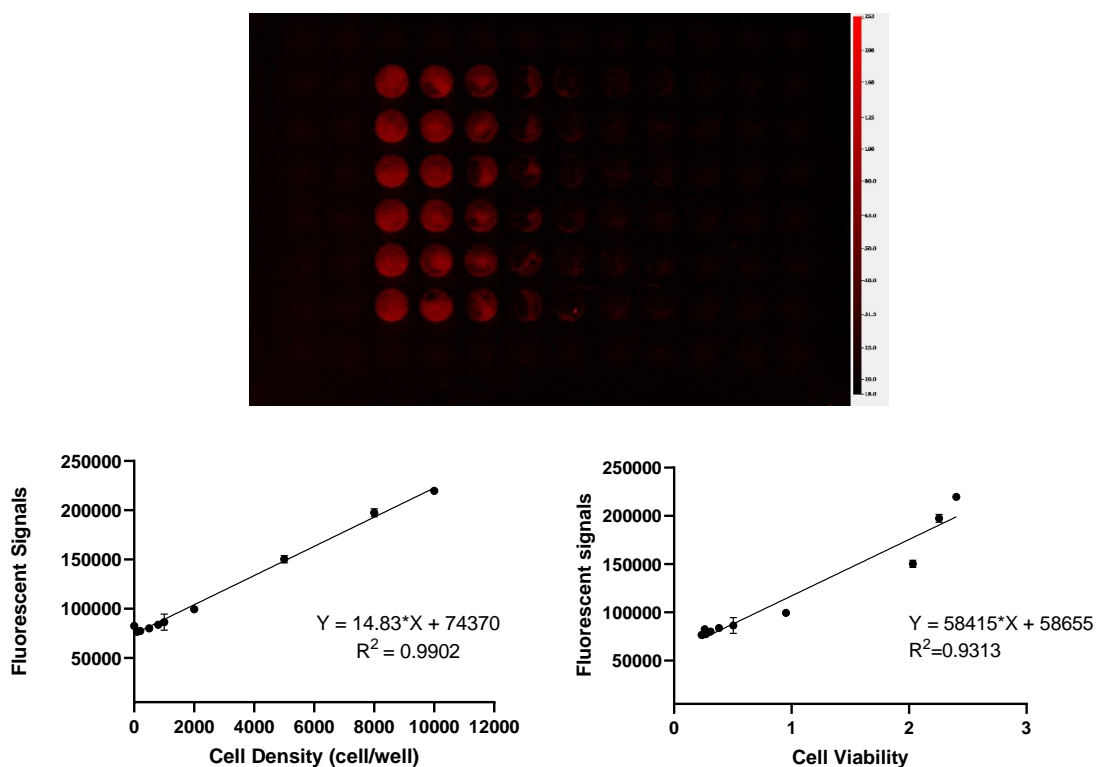


Figure 4.3. Correlation of iRFP fluorescent signal in A549-iRFP monolayer cells with cell seeding density (lower left) and with cell viability (lower right). (Mean \pm S.D, N = 6).

4.3.2 Formation of 3D MCS

The 3D MCS of two lung cancer cell lines (A549 and A549-iRFP) were successfully constructed at selected seeding density (3000 cells/well) with the help of centrifugation and

collagen addition in the growth media. The resultant 3D MCS showed a round, tight structure in the first 15 days (Figure 4.4). The edge of MCS was smooth and clear in the first 10 days but became fuzzy and rough from Day 13. MCS grew into ~500 μm in diameter after 5 to 7 days. As reported previously [129, 133, 137], spheroids with diameter larger than 400–500 μm transformed into a hollowed-heart structure consisting of an exterior layer of reproducing cells (proliferating zone), a middle layer of quiescent cells and a core of necrotic cells.

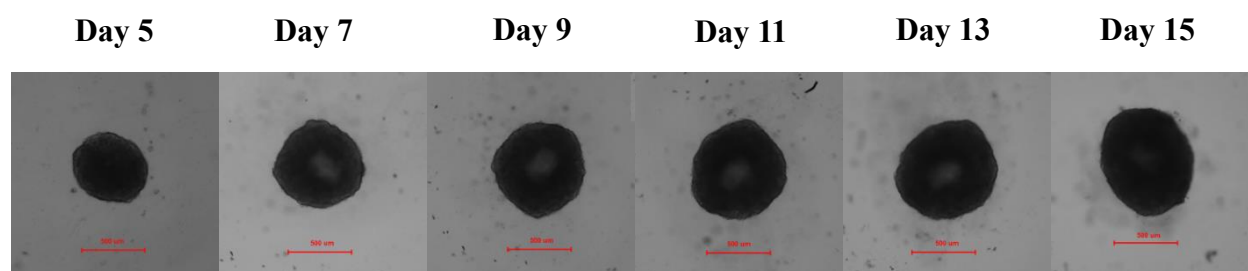


Figure 4.4. Morphology of A549-iRFP 3D MCS (3000 cells/well) after 5, 7, 9, 11, 13, 15 days of culturing (scale bar=500 μm).

4.3.3 Comparison between Sensitivity of A549 and that of A549-iRFP 3D MCS to Anticancer Drugs and Nano Formulations

In order to validate A549-iRFP MCS as an alternative *in vitro* lung cancer model of A549 MCS, both MCS were treated with the same anticancer agents (cisplatin/paclitaxel) and miriplatin-loaded nano formulations for comparison. The two types of MCS (Figure 4.5) showed similar fifty percent inhibitory concentrations (IC₅₀) of cisplatin with no significant difference ($p > 0.05$). Figure 4.6 showed the cell viability of 3D MCS of the two cell lines against different miriplatin-loaded formulations. There was no significant difference between two cell lines in most treatment group ($p > 0.05$, except the TP/co-solvent group, $p = 0.0197$). Therefore,

3D MCS of A549-iRFP showed similar sensitivity to anticancer agents to 3D MCS of A549 and could serve as a valid lung cancer model to evaluate anticancer drugs and drug delivery systems.

The treatment procedure of this study was 3-day agent exposure plus 4-day agent-free growth. The medium with the free drugs/drug formulations was removed completely after 3-day exposure and replaced by fresh growth medium for the following 4-day growth. During the 7-day treatment, the iRFP fluorescent signal of A549-iRFP was recorded and analyzed to calculate the cell viability. Compared to the traditional 72-hour exposure treatment, the modified treatment procedure added 4 more days of drug-free growth to use the fluorescent signal to test whether the cancer cells would relapse after the drug exposure. This modification was designed to mimic the clinical regimens, where patients rest for weeks between each round of exposure to chemotherapy agents while the efficacy and toxicity of chemotherapy are continuously monitored.

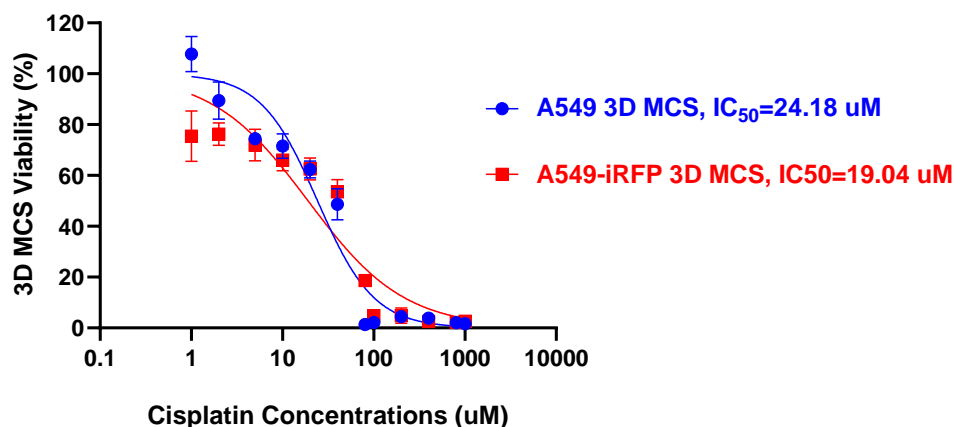


Figure 4.5. Cell viability of A549 (blue) and A549-iRFP (red) 3D MCS after 3-day exposure to cisplatin plus 4-day cisplatin-free growth (Mean \pm S.D, N = 4).

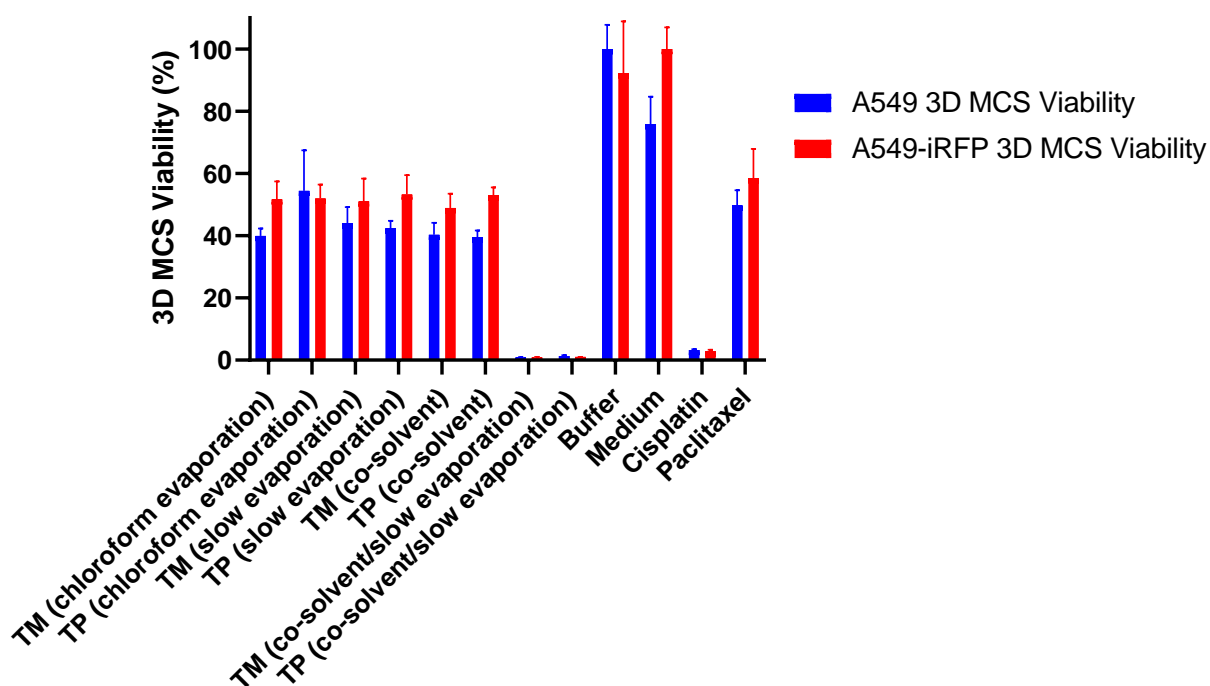


Figure 4.6. Cell viability of A549 (blue) and A549-iRFP (red) 3D MCS after 3-day exposure to miriplatin-loaded formulations plus 4-day drug-free growth (Mean \pm S.D, N = 4).

4.3.4 Comparison of Anticancer Activity of Miriplatin-Loaded Nano Formulations

Prepared by Different Methods

The cell viability of A549-iRFP 3D MCS by miriplatin-loaded nano formulations prepared by different methods was shown in Figure 4.7. The platinum recovery of each formulation was quantified by ICP-OES. In order to better correlate anticancer activity and platinum recovery, cell viability was transferred into growth inhibition by the equation mentioned in 4.2.4 and showed in Figure 4.8. There was a strong relationship between platinum recovery of different formulations and their anticancer activity that is assessed by both 3D viability assay and iRFP fluorescence. The higher the platinum recovery, the higher the anticancer activity would be. Although the platinum recovery could not be taken directly as the

encapsulation efficiency of nano formulations (as mentioned in Chapter 3), it could reflect the amount of miriplatin or its degradation products in the nano formulation preparation. The positive association between the anticancer activity against A549-iRFP 3D MCS and the platinum recovery supported this assumption. Thus, both platinum drug recovery and biological activity results strongly suggest that nano formulations prepared by the chloroform dripping/injection methods lost majority of the input miriplatin during the preparation. Co-solvent and slow evaporation both improved the platinum recovery. When both co-solvent and slow evaporation were implemented in the preparation, the resultant nano formulation showed significantly enhanced platinum recovery (>80%) and substantial anticancer activity against 3D MCS *in vitro*.

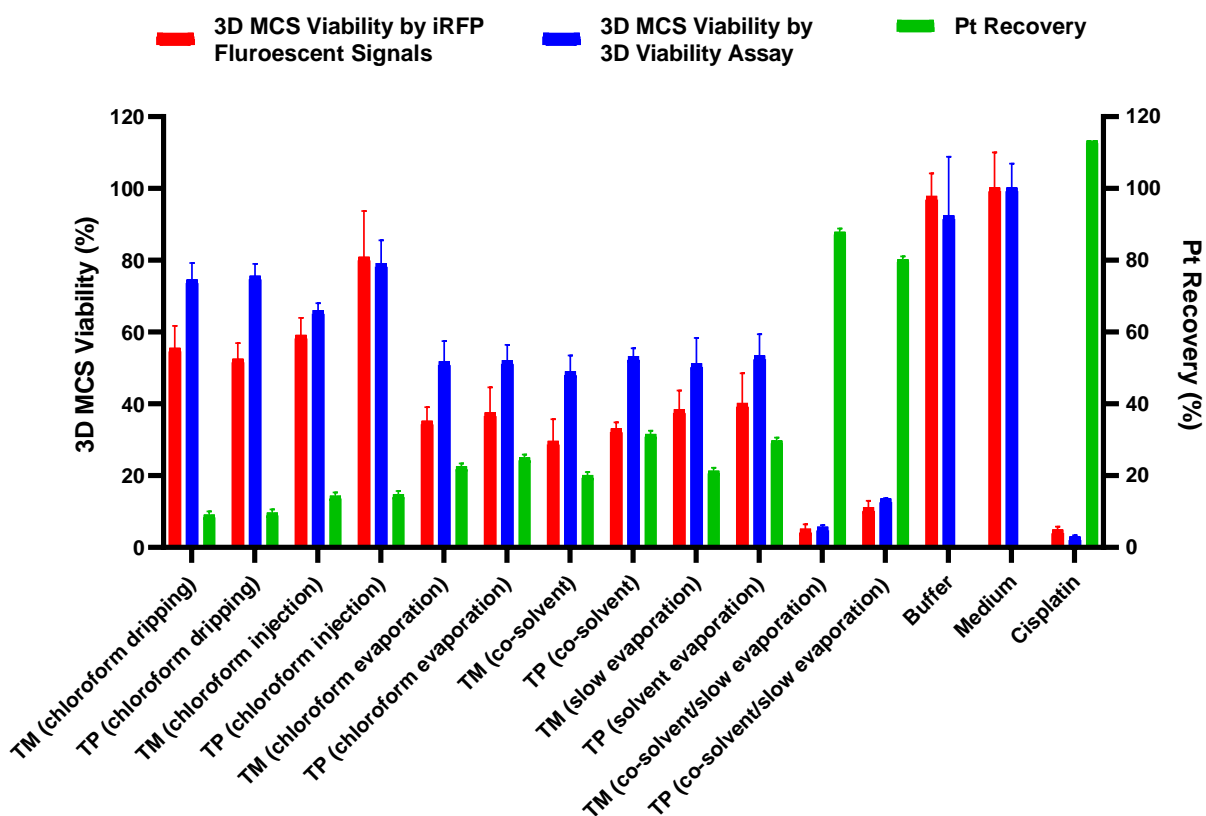


Figure 4.7. Cell viability of A549-iRFP 3D MCS after 3-day exposure to miriplatin-loaded nano formulation prepared by different methods at 400 μM input platinum concentration and 4-day platinum-free growth. The platinum recovery of each formulation (green) is also listed for reference (Mean \pm S.D, N = 4). The cell viability is quantified by the iRFP fluorescent signal (red) and by the 3D cell viability assay (blue). (TM: SLNs consisting of 90% TM/10% PE-PEG₂₀₀₀ + 20% miriplatin; TP: SLNs consisting of 90% TP/10% PE-PEG₂₀₀₀ + 20% miriplatin)

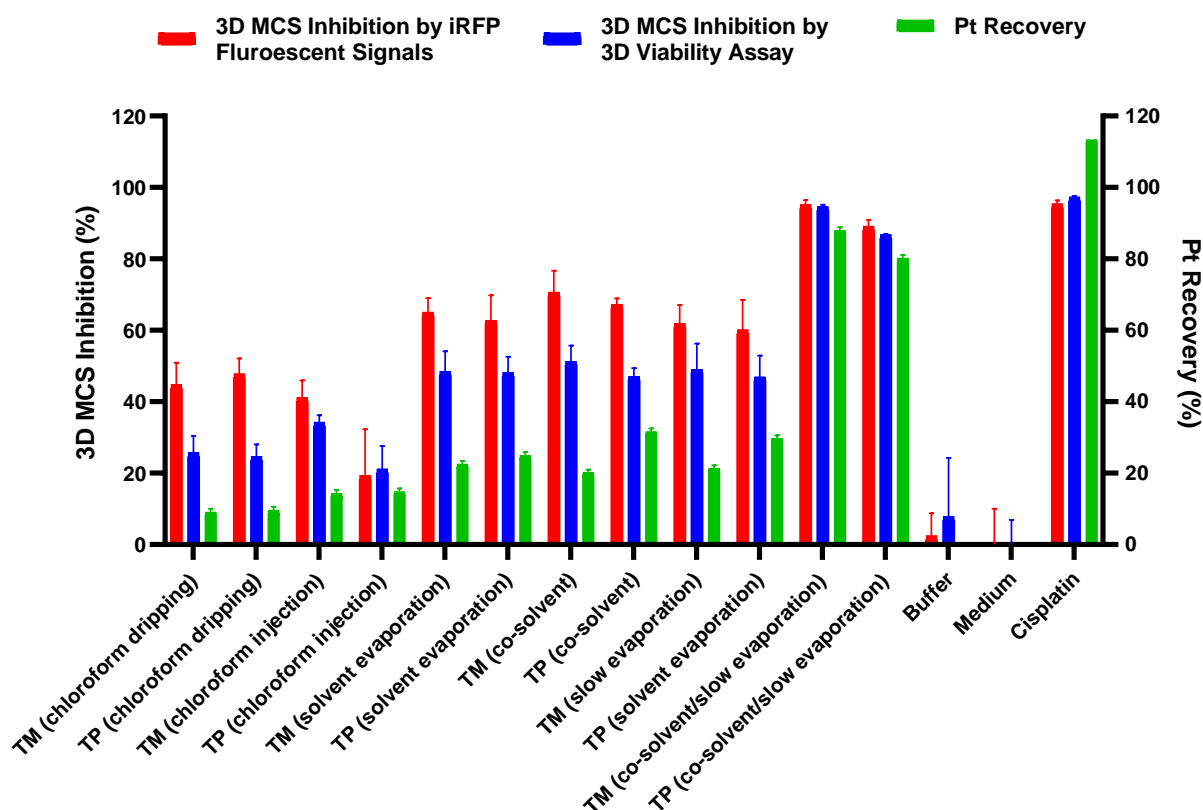


Figure 4.8. Growth inhibition of A549-iRFP 3D MCS after 3-day exposure to miriplatin-loaded nano formulation prepared by different methods at 400 μM input platinum concentration and 4-day platinum-free growth. The platinum recovery of each formulation (green) is also listed for reference (Mean \pm S.D, N = 4). The growth inhibition is defined as 100% minus cell viability quantified by the iRFP fluorescent signal (red) and by the 3D cell viability assay (blue). (TM: SLNs consisting of 90% TM/10% PE-PEG₂₀₀₀ + 20% miriplatin; TP: SLNs consisting of 90% TP/10% PE-PEG₂₀₀₀ + 20% miriplatin)

4.3.5 Anticancer Activity of Selected Miriplatin-Loaded Nano Formulations

The cell viability of A549-iRFP 3D MCS by miriplatin-loaded nano formulations prepared by co-solvent slow evaporation method at platinum input concentration of 400 μM is shown in Figure 4.9. All miriplatin-loaded nano formulations including micelles and SLNs showed substantial anticancer activity against A549-iRFP, which was comparable to cisplatin, a first-line anticancer drug against lung cancer. The low cell viability of these formulations

(<10%) was correlated to their high platinum recovery (>70%) as shown in Chapter 3. The 3D MCS treated by free miriplatin suspension showed no substantial anticancer activity. This is most probably caused by its extremely low solubility in aqueous phase. The lack of anticancer activity by miriplatin itself also indicates that miriplatin did not transform into any other platinum compound of substantial anticancer activity.

The miriplatin input concentration at 400 μM was much higher than the IC₅₀ value (19.04 μM) of cisplatin against A549-iRFP 3D MCS. The high concentration of miriplatin was initially used to screen different preparation methods to accommodate those that might have low encapsulation efficiency or low anticancer activity. Although all the miriplatin-loaded nano formulations prepared by co-solvent and slow evaporation showed extremely low cell viability below 10%, it should not be concluded that their anticancer activities are all as good as cisplatin because of their high input platinum concentration. In order to more thoroughly evaluate their efficacy against lung cancer model A549-iRFP 3D MCS, cell viability should be assayed at incremental concentration in comparison with cisplatin in the future. The slight difference of cell viability between different formulations should not be considered as sufficient evidence that which one was better than another for the same reason. The effect of combination therapy (miriplatin and paclitaxel) and cholesterol on anticancer activity also need to be studied by such dose response experiment.

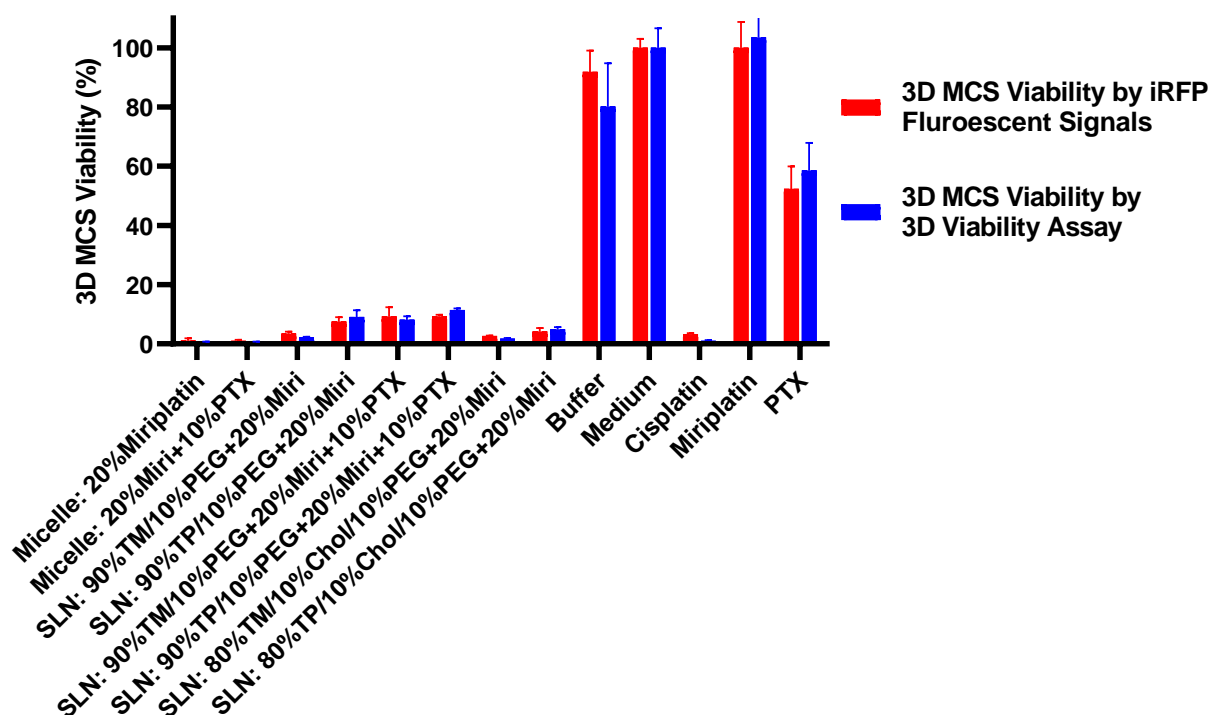


Figure 4.9. Cell viability of A549-iRFP 3D MCS after 3-day exposure to miriplatin-loaded nano formulations prepared by the co-solvent slow evaporation method and 4-day drug-free growth (Mean \pm S.D, N = 4). The cell viability was quantified by iRFP fluorescence (red) and by 3D cell viability assay (blue). (Miri: miriplatin, PTX: paclitaxel, Chol: cholesterol)

The daily dynamic change of iRFP fluorescent signal of A549-iRFP 3D MCS that have been exposed to miriplatin-loaded nano formulations prepared by co-solvent slow evaporation method is shown in Figure 4.10. The drastically higher fluorescent signal in the first three days could be explained by the excess suspended nano formulation, which might give arteficial signals by light scattering. After three-day exposure and change of growth medium, the fluorescent signals of all the nano formulation groups were comparable to the fluorescent signals of 3D MCS that had been treated with cisplatin. During the following four-day growth, both the fluorescent signals of formulation groups and the cisplatin group stayed low without noticeable

changes indicating that the three-day exposure was enough for extensive killing and that the cancer cells did not relapse 4 days after the clearance of the anticancer agents.

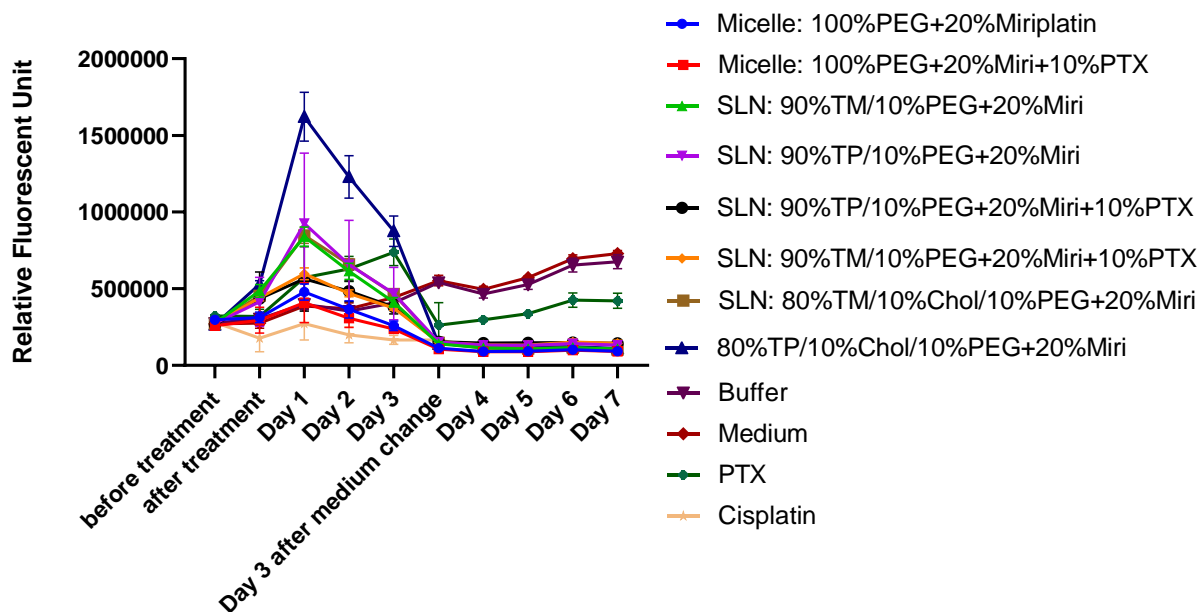


Figure 4.10. The dynamic change of iRFP fluorescent signal of A549-iRFP 3D MCS after 3-day exposure to miriplatin-loaded nano formulations prepared by co-solvent slow evaporation and 4-day drug-free growth (Mean \pm S.D, N = 4). (Miri: miriplatin, PTX: paclitaxel, Chol: cholesterol)

4.4 Summary

A 3D MCS model of A549-iRFP was successfully established for *in vitro* evaluation of activity against NSCLC. The viability of A549-iRFP 3D MCS after exposure to cisplatin or nano formulations was similar to A549 3D MCS. The anticancer activity of miriplatin-loaded formulations against 3D MCS was positively associated with the platinum recovery as quantified by ICP-OES. The miriplatin-loaded nano formulations that had been prepared by the co-solvent slow evaporation method showed substantial anticancer activity against A549 and A549-iRFP

3D MCS, which was comparable to cisplatin. Such encouraging results warrant further studies on miriplatin-loaded nano formulations in the future, such as dose-dependent viability of MCS growth.

CHAPTER 5: SUMMARY AND FUTURE WORK

Lung cancer claims the highest mortality and the second most new cases in the US. Approximately 40% of newly diagnosed lung cancer patients are in the advanced stage IV, for which platinum-based chemotherapy, individually or in combination with surgery or radiotherapy, is the first-line treatment. After the clinical use of the first platinum drug, cisplatin, many more platinum complexes have been investigated to overcome its drawbacks including severe side effects and induction of drug resistance.

Several characteristics of solid tumors in lung cancer constitute a physiochemical barrier to the deep penetration of chemotherapy agents. Nanocarriers provide a promising platform to overcome the physiochemical barrier and to reduce the systemic toxicity of anticancer chemotherapy. In this study, miriplatin, an exceptionally lipophilic platinum drug was formulated with various lipid-based nanocarriers including micelles and solid lipid nanoparticles (SLNs). The objective of this thesis project was to develop and evaluate miriplatin-loaded nano formulations against lung cancer.

Miriplatin-loaded formulations were successfully prepared by different methods, including one small, lab-scale method (thin film hydration) and several scale-up methods (chloroform dripping, chloroform injection, chloroform evaporation, co-solvent evaporation, chloroform slow evaporation and co-solvent slow evaporation). The size of the resultant nano formulations was characterized by dynamic light scattering (DLS) and presented using number-weighted distribution. Different compositions of the nano formulations have been investigated. Higher percentage of the pegylated lipid PE-PEG₂₀₀₀ in the composition resulted in smaller sizes.

Among the two types of nano formulations under this study, micelles were much smaller (~10 nm in diameter) and more homogeneous (PDI < 0.3), while SLNs were bigger (~ 100 nm in diameter) but had a more heterogeneous size distribution (PDI ~0.8).

HPLC and ICP-OES techniques were attempted to quantify miriplatin. Miriplatin was characterized by ESI-MS, which confirmed its chemical structure. Quantification using HPLC was attempted but then abandoned because of the low solubility and stability of miriplatin in common mobile phases (water, methanol, ethanol and acetonitrile). Instead, a quantification method for miriplatin was established using ICP-OES, which showed good consistency in different platinum-containing samples including platinum standard solutions, cisplatin and miriplatin. Platinum recovery in the quantification of different miriplatin-loaded nano formulations was promoted by digestion with 70% nitric acid and heating at 90 °C for 90 min. The solvent evaporation method to prepare miriplatin-loaded formulations improved the platinum recovery prominently from 10% to 75% by adding co-solvent and by slow evaporation. Thus, co-solvent slow evaporation has been established as a pharmaceutically viable scale-up method to prepare nano formulations of miriplatin.

Miriplatin-loaded nano formulations of different compositions were negatively stained with uranyl acetate and then imaged by TEM. The size and morphology of the miriplatin-loaded nano formulations observed from TEM images were consistent with the size and PDI data from DLS studies by the Malvern Zetasizer. In the TEM studies, micelles showed a morphology of spherical dots at around 10 nm in diameter while SLNs showed both spherical and rod structures with a size distribution from 50 to 150 nm.

A 3D MCS model of A549-iRFP was successfully established for in vitro evaluation of anticancer activity against lung cancer. A549-iRFP cells were engineered from the common lung cancer cell line A549 to stably express the near infrared fluorescent protein (iRFP). A strong linear relationship was found between iRFP fluorescent signal and cell viability. The cell viability of A549-iRFP 3D MCS after exposure to cisplatin or nano formulations was similar to A549 3D MCS. The anticancer activity of miriplatin-loaded formulations against 3D MCS was positively associated with the platinum recovery by ICP-OES. The miriplatin-loaded nano formulations that had been prepared by the co-solvent slow evaporation method showed substantial anticancer activity against both A549 and A549-iRFP 3D MCS, which was comparable to cisplatin. The growth of A549-iRFP 3D MCS after various treatment was monitored by the iRFP fluorescent signal. Three-day exposure to miriplatin-loaded nano formulations was enough for extensive killing and the cancer cells did not relapse during the following 4 days of further culturing in drug-free media.

Future work for further development of miriplatin-loaded nano formulations would include optimization of the lipid compositions. For examples, phospholipids and triglycerides with different lengths of hydrocarbon chains can be tested as potential lipid components to balance between stability and drug release; stabilizers such as cholesterol myristate can be added into the lipid composition to improve the stability and homogeneity of nano formulations; the surface of the nanocarriers can be modified with active targeting ligands to increase the drug accumulation at the lung tumor site.

For future applications in industry, the scale-up method (co-solvent slow evaporation method) also needs improvement to reduce batch-to-batch variance. The temperature increase and the stirring speed can be better controlled by instrumental programming rather than manual

operation. If needed, the key factors (such as solvent ratio, stirring speed and heating duration) can be further investigated by design of experiments (DoE) to find their effects on the nano formulations' physiochemical properties. Moreover, storage procedures such as lyophilization and spray-drying also need to be considered in order to reduce the degradation of the miriplatin formulations in aqueous media.

In order to quantify the encapsulation efficiency of miriplatin-loaded nano formulations for better dosage control in further *in vitro* and *in vivo* studies, different forms of platinum need to be quantified. Possible techniques include chloroform extraction and ^{195}Pt -NMR. In addition, selected miriplatin-loaded formulations showed substantial anticancer activity against A549-iRFP 3D MCS but at a high platinum dosage (400 μM). The dose-dependent inhibition of 3D MCS growth by the miriplatin formulations need to be studied before further animal studies.

In conclusion, co-solvent slow evaporation has been established as a pharmaceutically viable scale-up method to prepare miriplatin-loaded formulations that carry smaller size, low PDI and high platinum recovery. A quantification method for miriplatin using ICP has been established. Selected miriplatin-loaded formulations prepared by co-solvent slow evaporation method showed substantial anticancer activities against A549 and A549-iRFP 3D MCS, which were comparable to cisplatin, a first-line anticancer drug against lung cancer.

REFERENCES

1. American Cancer Society. Cancer Facts & Figures 2020. Atlanta: American Cancer Society;. 2020.
2. World Health Organization, Cancer Fact Sheets. 2018; Available from: <https://www.who.int/news-room/fact-sheets/detail/cancer>. 2018.
3. Siegel, R.L., K.D. Miller, and A. Jemal, Cancer statistics. CA Cancer J Clin, 2020. **70**(1): p. 7-30.
4. American cancer society. Lung Cancer Causes. Available from: <https://www.cancer.org/cancer/lung-cancer/causes-risks-prevention/what-causes.html>. 2019.
5. Travis, W.D., E. Brambilla, and G.J. Riely, New pathologic classification of lung cancer: relevance for clinical practice and clinical trials. J Clin Oncol, 2013. **31**(8): p. 992-1001.
6. Travis, W.D., et al., The 2015 World Health Organization Classification of Lung Tumors: Impact of Genetic, Clinical and Radiologic Advances Since the 2004 Classification. J Thorac Oncol, 2015. **10**(9): p. 1243-1260.
7. Lemjabbar-Alaoui, H., et al., Lung cancer: Biology and treatment options. Biochim Biophys Acta, 2015. **1856**(2): p. 189-210.
8. Gridelli, C., et al., Non-small-cell lung cancer. Nat Rev Dis Primers, 2015. **1**: p. 15009.
9. Howington, J.A., et al., Treatment of stage I and II non-small cell lung cancer: Diagnosis and management of lung cancer, 3rd ed: American College of Chest Physicians evidence-based clinical practice guidelines. Chest, 2013. **143**(5 Suppl): p. e278S-e313S.

10. Zappa, C. and S.A. Mousa, Non-small cell lung cancer: current treatment and future advances. *Transl Lung Cancer Res*, 2016. **5**(3): p. 288-300.
11. Chemotherapy in non-small cell lung cancer: a meta-analysis using updated data on individual patients from 52 randomised clinical trials. *BMJ*, 1995. **311**(7010): p. 899-909.
12. Mayo Clinic. Lung-cancer/diagnosis-treatment. Available from: <https://www.mayoclinic.org/diseases-conditions/lung-cancer/diagnosis-treatment/drc-20374627>. 2020.
13. Scott, W.J., et al., Treatment of non-small cell lung cancer stage I and stage II: ACCP evidence-based clinical practice guidelines (2nd edition). *Chest*, 2007. **132**(3 Suppl): p. 234S-242S.
14. Schreiber, R.D., L.J. Old, and M.J. Smyth, Cancer immunoediting: integrating immunity's roles in cancer suppression and promotion. *Science*, 2011. **331**(6024): p. 1565-70.
15. Banchereau, J. and R.M. Steinman, Dendritic cells and the control of immunity. *Nature*, 1998. **392**(6673): p. 245-52.
16. van Meerbeeck, J.P., D.A. Fennell, and D.K.M. De Ruyscher, Small-cell lung cancer. *The Lancet*, 2011. **378**(9804): p. 1741-1755.
17. Rossi, A. and M. Di Maio, Platinum-based chemotherapy in advanced non-small-cell lung cancer: optimal number of treatment cycles. *Expert Rev Anticancer Ther*, 2016. **16**(6): p. 653-60.
18. Masters, G.A., et al., Systemic Therapy for Stage IV Non-Small-Cell Lung Cancer: American Society of Clinical Oncology Clinical Practice Guideline Update. *J Clin Oncol*, 2015. **33**(30): p. 3488-515.

19. Browning, R.J., et al., Drug Delivery Strategies for Platinum-Based Chemotherapy. *ACS Nano*, 2017. **11**(9): p. 8560-8578.
20. Rosenberg, B., et al., Platinum compounds: a new class of potent antitumour agents. *Nature*, 1969. **222**(5191): p. 385-6.
21. Johnstone, T.C., K. Suntharalingam, and S.J. Lippard, The Next Generation of Platinum Drugs: Targeted Pt(II) Agents, Nanoparticle Delivery, and Pt(IV) Prodrugs. *Chem Rev*, 2016. **116**(5): p. 3436-86.
22. Feng, Chao. (2019). Approaches to the Search of Platinum Anticancer Agents: Derivatizing Current Drugs and Incorporating HDAC Inhibition. University of the Pacific, Dissertation. Available from:
https://scholarlycommons.pacific.edu/uop_etds/3637.
23. Alderden, R.A., M.D. Hall, and T.W. Hambley, The Discovery and Development of Cisplatin. *Journal of Chemical Education*, 2006. **83**(5).
24. Holzer, A.K., G.H. Manorek, and S.B. Howell, Contribution of the major copper influx transporter CTR1 to the cellular accumulation of cisplatin, carboplatin, and oxaliplatin. *Mol Pharmacol*, 2006. **70**(4): p. 1390-4.
25. Jung, Y. and S.J. Lippard, Direct cellular responses to platinum-induced DNA damage. *Chem Rev*, 2007. **107**(5): p. 1387-407.
26. Eastman, A., The formation, isolation and characterization of DNA adducts produced by anticancer platinum complexes. *Pharmacol Ther*, 1987. **34**(2): p. 155-66.
27. Kartalou, M. and J.M. Essigmann, Recognition of cisplatin adducts by cellular proteins. *Mutat Res*, 2001. **478**(1-2): p. 1-21.

28. Basu, A. and S. Krishnamurthy, Cellular responses to Cisplatin-induced DNA damage. *J Nucleic Acids*, 2010. **2010**.
29. Ghosh, S., Cisplatin: The first metal based anticancer drug. *Bioorg Chem*, 2019. **88**: p. 102925.
30. Miller, R.P., et al., Mechanisms of Cisplatin nephrotoxicity. *Toxins (Basel)*, 2010. **2**(11): p. 2490-518.
31. Burger, H., et al., Drug transporters of platinum-based anticancer agents and their clinical significance. *Drug Resist Updat*, 2011. **14**(1): p. 22-34.
32. Pasello, M., et al., Overcoming glutathione S-transferase P1-related cisplatin resistance in osteosarcoma. *Cancer Res*, 2008. **68**(16): p. 6661-8.
33. Kelland, L.R., Preclinical Perspectives on Platinum Resistance. *Drugs*, 2000. **59**(4): p. 1-8.
34. Wilson, J.J. and S.J. Lippard, Synthetic methods for the preparation of platinum anticancer complexes. *Chem Rev*, 2014. **114**(8): p. 4470-95.
35. Silverman, A.P., et al., 2.4-A crystal structure of the asymmetric platinum complex [Pt(amine)(cyclohexylamine)]²⁺ bound to a dodecamer DNA duplex. *J Biol Chem*, 2002. **277**(51): p. 49743-9.
36. Lovejoy, K.S., et al., cis-Diammine(pyridine)chloroplatinum(II), a monofunctional platinum(II) antitumor agent: Uptake, structure, function, and prospects. *Proc Natl Acad Sci U S A*, 2008. **105**(26): p. 8902-7.
37. Wheate, N.J., et al., The status of platinum anticancer drugs in the clinic and in clinical trials. *Dalton Trans*, 2010. **39**(35): p. 8113-27.

38. Deo, K.M., et al., Platinum coordination compounds with potent anticancer activity. *Coordination Chemistry Reviews*, 2018. **375**: p. 148-163.
39. Rixe, O., et al., Oxaliplatin, tetraplatin, cisplatin, and carboplatin: spectrum of activity in drug-resistant cell lines and in the cell lines of the National Cancer Institute's Anticancer Drug Screen panel. *Biochem Pharmacol*, 1996. **52**(12): p. 1855-65.
40. Knox, R.J., et al., Mechanism of cytotoxicity of anticancer platinum drugs: evidence that cis-diamminedichloroplatinum(II) and cis-diammine-(1,1-cyclobutanedicarboxylato)platinum(II) differ only in the kinetics of their interaction with DNA. *Cancer Res*, 1986. **46**(4 Pt 2): p. 1972-9.
41. Zdraveski, Z.Z., et al., MutS preferentially recognizes cisplatin- over oxaliplatin-modified DNA. *J Biol Chem*, 2002. **277**(2): p. 1255-60.
42. Raymond, E., et al., Cellular and molecular pharmacology of oxaliplatin. *Mol Cancer Ther*, 2002. **1**(3): p. 227-35.
43. Zhang, S., et al., Organic cation transporters are determinants of oxaliplatin cytotoxicity. *Cancer Res*, 2006. **66**(17): p. 8847-57.
44. KUNIMATSU, T., J. SHIMAKURA, and M. HANADA, Development of Miriplatin, a Novel Antitumor Platinum for Hepatocellular Carcinoma. 2011.
45. Tredan, O., et al., Drug resistance and the solid tumor microenvironment. *J Natl Cancer Inst*, 2007. **99**(19): p. 1441-54.
46. Mittal, V., et al., The Microenvironment of Lung Cancer and Therapeutic Implications. *Adv Exp Med Biol*, 2016. **890**: p. 75-110.
47. Lu, Y., Fliposomes with a pH-sensitive conformational switch for anticancer drug delivery against triple negative breast cancer (Order No. 13814112). Available from

- Dissertations & Theses @ University of the Pacific. (2217758143). Retrieved from <https://0-search.proquest.com/pacificatclassic.pacific.edu/docview/2217758143?accountid=14704>. 2019.
48. Kobayashi, H., R. Watanabe, and P.L. Choyke, Improving conventional enhanced permeability and retention (EPR) effects; what is the appropriate target? *Theranostics*, 2013. **4**(1): p. 81-9.
 49. Aznavoorian, S., et al., Signal transduction for chemotaxis and haptotaxis by matrix molecules in tumor cells. *The Journal of cell biology*, 1990. **110**(4): p. 1427-1438.
 50. Ohtani, H., Stromal reaction in cancer tissue: pathophysiologic significance of the expression of matrix-degrading enzymes in relation to matrix turnover and immune/inflammatory reactions. *Pathology international*, 1998. **48**(1): p. 1-9.
 51. Bissell, M.J. and D. Radisky, Putting tumours in context. *Nature Reviews Cancer*, 2001. **1**(1): p. 46-54.
 52. Kinzler, K.W. and B. Vogelstein, Landscaping the cancer terrain. *Science*, 1998. **280**(5366): p. 1036-1037.
 53. Konerding, M.A., A.J. Miodonski, and A. Lametschwandtner, Microvascular corrosion casting in the study of tumor vascularity: a review. *Scanning Microsc*, 1995. **9**(4): p. 1233-43; discussion 1243-4.
 54. Jain, R.K., Determinants of tumor blood flow: a review. *Cancer Res*, 1988. **48**(10): p. 2641-58.
 55. Stohrer, M., et al., Oncotic pressure in solid tumors is elevated. *Cancer Res*, 2000. **60**(15): p. 4251-5.

56. Ji, R.C., Characteristics of lymphatic endothelial cells in physiological and pathological conditions. *Histol Histopathol*, 2005. **20**(1): p. 155-75.
57. Din, F.U., et al., Effective use of nanocarriers as drug delivery systems for the treatment of selected tumors. *Int J Nanomedicine*, 2017. **12**: p. 7291-7309.
58. Maeda, H., Toward a full understanding of the EPR effect in primary and metastatic tumors as well as issues related to its heterogeneity. *Adv Drug Deliv Rev*, 2015. **91**: p. 3-6.
59. Maeda, H., Tumor-selective delivery of macromolecular drugs via the EPR effect: background and future prospects. *Bioconjug Chem*, 2010. **21**(5): p. 797-802.
60. Zhang, B., Y. Hu, and Z. Pang, Modulating the Tumor Microenvironment to Enhance Tumor Nanomedicine Delivery. *Front Pharmacol*, 2017. **8**: p. 952.
61. Perry, J.L., et al., Mediating Passive Tumor Accumulation through Particle Size, Tumor Type, and Location. *Nano Lett*, 2017. **17**(5): p. 2879-2886.
62. van Vlerken, L.E., T.K. Vyas, and M.M. Amiji, Poly(ethylene glycol)-modified nanocarriers for tumor-targeted and intracellular delivery. *Pharm Res*, 2007. **24**(8): p. 1405-14.
63. Kobayashi, H. and M.W. Brechbiel, Nano-sized MRI contrast agents with dendrimer cores. *Adv Drug Deliv Rev*, 2005. **57**(15): p. 2271-86.
64. Attia, M.F., et al., An overview of active and passive targeting strategies to improve the nanocarriers efficiency to tumour sites. *J Pharm Pharmacol*, 2019. **71**(8): p. 1185-1198.
65. Nakamura, Y., et al., Nanodrug Delivery: Is the Enhanced Permeability and Retention Effect Sufficient for Curing Cancer? *Bioconjug Chem*, 2016. **27**(10): p. 2225-2238.

66. Patra, C.R., et al., Targeted delivery of gemcitabine to pancreatic adenocarcinoma using cetuximab as a targeting agent. *Cancer Res*, 2008. **68**(6): p. 1970-8.
67. Leserman, L.D., et al., Targeting to cells of fluorescent liposomes covalently coupled with monoclonal antibody or protein A. *Nature*, 1980. **288**(5791): p. 602-4.
68. Yoo, J., et al., Active Targeting Strategies Using Biological Ligands for Nanoparticle Drug Delivery Systems. *Cancers (Basel)*, 2019. **11**(5).
69. Gorain, B., et al., Overexpressed Receptors and Proteins in Lung Cancer, in *Nanotechnology-Based Targeted Drug Delivery Systems for Lung Cancer*. 2019. p. 39-75.
70. Roma-Rodrigues, C., et al., Targeting Tumor Microenvironment for Cancer Therapy. *Int J Mol Sci*, 2019. **20**(4).
71. Bello, L., et al., Alpha(v)beta3 and alpha(v)beta5 integrin expression in glioma periphery. *Neurosurgery*, 2001. **49**(2): p. 380-9; discussion 390.
72. Müller, R.H., et al., Phagocytic uptake and cytotoxicity of solid lipid nanoparticles (SLN) sterically stabilized with poloxamine 908 and poloxamer 407. *J Drug Target*, 1996. **4**(3): p. 161-70.
73. Mishra, B., B.B. Patel, and S. Tiwari, Colloidal nanocarriers: a review on formulation technology, types and applications toward targeted drug delivery. *Nanomedicine*, 2010. **6**(1): p. 9-24.
74. P, B.K.a.C., Lipid nano particulate drug delivery: An overview of the emerging trend. *The Pharma Innovation Journal*. 2018; 7(7): 779-789., 2018.
75. Xiao, K., et al., The effect of surface charge on in vivo biodistribution of PEG-oligocholic acid based micellar nanoparticles. *Biomaterials*, 2011. **32**(13): p. 3435-46.

76. Wang, W., et al., The impact of nanoparticle shape on cellular internalisation and transport: what do the different analysis methods tell us? *Materials Horizons*, 2019. **6**(8): p. 1538-1547.
77. Li, Y., M. Kroger, and W.K. Liu, Shape effect in cellular uptake of PEGylated nanoparticles: comparison between sphere, rod, cube and disk. *Nanoscale*, 2015. **7**(40): p. 16631-46.
78. Gupta, R., et al., Permeation of nanoparticles across the intestinal lipid membrane: dependence on shape and surface chemistry studied through molecular simulations. *Nanoscale*, 2020. **12**(11): p. 6318-6333.
79. Sun, T., et al., Engineered nanoparticles for drug delivery in cancer therapy. *Angew Chem Int Ed Engl*, 2014. **53**(46): p. 12320-64.
80. Dattani, P., Development and characterization of LDV peptide targeted nanocarriers for paclitaxel delivery: A comparative study of micelles, liposomes and solid lipid nanoparticles (Order No. 13885051). Available from Dissertations & Theses @ University of the Pacific; ProQuest Dissertations & Theses Global. (2242545235). Retrieved from <https://0-search.proquest.com.pacificatclassic.pacific.edu/docview/2242545235?accountid=14704>. 2019.
81. Zhao, B.J., et al., The antiangiogenic efficacy of NGR-modified PEG-DSPE micelles containing paclitaxel (NGR-M-PTX) for the treatment of glioma in rats. *J Drug Target*, 2011. **19**(5): p. 382-90.

82. Musacchio, T., et al., PEG-PE micelles loaded with paclitaxel and surface-modified by a PBR-ligand: synergistic anticancer effect. *Molecular pharmaceutics*, 2009. **6**(2): p. 468-479.
83. Allen, T.M. and P.R. Cullis, Liposomal drug delivery systems: from concept to clinical applications. *Adv Drug Deliv Rev*, 2013. **65**(1): p. 36-48.
84. Eloy, J.O., et al., Liposomes as carriers of hydrophilic small molecule drugs: strategies to enhance encapsulation and delivery. *Colloids Surf B Biointerfaces*, 2014. **123**: p. 345-63.
85. Koudelka, S. and J. Turanek, Liposomal paclitaxel formulations. *J Control Release*, 2012. **163**(3): p. 322-34.
86. Allen, T.M., Stealth Liposomes: Five Years On. *Journal of Liposome Research*, 2008. **2**(3): p. 289-305.
87. Johnston, M.J., et al., Therapeutically optimized rates of drug release can be achieved by varying the drug-to-lipid ratio in liposomal vincristine formulations. *Biochim Biophys Acta*, 2006. **1758**(1): p. 55-64.
88. Ghasemiyeh, P. and S. Mohammadi-Samani, Solid lipid nanoparticles and nanostructured lipid carriers as novel drug delivery systems: applications, advantages and disadvantages. *Res Pharm Sci*, 2018. **13**(4): p. 288-303.
89. Das, S. and A. Chaudhury, Recent advances in lipid nanoparticle formulations with solid matrix for oral drug delivery. *AAPS PharmSciTech*, 2011. **12**(1): p. 62-76.
90. Bangham, A.D., M.M. Standish, and G. Weissmann, The action of steroids and streptolysin S on the permeability of phospholipid structures to cations. *Journal of Molecular Biology*, 1965. **13**(1): p. 253-IN28.

91. Stylianopoulos, T., EPR-effect: utilizing size-dependent nanoparticle delivery to solid tumors. *Therapeutic Delivery*, 2013. **4**(4): p. 421-423.
92. Ganesan, P. and D. Narayanasamy, Lipid nanoparticles: Different preparation techniques, characterization, hurdles, and strategies for the production of solid lipid nanoparticles and nanostructured lipid carriers for oral drug delivery. *Sustainable Chemistry and Pharmacy*, 2017. **6**: p. 37-56.
93. Amoabediny, G., et al., Overview of preparation methods of polymeric and lipid-based (niosome, solid lipid, liposome) nanoparticles: A comprehensive review. *International Journal of Polymeric Materials and Polymeric Biomaterials*, 2017. **67**(6): p. 383-400.
94. Schubert, M., Solvent injection as a new approach for manufacturing lipid nanoparticles – evaluation of the method and process parameters. *European Journal of Pharmaceutics and Biopharmaceutics*, 2003. **55**(1): p. 125-131.
95. Puri, A., et al., Lipid-based nanoparticles as pharmaceutical drug carriers: from concepts to clinic. *Critical reviews in therapeutic drug carrier systems*, 2009. **26**(6): p. 523-580.
96. Hanada, M., et al., Intra-hepatic arterial administration with miriplatin suspended in an oily lymphographic agent inhibits the growth of tumors implanted in rat livers by inducing platinum-DNA adducts to form and massive apoptosis. *Cancer Chemother Pharmacol*, 2009. **64**(3): p. 473-83.
97. Bayat Mokhtari, R., et al., Combination therapy in combating cancer. *Oncotarget*, 2017. **8**(23): p. 38022-38043.
98. Sarisozen, C., et al., PEG-PE-based micelles co-loaded with paclitaxel and cyclosporine A or loaded with paclitaxel and targeted by anticancer antibody overcome drug resistance in cancer cells. *Drug Deliv*, 2012. **19**(4): p. 169-76.

99. Leiva, M.C., et al., Tripalmitin nanoparticle formulations significantly enhance paclitaxel antitumor activity against breast and lung cancer cells in vitro. *Sci Rep*, 2017. **7**(1): p. 13506.
100. Kathe, N., B. Henriksen, and H. Chauhan, Physicochemical characterization techniques for solid lipid nanoparticles: principles and limitations. *Drug Dev Ind Pharm*, 2014. **40**(12): p. 1565-75.
101. Raval, N., et al., Importance of Physicochemical Characterization of Nanoparticles in Pharmaceutical Product Development, in *Basic Fundamentals of Drug Delivery*. 2019. p. 369-400.
102. Bertrand, N. and J.C. Leroux, The journey of a drug-carrier in the body: an anatomophysiological perspective. *J Control Release*, 2012. **161**(2): p. 152-63.
103. Caracciolo, G., Clinically approved liposomal nanomedicines: lessons learned from the biomolecular corona. *Nanoscale*, 2018. **10**(9): p. 4167-4172.
104. Gradishar, W.J., et al., Phase III trial of nanoparticle albumin-bound paclitaxel compared with polyethylated castor oil-based paclitaxel in women with breast cancer. *J Clin Oncol*, 2005. **23**(31): p. 7794-803.
105. O'Brien, M.E., et al., Reduced cardiotoxicity and comparable efficacy in a phase III trial of pegylated liposomal doxorubicin HCl (CAELYX/Doxil) versus conventional doxorubicin for first-line treatment of metastatic breast cancer. *Ann Oncol*, 2004. **15**(3): p. 440-9.
106. Ssolvent Miscibility Chart. Available from: <https://www.templateroller.com/template/214400/solvent-miscibility-chart.html>. 2020.

107. Redondo-Morata, L., M.I. Giannotti, and F. Sanz, Influence of cholesterol on the phase transition of lipid bilayers: a temperature-controlled force spectroscopy study. *Langmuir*, 2012. **28**(35): p. 12851-60.
108. Lu, T., et al., Influence of polymer size, liposomal composition, surface charge, and temperature on the permeability of pH-sensitive liposomes containing lipid-anchored poly(2-ethylacrylic acid). *Int J Nanomedicine*, 2012. **7**: p. 4917-26.
109. Liu, S., et al., Preparation, Characterization, and Antitumor Activities of Miriplatin-Loaded Liposomes. *J Pharm Sci*, 2016. **105**(1): p. 78-87.
110. Wilschefski, S.C. and M.R. Baxter, Inductively Coupled Plasma Mass Spectrometry: Introduction to Analytical Aspects. *The Clinical biochemist. Reviews*, 2019. **40**(3): p. 115-133.
111. The development of analytical procedures using ICP-OES and ICP-MS for the analysis of trace metals in pharmaceutical formulations. *British Journal of Pharmacy*, 2017. **2**(2).
112. Khan, K.F., Application, principle and operation of ICP-OES in pharmaceutical analysis. 2019.
113. Caruso, F., et al., ICP-OES method for the characterization of cement pore solutions and their modification by polycarboxylate-based superplasticizers. *Cement and Concrete Research*, 2017. **91**: p. 52-60.
114. Asadi Asadabad, M. and M. Jafari Eskandari, Transmission Electron Microscopy as Best Technique for Characterization in Nanotechnology. *Synthesis and Reactivity in Inorganic, Metal-Organic, and Nano-Metal Chemistry*, 2014. **45**(3): p. 323-326.

115. Reimer, L., Transmission electron microscopy : physics of image formation and microanalysis / Ludwig Reimer. Springer series in optical sciences ; v. 36. 1984, Berlin ; New York: Springer-Verlag.
116. Barreto-Vieira, D.F. and O.M. Barth, Negative and Positive Staining in Transmission Electron Microscopy for Virus Diagnosis, in Microbiology in Agriculture and Human Health. 2015.
117. Ma, Y. and X. Wei, Determination of platinum in waste platinum-loaded carbon catalyst samples using microwave-assisted sample digestion and ICP-OES. 2017.
118. Niemelä, M., et al., Microwave-assisted aqua regia digestion for determining platinum, palladium, rhodium and lead in catalyst materials. *Microchemical Journal*, 2012. **101**: p. 75-79.
119. Varbanov, H.P., et al., Oxaliplatin reacts with DMSO only in the presence of water. *Dalton Trans*, 2017. **46**(28): p. 8929-8932.
120. Priquelier, J.R.L., I.S. Butler, and F.D. Rochon, An Overview of ¹⁹⁵Pt Nuclear Magnetic Resonance Spectroscopy. *Applied Spectroscopy Reviews*, 2006. **41**(3): p. 185-226.
121. Wang, Y., et al., Pegylated phospholipids-based self-assembly with water-soluble drugs. *Pharm Res*, 2010. **27**(2): p. 361-70.
122. Lu, X., et al., Polymeric micelles as a drug delivery system enhance cytotoxicity of vinorelbine through more intercellular accumulation. *Drug Deliv*, 2010. **17**(4): p. 255-62.
123. Zhao, Y., et al., A comparison between sphere and rod nanoparticles regarding their in vivo biological behavior and pharmacokinetics. *Sci Rep*, 2017. **7**(1): p. 4131.
124. Hinde, E., et al., Pair correlation microscopy reveals the role of nanoparticle shape in intracellular transport and site of drug release. *Nat Nanotechnol*, 2017. **12**(1): p. 81-89.

125. Kolhar, P., et al., Using shape effects to target antibody-coated nanoparticles to lung and brain endothelium. *Proc Natl Acad Sci U S A*, 2013. **110**(26): p. 10753-8.
126. Kónya, Z., et al., Novel Two-Step Synthesis of Controlled Size and Shape Platinum Nanoparticles Encapsulated in Mesoporous Silica. *Catalysis Letters*, 2002. **81**(3/4): p. 137-140.
127. Toro-Cordova, A., et al., Liposomes Loaded with Cisplatin and Magnetic Nanoparticles: Physicochemical Characterization, Pharmacokinetics, and In-Vitro Efficacy. *Molecules*, 2018. **23**(9).
128. Lazzari, G., P. Couvreur, and S. Mura, Multicellular tumor spheroids: a relevant 3D model for the in vitro preclinical investigation of polymer nanomedicines. *Polymer Chemistry*, 2017. **8**(34): p. 4947-4969.
129. Huang, B.W. and J.Q. Gao, Application of 3D cultured multicellular spheroid tumor models in tumor-targeted drug delivery system research. *J Control Release*, 2018. **270**: p. 246-259.
130. Sant, S. and P.A. Johnston, The production of 3D tumor spheroids for cancer drug discovery. *Drug Discov Today Technol*, 2017. **23**: p. 27-36.
131. Imamura, Y., et al., Comparison of 2D- and 3D-culture models as drug-testing platforms in breast cancer. *Oncol Rep*, 2015. **33**(4): p. 1837-43.
132. Langhans, S.A., Three-Dimensional in Vitro Cell Culture Models in Drug Discovery and Drug Repositioning. *Front Pharmacol*, 2018. **9**: p. 6.
133. Chaicharoenaudomrung, N., P. Kunhorm, and P. Noisa, Three-dimensional cell culture systems as an in vitro platform for cancer and stem cell modeling. *World J Stem Cells*, 2019. **11**(12): p. 1065-1083.

134. Friedrich, J., R. Ebner, and L.A. Kunz-Schughart, Experimental anti-tumor therapy in 3-D: spheroids--old hat or new challenge? *Int J Radiat Biol*, 2007. **83**(11-12): p. 849-71.
135. Inch, W.R., J.A. McCredie, and R.M. Sutherland, Growth of nodular carcinomas in rodents compared with multi-cell spheroids in tissue culture. *Growth*, 1970. **34**(3): p. 271-82.
136. Wang, C., et al., Three-dimensional in vitro cancer models: a short review. *Biofabrication*, 2014. **6**(2): p. 022001.
137. Hirschhaeuser, F., et al., Multicellular tumor spheroids: an underestimated tool is catching up again. *J Biotechnol*, 2010. **148**(1): p. 3-15.
138. Kim, J.B., Three-dimensional tissue culture models in cancer biology. *Semin Cancer Biol*, 2005. **15**(5): p. 365-77.
139. Florczyk, S.J., et al., 3D Porous Chitosan-Alginate Scaffolds Promote Proliferation and Enrichment of Cancer Stem-Like Cells. *J Mater Chem B*, 2016. **4**(38): p. 6326-6334.
140. Oliveira, M.S., et al., Solid lipid nanoparticles co-loaded with doxorubicin and alpha-tocopherol succinate are effective against drug-resistant cancer cells in monolayer and 3-D spheroid cancer cell models. *Int J Pharm*, 2016. **512**(1): p. 292-300.
141. Perche, F., N.R. Patel, and V.P. Torchilin, Accumulation and toxicity of antibody-targeted doxorubicin-loaded PEG-PE micelles in ovarian cancer cell spheroid model. *J Control Release*, 2012. **164**(1): p. 95-102.
142. Ho, D.N., et al., Penetration of endothelial cell coated multicellular tumor spheroids by iron oxide nanoparticles. *Theranostics*, 2012. **2**(1): p. 66-75.

143. Huang, Y., et al., Intrapulmonary inoculation of multicellular spheroids to construct an orthotopic lung cancer xenograft model that mimics four clinical stages of non-small cell lung cancer. *J Pharmacol Toxicol Methods*, 2020: p. 106885.
144. Khot, M., et al., A Review on the Recent Advancement in Tumour Spheroids-on-a-Chip. *Journal of Cancer Research and Practice*, 2019. **6**(2): p. 55-63.